2-9-2011

Multispectral plasmon enhanced quantum dots in a well infrared photodetectors

Rajeev V. Shenoi

Recommended Citation

Shenoi, Rajeev V.. "Multispectral plasmon enhanced quantum dots in a well infrared photodetectors." (2011). https://digitalrepository.unm.edu/ece_etds/236

Rajeev V. Shenoi
Candidate

Electrical and Computer Engineering
Department

This dissertation is approved, and it is acceptable in quality and form for publication:

Approved by the Dissertation Committee:

, Chairperson

Steven Brueck

Sudhakar Prasad

Majeed Hayat

Multispectral Plasmon Enhanced Quantum Dots in a Well Infrared Photodetectors

by

Rajeev V. Shenoi

Master of Technology,
Indian Institute of Technology Madras,
Chennai, India, 2005

DISSERTATION

Submitted in Partial Fulfillment of the
Requirements for the Degree of

Doctor of Philosophy
Engineering

The University of New Mexico

Albuquerque, New Mexico

December, 2010

A drop in an ocean, but nevertheless a drop.

Acknowledgments

I would like to thank my advisor Dr. Sanjay Krishna, for his guidance, encouragement and support throughout the course of this work. I have learnt a lot from him. A man of great patience, he has put up with all my eccentricities and I hope that some of his ever optimistic attitude has rubbed on to me. It has truely been a great pleasure to work under his supervision. I would like to thank other members of my thesis committee, Dr. Steven R. J. Brueck, Dr. Sudhakar Prasad and Dr. Majeed Hayat, for their time and constructive comments during my dissertation proposal and defense.

Many thanks to Dr. Oskar Painter and Jessie Rosenberg at Caltech. It has been great collaborating with them. I have had a chance to learn a lot, least of all scientific rigor, by working with them. Some of the most interesting work, from a personal point of view, would not have been possible without the time, effort and patience of Dr. Aaron Gin at Sandia National Labs. I would like to thank him and other staff at CINT for their support during this work. Thanks to Dr. Tom Vandervelde at Tufts, who has been a great source of knowledge and strategy among other things. Tom has been of great help and his insights have helped me immensely in understanding epitaxial growth.

I would like to express my gratitude to Dr. Ralph Dawson, Dr. Kevin Malloy, Dr. Luke Lester and Dr. Stephen D. Hersee who have been great teachers here at UNM. It has been a great joy to attend their classes and a wonderful learning experience.

Furthermore, I am indebted to Dr. Yagya Sharma, Dr. Sang Jun Lee, Dr. S. C. Lee and Dr. Jay Brown for helping me get to my feet, during the early days here. I would like to thank other colleagues in my group for all the support and for providing a vibrant and diverse environment. Two friends, Maya and Tom, have been great colleagues as well. Their help, guidance and company at every stage of my life here, both personal and professional, is greatly appreciated.

None of this work would have been possible without the support of cleanroom staff, specifically Douglas, Steve, Beth and Rick. Their dedication, patience and energy has helped immensely to solve issues on the fly and to reduce the turn around time. Many thanks to Joe Sadler for a wonderful computer network and for patiently dealing with all my cryptic software and networking requests. Thanks to Dan, Kerry, Jannell, Tamara and Elmyra, there has not been much hassle to get things done at CHTM and ECE.

I would like to thank Navin and Arnab for being great roomates all along my stay here and for putting up with my erratic schedules. I would also like to thank Ashwin, Srikant, Wenyun, Vaibhav and Japji for the great company and thoughts they have provided. Special thanks to Bibin, Andhu, PR, Papps and Abu for those long discussions, everytime we have talked.

Thanks to Happle and Banoose, for all those conversations that have provided great relief, even during the most chaotic times. I am indebted to Prof. V. L. Antony, formerly of CMS College. None of this would have been possible without his guidance and inspiration. Finally I remember fondly my appa, amma and Reshmi, whose great sacrifices have brought me here.

Multispectral Plasmon Enhanced Quantum Dots in a Well Infrared Photodetectors

by

Rajeev V. Shenoi

ABSTRACT OF DISSERTATION

Submitted in Partial Fulfillment of the
Requirements for the Degree of

Doctor of Philosophy
Engineering

The University of New Mexico

Albuquerque, New Mexico

December, 2010

Multispectral Plasmon Enhanced Quantum Dots in a Well Infrared Photodetectors

by

Rajeev V. Shenoi

Master of Technology,

Indian Institute of Technology Madras,
Chennai, India, 2005

PhD, Engineering, University of New Mexico, 2010

Abstract

Infrared detectors in 3-5 μm and 8-12 μm regions are extensively used for applications in remote sensing, target detection and medical diagnostics. Detectors using intersubband transitions in the quantum dots in a well (DWELL) system for infrared detection have gained prominence recently, owing to their ability to detect normally incident light, bicolor detection and use of mature III-V technology. In this dissertation, two aspects of DWELL detectors that make them suitable for third generation infrared systems are discussed: 1) High temperature operation, 2) Multispectral detection.

There are two parts to this dissertation. In the first part, an alternate structure with an improved operating temperature and thicker active region is presented. Traditionally, DWELL detectors use InAs quantum dots embedded in $In_{0.15}Ga_{0.85}As$ wells with GaAs barriers. Intersubband transitions in the conduction band of this system result in infrared detection. InAs quantum dots are grown using self assembly on a GaAs substrate for this system. The strain of the quantum dots and the $In_{0.15}Ga_{0.85}As$ well limits the thickness of the active region. An improved design that minimizes the strain in growth of DWELL active region is discussed. By minimizing the amount of $In_{0.15}Ga_{0.85}As$ in the quantum well, a lower strain per DWELL active region stack is achieved. This design consists of InAs dots in $In_{0.15}Ga_{0.85}As$/GaAs wells, forming dots-in-a-double-well (DDWELL) is presented. Optimization using PL and AFM is discussed. Detectors fabricated using DDWELL design show an operating temperature of 140 K and a background limited performance at 77 K. A peak detectivity of 6.7×10^{10} $cm.\sqrt{Hz}/W$ was observed for a wavelength of 8.7 μm.

In the second part of this dissertation, multispectral and polarization detectors using DWELL absorbers are discussed. Integration of a subwavelength metallic pattern with the detector results in coupling of surface plasmons excited at the metal-semiconductor interface with DWELL active regions. Simulations indicate the presence of several modes of absorption, which can be tuned by changing the pitch of the pattern. Enhancement of absorption is predicted for the detector. Experimental demonstration show spectral tuning in MWIR and LWIR regions and a peak absorption enhancement of 4.9×. By breaking the symmetry of the fabricated pattern, we can extract a polarization dependent response, as shown from device measurements. The technique used is detector agnostic, simple and can easily be transferred to focal plane arrays (FPA). Integrating plasmonic structures on detectors using low noise DDWELL active regions can provide a higher operating temperature and high absorption.

The origin of resonant peaks in multispectral DWELL detectors is examined. Use of surface patterns that selectively excite different types of modes, with absorbers of different thicknesses, show the presence of enhancement mechanisms in these devices. A 2.2× enhancement is measured from waveguide modes and 4.9× enhancement is observed from plasmon modes. Finally, a pathway of integration with FPA and integration with other infrared technologies is discussed.

Contents

List of Figures

List of Tables

Chapter 1

Introduction

Infrared (IR) radiation is part of electromagnetic spectrum having a wavelength longer than that of visible light, but shorter than radio waves. Human eye is sensitive to radiation ranging from 400 nm to 700 nm. The IR region covers wavelengths between ≈750 nm and 1 mm, spanning five orders of magnitude [1]. Any object with a temperature above 0 K emits electromagnetic radiation as given by Plank's law. The spectral radiant emittance (power per unit area per unit wavelength) of a blackbody is given by

$$W = \frac{2\pi hc^2}{\lambda^5}\frac{1}{\exp\frac{hc}{\lambda kT} - 1} \tag{1.1}$$

where W is the spectral radiant emittance, k is Boltzmann's constant, h is Plank's constant and c is speed of light. A plot of blackbody radiation at 300 K is shown in Figure 1.1. Most objects with temperatures near 300 K emit in the IR and this forms the basis of IR detection. As imaging is the major application of IR detectors, transmission through atmosphere plays a crucial role in the development of detection schemes for terrestrial applications. A plot of atmospheric transmission with wavelength is shown in Figure 1.2. The presence of several high transmission spectral windows has led to concentrated efforts in the development of detectors for these regions. The IR spectrum is divided into several bands for convenience, as shown in Table 1.1. In this work, we will confine ourselves to mid-wave infrared (MWIR) and long-wave infrared (LWIR) regions. For objects close to 300 K, the peak of spectral radiance falls in LWIR region, while the high sensitivity region falls in MWIR region.

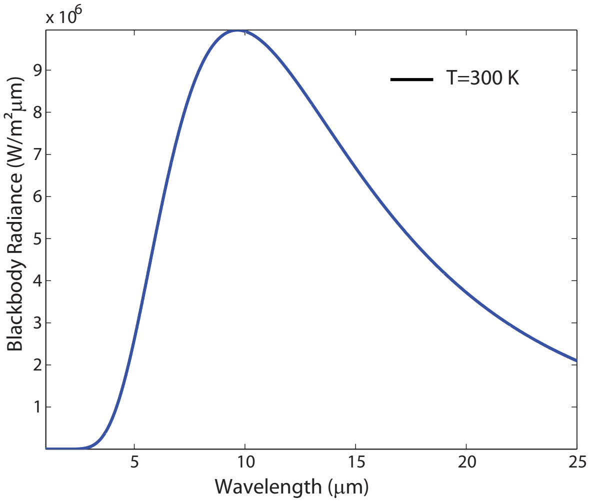

Figure 1.1: Radiation from a blackbody at 300 K [2].

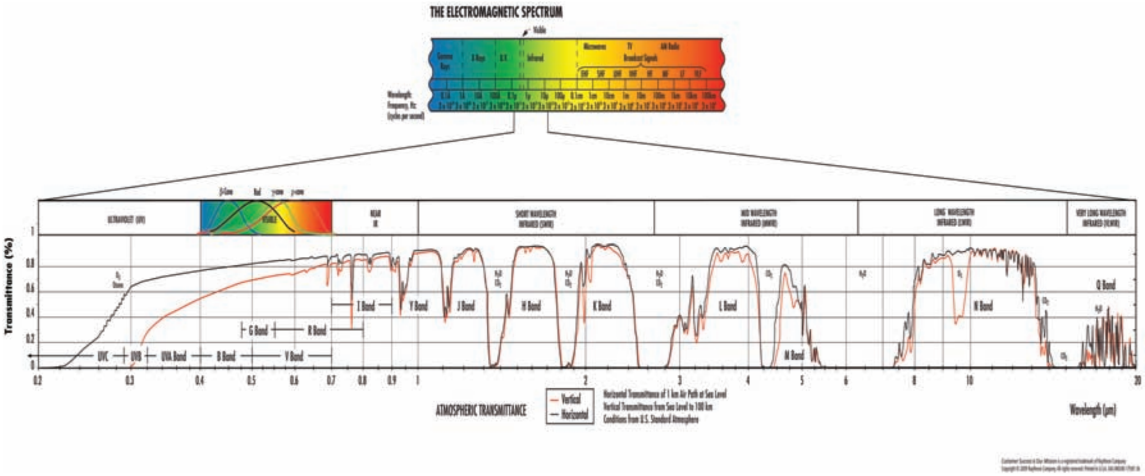

Figure 1.2: Atmospheric transmission as a function of wavelength [3].

Wavelength (μm)	Category
0.7-1.0	Near infrared (NIR)
1.0-3.0	Short-wave infrared (SWIR)
3.0-5.0	Mid-wave infrared (MWIR)
8.0-14.0	Long-wave infrared (LWIR)
14.0-30.0	Very-long wave infrared (VLWIR)
30-1000	Far infrared

Table 1.1: Classification of the infrared spectrum. The type of detectors used in each band forms the basis of classification.

The prominent applications of IR detection include night vision, thermography, target tracking, IR heating, trace gas detection and communications. The example shown in Figure 1.3 illustrates the thermographic image of a dog. The image has been false-colored with respect to the temperature of the body. Optical communication systems worldwide use wavelengths in SWIR region for data transmission.

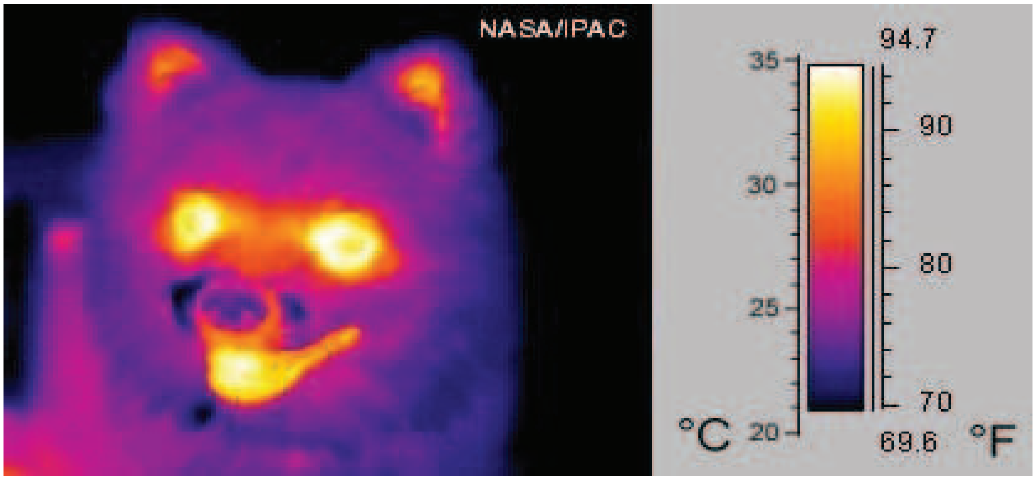

Figure 1.3: Thermographic image of a dog [4].

1.1 Infrared Detectors

Infrared detectors fall into two classes : Thermal detectors and Photon detectors.

In a thermal detector, incident radiation is absorbed to change the temperature of the constituent material, and the resultant change in a physical property is used to generate an electrical output. Thermal effects are generally wavelength independent; the signal depends upon radiant power but not on its spectral content. In pyroelectric detectors a change in internal spontaneous polarization is measured, whereas in the case of bolometers a change in electrical resistance is measured. An advantage of thermal detectors is that they operate at room temperatures and hence are exempt from stringent cooling requirements of photon detectors that add to their cost. These devices, however, exhibit low responsivity and have a slow response time.

In photon detectors, radiation is absorbed within the constituent material by interaction with charge carriers. The observed electrical output signal results from changes in the electronic energy distribution. Photon detectors show a selective wavelength dependence of response per unit incident radiation power. This can be utilized to obtain spectral information of the image and for multi-color detection. In general, photon detectors exhibit both an improved signal-to-noise (SNR) and a very fast response when compared to thermal detectors. To achieve this, photon detectors require cryogenic cooling. This makes them bulky, heavy, expensive and inconvenient to use.

Present day IR photon detectors use both intrinsic and extrinsic materials for detection. The state-of-the-art systems in LWIR use mercury cadmium telluride (HgCdTe). It is possible to tune the bandgap of HgCdTe by changing the composition of Hg and Cd, which makes the material system attractive for use in a wide range of wavelengths. High quantum efficiency (QE) associated with the use of bulk materials is another advantage. Higher life times in the HgCdTe system reduce dark currents and provide an improved SNR. The major drawback of HgCdTe based systems is associated with material growth. The weak Hg-Te bond results in bulk and surface interface instabilities. Stringent conditions are needed for good quality material. Large area uniformity is another issue that becomes important in the development of focal plane arrays (FPA). Variations in composition of the alloy across large sized wafers leads to changes in response wavelengths.

For MWIR detectors InSb is the preferred material. InSb detectors have a cut-off wavelength of ≈5.5 μm. A diffused p-n junction can be used for detection in the MWIR region. A simple processing scheme and superior performance make InSb an attractive material for large sized (4 K×4 K) FPAs. The lack of tunability in the cut-off wavelength and a stringent cooling requirement are issues with InSb based systems.

Extrinsic detectors are widely used in IR applications, due to their ability to detect light of energy lower than the semiconductor bandgap. Since it is possible to use a larger bandgap material as the active region, efforts have been directed to utilize mature growth and processing technologies from III-V semiconductors to achieve high quality material and detectors [5]. For detectors with small energy bandgaps, electrons can be thermally excited into the conduction band, generating dark current. This results in a high noise current in devices. Based on Boltzmann's distribution, the population of the energy levels follows an exponential distribution, $e^{-E_g/kT}$. As E_g becomes smaller (while temperature T is constant), the number of thermally generated carriers increases exponentially [6]. The detector has to be cooled to a cryogenic temperature to prevent thermal carriers from dominating photo carriers. In addition, extrinsic photoconductors also suffer from low QEs when compared with intrinsic photoconductors. This is due to low absorption cross sections for intrinsic materials, resulting from low volumetric density of extrinsic dopant species compared to the host material. Quantum well infrared photodetectors (QWIP) and quantum dot infrared photodetectors (QDIP), which are examined in detail in section 1.3, are examples of extrinsic photodetectors.

1.2 Focal Plane Arrays

1.2.1 Historical Perspective

Two dimensional (2D) arrays of pixels (normally square) are currently used in infrared systems for image acquisition. Several generations of arrays have evolved, mostly based on their functionality.

1950-1970

First generation FPAs (also known as scanning arrays) had linear arrays of detectors for imaging. A mirror was used to scan in the second dimension, to create a video image. The resolution of these systems was dependent on detector pixel sizes and scanning rates. First generation systems had low frame rates and were not suitable for high speed imaging.

1970-2000

Second generation systems (or staring arrays) developed from 1970-2000 used medium sized two dimensional arrays for imaging. Arrays of size 320 × 256 were very common. These systems deliver higher performance when compared to first generation systems. Both first and second generation systems are single color detection schemes: They recognize the intensity difference within their detection band, without the ability to discern specific wavebands. All these detectors need to be cooled for optimized performance. Second generation arrays are integrated with silicon based read out integrated circuits (ROIC), which are used to extract image information from each pixel and reconstruct the image.

2000-Present

The use of identification of targets rather than mere detection necessitated improved viewing range for infrared systems [7]. The most obvious method to improve the range of an FPA is to improve its spatial resolution i.e, large format FPAs. Another option is to introduce different spectral bands of sensing and to use images captured in different bands for identification. Moreover, multi-spectral detection helps in discerning features with responses in specific wavebands. Different spectral bands provide another dimension in contrast and help in cases where the intensity difference between a scene and its background is too low for a successful distinction between the two. Reducing colling cost, by improving operating temperatures, is another desired feature of future infrared systems. An improved signal to noise ratio for the array is necessary to raise its operating temperature. Higher frame rates, leading to high speed imaging, is another requirement for a third generation array.

The requirements of a third generation infrared system can be summarized as follows

1. Large format arrays
2. High frame rates
3. Higher operating temperature
4. Multicolor functionality

This thesis addresses two aspects of third generation arrays: Higher operating temperature and multicolor functionality.

1.3 Quantum Dot Infrared Detectors

1.3.1 Quantum Dots

When the dimensions of a semiconductor structure approach that of electron wavelengths, quantum effects are observed in electronic properties. Confinement in one, two and three dimensions to the order of electron wavelength results in formation of quantum wells, quantum wires and quantum dots respectively. A schematic of the confinement in one dimension is given in Figure 1.4. Here a lower band gap material is sandwiched between higher band gap materials resulting in the formation of a potential well [8]. The conduction band edge energy of lower band gap material lies nested in the band gap of two confining layers. As a result electrons and holes are confined in middle layer by the barriers.

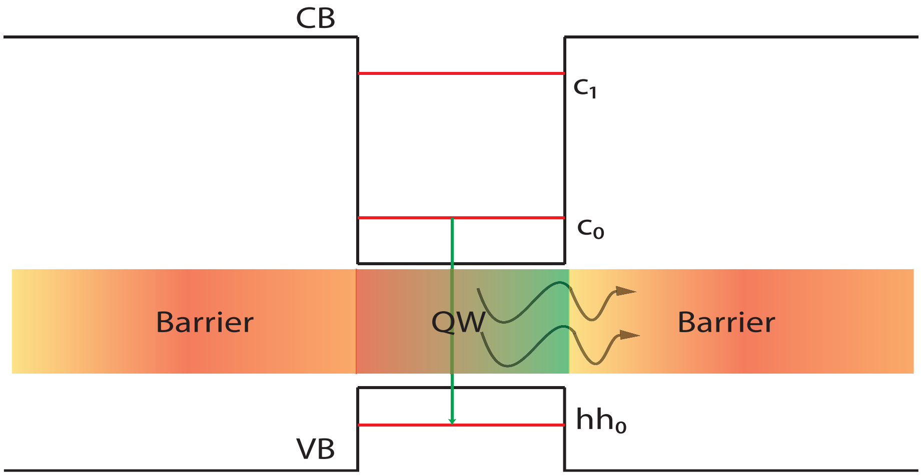

Figure 1.4: Schematic of a Quantum Well [9].

The density of electronic states of a material change significantly upon quantum confinement. As quantum confinement increases, electronic states are discretized. The change in density of states function with degrees of confinement (to form quantum wells (1 dimension), quantum wires (2 dimension) or quantum dots (3 dimension)) is illustrated in Figure 1.5.

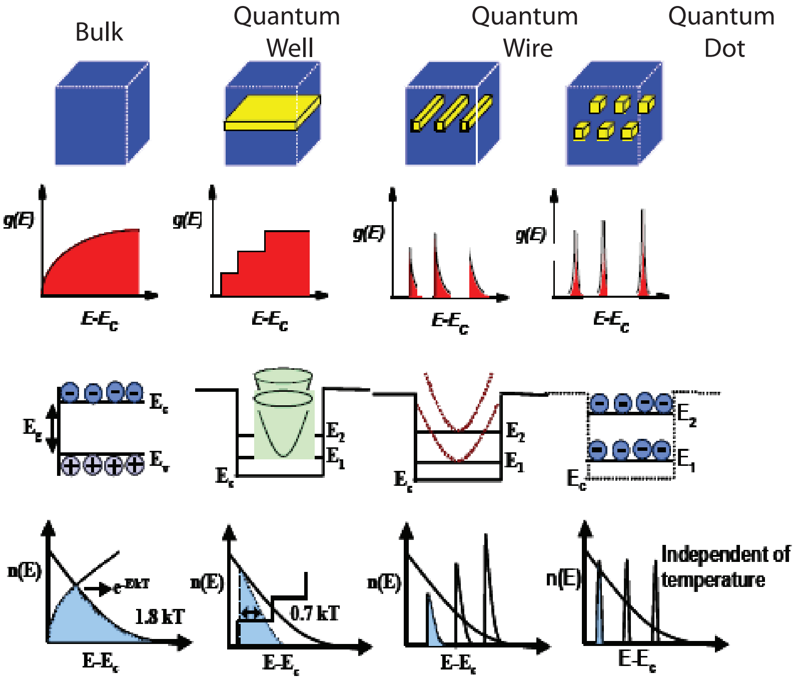

Figure 1.5: Density of states, band structure and carrier distribution for bulk materials, quantum wells, quantum wires and quantum dots[10].

As we go to confinement in higher dimensions, change in the density of states enables use of fewer carriers to invert carrier populations, which results in low threshold current density and high characteristic temperature, when incorporated as the active region in a laser. In terms of detectors, absorption of dots can be easily saturated due to finite density of states. Transitions between discretized energy states in the conduction and valence bands can be used for detection. For intersubband transitions, the energy difference between states is low and wavelengths of detection would fall primarily in IR region.

The size of quantum dots is an important parameter to be considered during device modeling to have good quantum confinement. There is a lower limit on the size of dots, which is obtained from the condition that there should be at least one bound energy level for electrons or holes. Solving Schrodinger's wave equation, with a spherical dot assumption and taking the minimum potential for a general particle in a box, the minimum size of the dot can be found out to be

$$D_{min} = \frac{\pi\hbar}{\sqrt{2m_e^*\Delta E_c}} \tag{1.2}$$

where m_e^* is the effective mass of the electron and ΔE_c is the confinement potential. For a conduction band offset of 0.3 eV this gives a dot size not smaller than 4 nm. Similarly there is an upper limit on the size of dots, considering that thermal population in higher levels should not be more than 5%. This gives the following condition to be satisfied to have good quantum confinement [10].

$$\frac{1}{3}(E_2 - E_1) > kT \tag{1.3}$$

where E_2 and E_1 are the energies of the second and first excited states respectively. This equation limits the maximum size of dots in GaAs/AlGaAs quantum dots system to be ≈12nm and InAs/AlGaAs to be ≈20nm at room temperature.

Growth of Quantum Dots

Self assembly is the preferred growth method for semiconductor quantum dots. This is achieved through growth of a lattice mismatched layer on a substrate. When a lattice mismatched epitaxial layer is grown, strain is developed in the system. When this strain is low there is a normal 2D layer growth as shown in Figure 1.6, called Frank van der Merwe growth. As lattice mismatch between two materials increases, strain energy increases. When the thickness of grown materials exceeds a certain value (known as 'critical thickness'), there is a coherent three-dimensional (3D) island formation, referred to as Stranski-Krastanow process [11]. If the lattice mismatch is very high then there is direct formation of 3-D islands, a growth mode known as Vollmer-Weber process [12]. Most of present day devices have quantum dots grown using Stranski-Krastanow mode. Molecular beam epitaxy (MBE) or metal organic chemical vapor deposition (MOCVD) is used as the growth process.

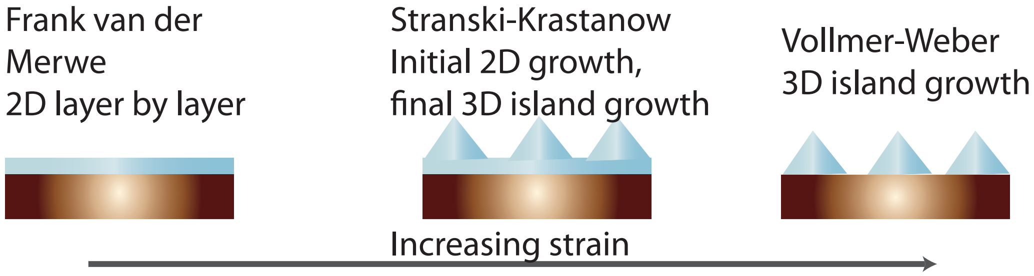

Figure 1.6: Three modes of heteroepitaxial growth[13].

.

Characteristics of Quantum Dots

Quantum dot devices can be tailored to provide superior performance by taking advantage of the large density of states function that increases the abundance of available levels in a given volume. Zero dimensional semiconductor systems with a discrete density of states exhibit a phonon bottleneck, or a suppression of carrier relaxation rates [14]. If the energy level spacings are sufficiently large, then the rate of phonon-mediated scattering processes will be inhibited, as energy and momentum conservation forbids transitions mediated by a single phonon emission. Semiconductor self-assembled quantum dots exhibit strong three-dimensional carrier confinement and show discrete energy spectra. Hence relaxation rates among the electronic levels of these quantum dots would be low [15]. We can therefore expect long carrier relaxation times and hence more probability of the electrons being found in the excited state. This in turn provides longer lifetime for photo-excited electrons due to reduced electron-phonon scattering and a lower dark current [16].

1.3.2 Quantum Dot Infrared Photodetector (QDIP)

Infrared detection using quantum confined structures offer a great potential, as inter-subband transitions within energy levels can be utilized to detect light in the IR regime. Quantum well infrared photodetector (QWIP), quantum dot infrared photodetector (QDIP) and strained layer superlattice (SLS) are the most common of IR detectors using quantum confined structures. QWIPs and QDIPs are extrinsic detectors that use inter-subband transitions from the dot/well to detect IR radiation. QWIPs use transitions in quantum well for detection while QDIPs use transitions in quantum dots for detection. An illustration of the use of intersubband transitions for detection is shown in Fig. 1.7, using InAs quantum dot with a GaAs barrier as an example. Since these devices use III-V semiconductors, the mature growth technology of III-V semiconductor growth can be used to obtain uniform material over a large area. This is extremely important in production of large area FPAs.

QWIP technology has developed into a mature one and is already in use in commercial IR FPA systems [5, 17]. Selection rules forbid the absorption of normally incident light in QWIPs. Thus, gratings or edge coupling schemes are required to absorb normally incident radiation. This makes the processing complex [18]. The QE of QWIP systems is also low, necessitating the use of cooling systems that make it expensive. QDIPs have been considered as one of the next generation IR technologies, due to their ability to absorb normally incident light, inherently lower dark current leading to a higher temperature operation and high relaxation times that lead to a higher photoconductive gain in the system [19–25]. QDIPs have been reported to operate at higher temperatures and room temperature operation has been reported at lower wavelengths recently [22, 26]. FPAs based on QDIP technology have been developed and single pixel performance has been replicated in large sized arrays [27–29]. Arrays are fabricated using quantum dot active regions in InP/GaAs substrates and are then flip-chip bonded into a silicon read-out integrated circuit (ROIC). The bonding to ROICs is done using pressure contacts via indium bumps. Illumination of arrays can be done from either frontside or backside.

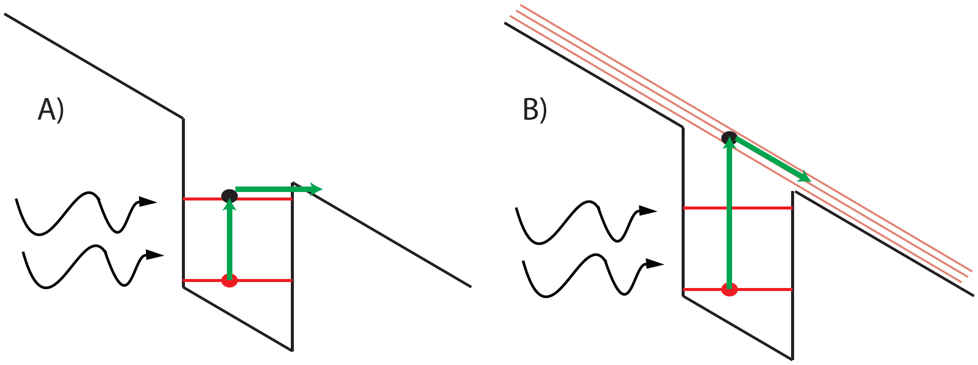

Figure 1.7: Transitions in a QDIP.

.

Despite these advantages, the demonstration of high absorption in QDIPs has been elusive due to the identical transport paths that exist for photocurrents and dark currents. Therefore, heterostructure designs developed to minimize the dark current, such as the insertion of a single AlGaAs barrier outside the active region, also prevent the efficient collection of carriers contributing to the photocurrent, resulting in low responsivity values [16, 30]. Self assembled growth of QDIPs creates another challenge in reproduction of spectral characteristics. Since the growth is a self assembled process, the dots formed differ from each other in size and shape. This changes the potential distribution from dot to dot and results in variation of eigen states and the oscillator strengths. Hence control of the operating wavelength becomes difficult [31]. Quantum dots-in-a-well (DWELL) detectors have been proposed to alleviate this drawback of QDIPs.

1.3.3 Quantum Dots-in-a-Well Photodetector (DWELL)

DWELL detectors represent a hybrid between a conventional QWIPs and QDIPs. In this structure quantum dots are placed inside a quantum well. In a DWELL structure, electrons in the ground state of QDs are promoted to a set of bound/quasi-bound states within quantum wells by photoexcitation. These electrons constitute the photo-current and form the basis of IR detection. Apart from lower dark currents, detectors using DWELL designs demonstrate a better control over the operating wavelength and nature of the transition (bound-to bound versus bound-to-continuum), as discussed in [31, 32]. High photoconductive gains observed in the DWELL design lead to improved responsivity for detectors [33]. A typical DWELL band diagram and the spectral response obtained from fabricated detectors is shown in Figure 1.8.

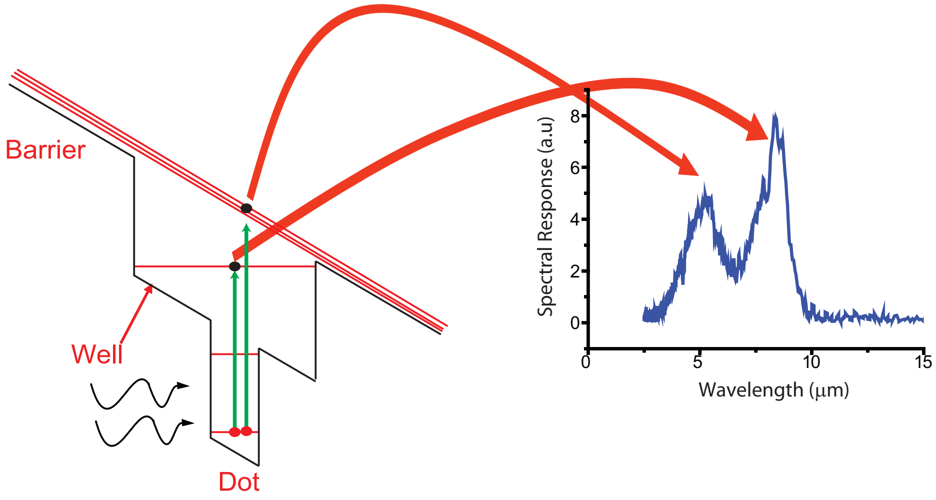

Figure 1.8: Band diagram of DWELL detector. The measured spectral response from detectors and the transitions that result in the response are also shown.

In DWELL designs, quantum dots are embedded within (a) quantum well(s), and a suitable barrier of higher bandgap is used to reduce dark current. The device shows a dual-color response which arises from two dominant transitions within the conduction band. There is a short wavelength peak due to electron transitions from the ground state of the dot to the continuum. The other peak is found in longer wavelength regions of the spectrum and is due to electron transitions from ground state of the dot to states in the quantum well [34, 35]. Bound to continuum transitions are dominant when the applied voltage is small. As the voltage increases, the peak shifts toward longer wavelength regions indicating that the energy gained now is sufficient to collect a bound to bound transition. This change of spectral response with bias has been exploited to make voltage tunable detectors [36, 37]. The operating wavelength of the DWELL structure can also be tuned by changing thickness of the quantum well [31]. Hence, instead of changing the whole growth process, thickness of the quantum well can be modified to obtain desired wavelengths. Another characteristic of the DWELL is dependence of peak wavelength on the bias polarity applied. A DWELL structure with an asymmetrically designed well exhibits quantum controlled Stark effect (QCSE). This results in bias polarity dependent spectral responses and can be exploited to provide spectrally adaptive detectors.

The DWELL design has been successfully incorporated into FPAs. Focal plane arrays of sizes 1024×1024, 640×512, and 320×256 have been demonstrated using DWELL technology [27, 29, 38, 39]. Two-color response observed in single pixel detectors has been demonstrated in FPAs also [39, 40]. It should be noted that DWELL FPAs display a two color response using a single indium bump only, which would simplify processing considerably, when compared to two-color FPAs that use more than one indium bump. An image obtained from the 320×256 FPA at 60 K is shown in Figure 1.9. This FPA demonstrated a noise equivalent temperature difference (NEDT) of 80 mK at a temperature of 77K [39, 41].

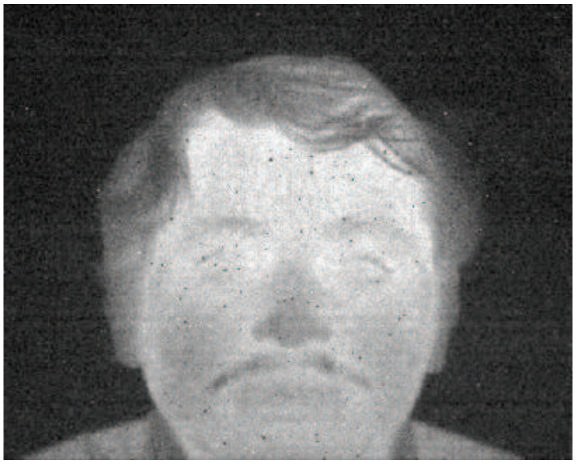

Figure 1.9: Image obtained from a standard DWELL based 320×256 FPA.

1.4 Objective of this Dissertation

The objective of this work has been to demonstrate

1. High operating temperature (HOT) DWELL infrared detectors.
2. Multispectral and polarization sensitive infrared detectors with enahnced absorption.

The following are the significant contributions of this thesis 1) Demonstration of a quantum dots in a double well (DDWELL) infrared detector, working at 140 K with a wavelength of 8.7 μm. 2) Integration of surface plasmon based cavities with DWELL detector. 3) Design of multispectral and polarization dependent infrared detectors. 3) Demonstration of enhanced absorption with multispectral and polarization sensitive detection 4) Analysis of enhancement mechanisms in plasmon integrated infrared detectors.

At the beginning of this work, DWELL systems using InAs dots were demonstrated in the MWIR and LWIR infrared regions, The dark current levels of DWELL detectors were higher than those of QWIPs and they had a QE lower than that of QWIP systems. This is attributed to the low absorption cross-section of these devices [30]. The thin absorption region in the surface normal direction is another reason for low responsivity of DWELLs. Self-assembled growth of QDs needs strain in the system and this limits the layers of active region grown before defects set in. The low fill factor of QDs (25% to 28% for a QD density of $\approx 5 \times 10^{10} cm^{-2}$) is another reason [24]. As the quantum dots are self assembled during growth, it is not possible to control the size with precision. The actual emission spectra in detectors occurs from an ensemble of dots, each different from the other. This results in broadening of emission spectrum and limits use of DWELLs in multi-spectral and hyper-spectral arrays.

Various methods have been suggested to improve performance and functionality of DWELLs. Doping of dots with Si has resulted in an improved response from DWELL detectors [42]. The integration of a DBR or photonic crystal resonant cavities with IR detectors to facilitate higher absorption is another technique [43, 44]. These systems to allow multiple passes of light in the active region and improve the absorption. This resulted in a six fold increase in responsivity [43]. However the spectral response of the system still shows a broad peak as the resonant cavity has a low quality factor (Q). Another technique is the use of an APD in conjunction with the DWELL to introduce gain in the system [45]. The use of resonant tunneling barriers that extract photo-excited carriers preferentially and inhibit the collection of dark carriers has been used in both QDIPs and DWELL systems to improve SNR [24, 46].

In Chapter 2, growth of thicker active regions for DWELL structures to improve their operating temperature is investigated. The strain accumulated in the DWELL layer, as result of growth of InAs dot and InGaAs well regions is the factor limiting active region thickness. A new design that reduces the thickness of strained quantum well regions is discussed. In this design, InAs quantum dots are embedded in InGaAs/GaAs wells, with GaAs forming the primary well. Optimization and characterization of this design is presented. Detector structures were grown using this design and their performance is examined. The use of an improved design resulted in higher operating temperatures of 140 K for detectors in the LWIR region, without sacrificing any of the characteristics of DWELLs.

In the second part of this dissertation, encoding of spectral and polarization information within a detector pixel is discussed. Present day infrared systems use bulky and expensive external components to provide multi-spectral detection. One method is to use a broadband FPA in conjunction with a dispersive prism to limit spectral range of radiation on FPAs. The other is to use external filters to select desired wavebands. Both these methods need precise optical alignment and components, as array sizes increase. This increases the cost of multi-spectral infrared FPAs manyfold. As a result, the current 30-50 band multi-spectral arrays cost $10-15 million. A limited multi-spectral capability; viz. dual color detection, can be achieved in arrays using back to back biased diodes [47, 48], or by asymmetric design of absorbing regions [31] that detect multiple wavelengths by changing the bias polarity. The contents of this chapter were originally published in refs. [13, 49–53]

In Chapter 3, a novel method to fabricate spectral and polarization dependent infrared detectors is presented. By integrating subwavelength metal nanostructures with infrared detectors, spectral and polarization characteristics of the detector can be tuned. A finite difference time domain (FDTD) based modeling is presented that predicts the absorption of a DWELL based detector integrated with nanostructures. An enhancement of the absorption and tunability of absortion are predicted. The fabrication and characterization of these detectors is discussed. Spectral tuning and enhancement of absorption is observed in MWIR and LWIR regions. A method to fabricate polarization sensitive detectors, by modifying the surface pattern, is analyzed and demonstrated.

Chapter 4 of this dissertation focuses on origin and mechanisms of spectral tuning and enhancement in plasmon assisted DWELL detectors. Analysis resonant peaks observed from devices in chapter 3 is performed. The spatial and spectral extent of electric field intensities obtained from FDTD simulations are used to classify the modes. Two enhancement mechanisms are observed in these devices: Plasmon modes and waveguide modes. Selective excitation between plasmon modes and waveguide modes is accomplished by use of surface patterns that excite one set of modes preferentially over the other. Detector structures with different active region thicknesses were designed and fabricated to couple these modes with the DWELL absorption. Experimental observations are discussed in detail and they indicate presence of several modes of absorption. This work was originally published in refs. [54–60].

Chapter 5 summarizes some of the most important results and discusses some of the future directions. Specifically, integration of surface plasmons with other IR technologies is discussed by using SLS as an example. The fabrication of surface plasmon based FPAs is also discussed. In this context, a double metal waveguide (DMWG) based structure, which improves the mode confinement within the cavity and has a fabrication methodology which can be directly integrated with FPAs, is proposed.

Chapter 2

Quantum Dots-in-a-double-well Infrared Detectors

2.1 Introduction

In recent years, several groups have investigated the use of dot-in-a-well designs for infrared detectors in MWIR and LWIR regions. In general, the DWELL system consists of quantum dots embedded in a quantum well, followed by a barrier layer. Two prominent DWELL systems that were in use, at the beginning of this work, for detectors were InAs/InGaAs/InAlAs system and InAs/InGaAs/GaAs systems [25, 29, 31, 61]. In these designs, growth of QDs is a self-assembled process. Formation of 3D islands of InAs is due to lattice mismatch with the substrate used. The lattice mismatch limits the number of stacks of active region that can be grown. Thus, infrared detector technologies using quantum dots have a lower thickness of active regions, when compared to bulk systems like HgCdTe or nearly lattice matched systems like GaAs/AlGaAs.

In the InAs/InGaAs/InAlAs system, InAs dots are embedded in an InGaAs layer followed by an InAlAs barrier. In this system the barrier is tensile strained, while the dot and the well are compressively strained. This offers a unique advantage to this system: strain compensation. With the growth of each stack of active region, the barrier compensates the strain introduced by the dot and the well. Thus growth of higher number of active region stacks is possible in this system [61]. Detectors fabricated using this system show a response at 4.1 μm. The lower wavelength of operation of these systems offer a better SNR and a better absorption coefficient. Detector structures with a peak detectivity of 2.8×10^{11} cm.$\sqrt{(\mathrm{Hz})}$/W at 77K and a QE of 35% have been observed in this system [62].

The InAs/InGaAs/ GaAs system consists of InAs dots embedded in $\mathrm{In_{0.15}Ga_{0.85}As}$ wells with GaAs barriers, on a GaAs substrate. Due to the higher lattice constants of InAs and InGaAs, the entire DWELL region is compressively strained in this system. The average indium composition in this system is around 19% [63] and the number of stacks that can be grown is limited to 12-15. Detectors grown using this system have been operating in the MWIR and LWIR region. In this chapter, the efforts to reduce the strain in this system to increase the active region thickness and performance improvements resulting from this change are discussed.

2.2 Optimization of Structure

Growth of lattice mismatched indium containing layers on GaAs is the primary reason for limited active region thickness. Strain reduction is achieved by reducing the overall indium content in the system, leading to a lower strain per layer. The development of this design required several cycles of optimization where the dot, well sizes above and below the dot, and the barrier thickness were optimized. This was achieved through a series of characterizations where the parameters above were varied and photoluminescence (PL) and atomic force microscopy (AFM) were used to optimize the structure. It is to be noted, however, that the transitions that result in infrared absorption are intersubband in nature, while the transitions that result in PL are from band to band. Thus a strong PL is a necessary but not a sufficient indicator of a good detector device.

Initially, several calibration samples were grown for optimization. A schematic of the calibration sample grown is shown in Figure 2.1. In general, samples consisted of InAs dots embedded in two quantum wells. A very thin layer of $In_{0.15}Ga_{0.85}As$, far below the thickness used in standard InAs/$In_{0.15}Ga_{0.85}As$/GaAs DWELLs, was used above and below the quantum dot region. The primary well in this system is GaAs, and $Al_{0.10}Ga_{0.90}As$ was used as the barrier. The emitted PL was collected and collated using two lenses, and an InGaAs detector was used in conjunction with a monochromator to measure the amount of signal and spectral content.

Initial attempts were made to use a GaAs well along with an InAs QD to form the DWELL structure, without the $In_{0.15}Ga_{0.85}As$ strain bed below the QD, This, however, was not found to be effective as the structure showed poor PL intensity. The QD density of the structure was also very low at $10^9/\text{cm}^{-2}$. Gallium-indium exchange, leading to a graded bandgap or a loss of dot confinement, may be the reason for loss of optical quality. Hence, a minimal $In_{0.15}Ga_{0.85}As$ layer was reintroduced between GaAs well and the dots. The InAs dots were then formed over the $In_{0.15}Ga_{0.85}As$ layer, instead of the GaAs well. The QD density was increased by two orders of magnitude as a result of this change.

The GaAs well width under the dot is critical as dots are essentially formed over GaAs/ $In_{0.15}Ga_{0.85}As$ wells.. Since the objective is to minimize strain, the amount of $In_{0.15}Ga_{0.85}As$ has to be kept to a minimum and well thickness below the dot is essentially determined by the GaAs layer. The GaAs shoulder width under the QDs was varied from 1 nm to 4 nm and PL from these devices at RT was measured using a He-Ne laser. The structure used to optimize GaAs well width under the dot is shown in Figure 2.2. As seen from the measured PL in Figure 2.2, PL intensity improves as GaAs thickness is increased. For all the device structures, the net thickness of quantum well was limited to 4 nm, to keep the total thickness comparable to previously grown structures.

Figure 2.1: Baseline structure used for optimizing DWELL detectors. The GaAs layer under the dot and the $In_{0.15}Ga_{0.85}As$ capping layer above the dot were optimized using this structure.

The effect of capping dots with an $In_{0.15}Ga_{0.85}As$ layer was investigated for optimizing the QD optical response. Thickness of $In_{0.15}Ga_{0.85}As$ layer above the dots in Figure 2.1 was varied from 0 to 2 nm, and the change in PL observed is shown in Figure 2.3. It was observed that capping dots with InGaAs helps to improve PL. The increase of capping layer thickness from 1 to 2 nm, results in a minor improvement. For the final detector structure, it was determined that the increased number of QD layers that could be grown with a 1 nm cap would compensate for the slightly decreased PL.

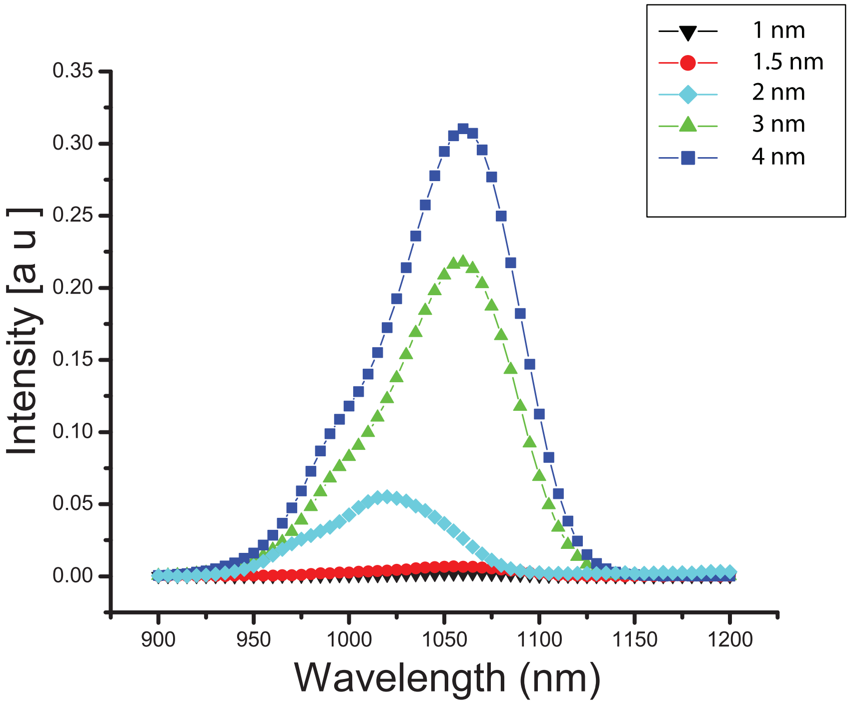

Figure 2.2: Photoluminescence intensity from structures with varying GaAs layer thickness under the dot.

The redshift seen in PL intensity plots of Figure 2.2 and Figure 2.3 may be due to the wider thicknesses which lead to a smaller quantum confinement. The effect of thickness of the GaAs layer above the dot has already been investigated and the optimized thickness is used for growing detector structures[36]. Thus a single stack of the optimized design consists of InAs dots sandwiched in $In_{0.15}Ga_{0.85}As$/GaAs wells and an $Al_{0.10}Ga_{0.90}As$ barrier. The wells and the barrier are present above and below the dot, forming a dots-in-a-double-well (DDWELL) region.

Once the design was optimized for PL, detector structures were grown with the optimized DDWELL design. Repetitions of DDWELL layers were sandwiched between two highly doped n-GaAs layers that serve as the top and bottom contact layers, see Figure 2.8. With the reduction in strain, the number of active region stacks was increased to 30, as opposed to 12 or 15 in InAs/$In_{0.15}Ga_{0.85}As$/GaAs

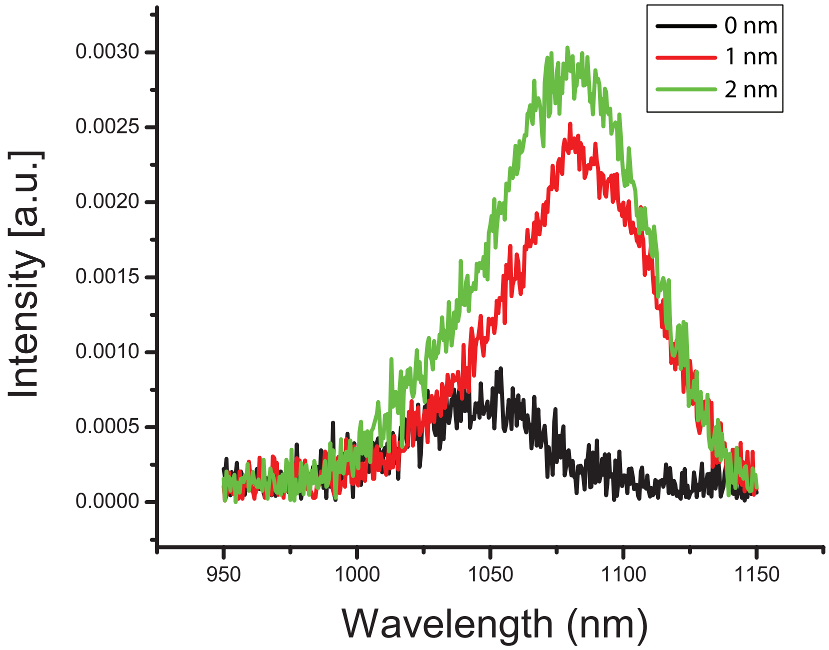

Figure 2.3: Photoluminescence intensity from structures as a function of quantum dot capping layer thickness. $In_{0.15}Ga_{0.85}As$ has been used for capping dots in this study.

DWELL detectors [42]. Attempts to grow higher number of stacks resulted in defects setting in, and did not provide good optical response. Three samples with barrier widths of 30, 50, and 65 nm were grown to optimize barrier width.

The samples were grown using a VG Semicon V80H solid source MBE reactor. $Al_{0.10}Ga_{0.90}As$ and GaAs layers were grown at a temperature of 590 °C. InAs dots and $In_{0.15}Ga_{0.85}As$ wells are grown at a lower temperature of 470 °C. A growth pause was applied during transition from a GaAs layer to $In_{0.15}Ga_{0.85}As$ strain bed under the dot, to facilitate lowering of the substrate temperature. The average dot density of DDWELL samples was found to be $4\times10^{11}/cm^2$. This is $\approx 3\times$ higher than the density for single well based DWELL samples. The QDs for the detector sample were doped to the order of 2e/dot, by opening the silicon shutter during QD formation. An AFM image, taken from exposed dots on the surface, from a 30 stack DDWELL sample is shown in Figure 2.4.

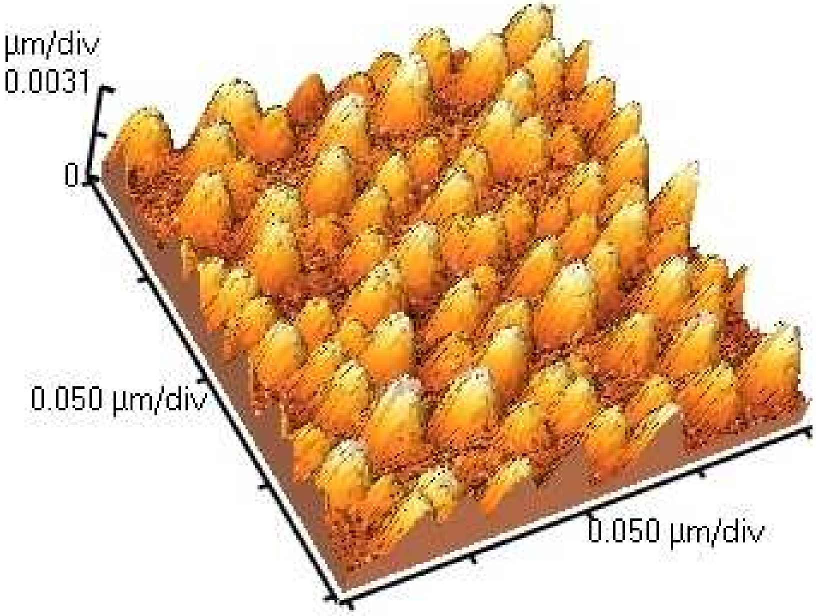

Figure 2.4: AFM image of exposed InAs dots, from a DDWELL design. An average dot density of $4\times10^{11}/\mathrm{cm}^2$ was measured for this sample.

In Figure 2.5 PL intensity from a standard InAs/ $In_{0.15}Ga_{0.85}As$ /GaAs DWELL design and a InAs/ $In_{0.15}Ga_{0.85}As$/GaAs /$Al_{0.10}Ga_{0.90}As$ DDWELL design at room temperature, measured by exciting with a He-Ne laser, is shown. The DDWELL design has a PL peak at 1095 nm and the DWELL design has a peak at 1245 nm. The changes in size and shape of QDs would be the primary contributors to this change. The lower PL wavelength also points to increased confinement. The response at longer wavelengths (>1300 nm) for the DWELL sample is due to exposed QDs on surface, used for AFM measurements. In order to observe the higher lying states of the DDWELL system, PL was measured using a pulsed Ti:Sapphire laser. The high intensity and short pulses from the Ti:Sapphire laser, create a high electron-hole pair (EHP) density per dot. As a result, the allowed band to band transitions between higher lying states in the conduction band and the valence band of this system can

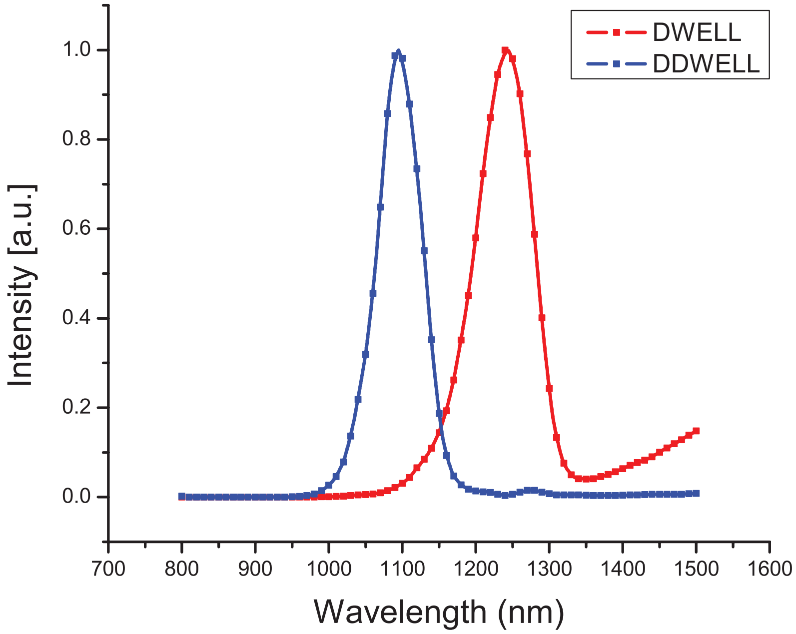

Figure 2.5: Normalized photoluminescence intensity from A) 30 stack DDWELL samples and B) 15 stack DWELL.

be observed. A plot of the observed PL spectrum at room temperature is shown in 2.6. Two dot to dot transitions and a transition between states in the quantum well (QW) can be observed. A schematic of the band diagram of the DDWELL structure is shown in Figure 2.7. A simple calulation based on a 60:40 band offset split between the conduction band and the valence band shows the intersubband transition to be 139 meV, which agrees well with the spectral response obtained in subsection 2.4.1.

2.3 Fabrication

Fabrication of detectors involved creating square mesa structures of sizes 410×410 μm^2 for electrical isolation. This was performed using a BCl_3 based dry etch in a class-100 clean room. A (optional) dip in a mixture of citric acid and hydrogen peroxide solution was performed after the dry etch to relieve the plasma induced

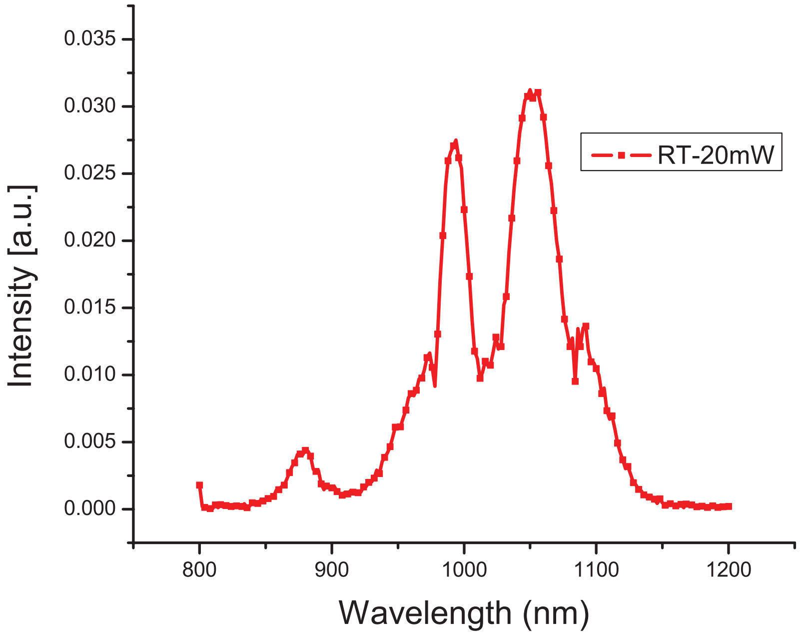

Figure 2.6: Room temperature photoluminescence measurements from DDWELL samples with a Ti:Sapphire laser. Higher lying dot states and well states are observed.

damage. This was followed by Ge/Au/Ni/Au metalization using an e-beam metal evaporator. The contact metal lithography also opens up top apertures ranging from 25 to 300 μm in diameter. The contacts were then annealed at a temperature of 380°C for 60s, using a rapid thermal annealer (RTA), to achieve ohmic contacts. An optional passivation step is also part of the process. SiNx deposited at 300° C using plasma enhanced chemical vapor deposition (PECVD) , is used as a passivant. This helps in long term stability and in limiting 1/f noise with age. Further details of the processing steps are provided in Appendix B. A schematic of the processed detector is shown in Figure 2.9.

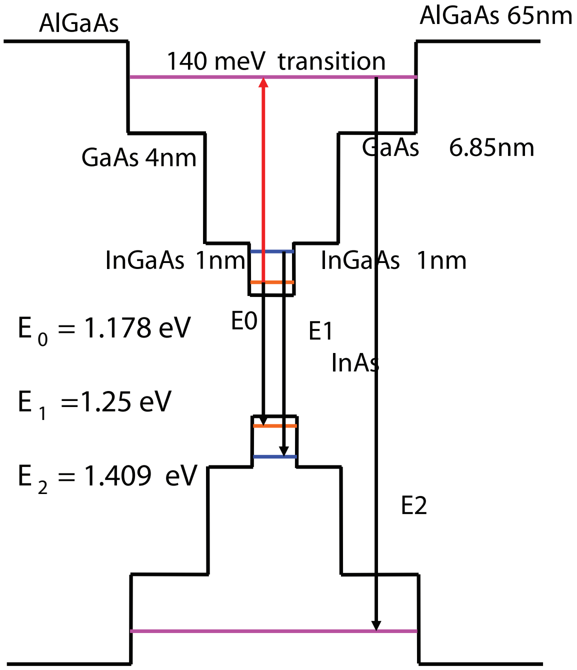

Figure 2.7: Schematic of the band diagram of DDWELL design, based on PL and spectral measurements. Two dot to dot transitions and a well to well transition is observed in the PL.

2.4 Characterization

The performance of an infrared detector is primarily evaluated through measuring its spectral content, signal, noise, photocurrent and dark current. In the case of an array, uniformity, pixel operability and minimum temperature difference that can be sensed are additional metrics used. A detailed description of the characterization methodology is provided in Appendix A.

2.4.1 Spectral Characteristics

The spectral response of detectors is measured using a Fourier transform infrared spectrometer (FTIR). Use of a FTIR helps in detecting low signals from the detector

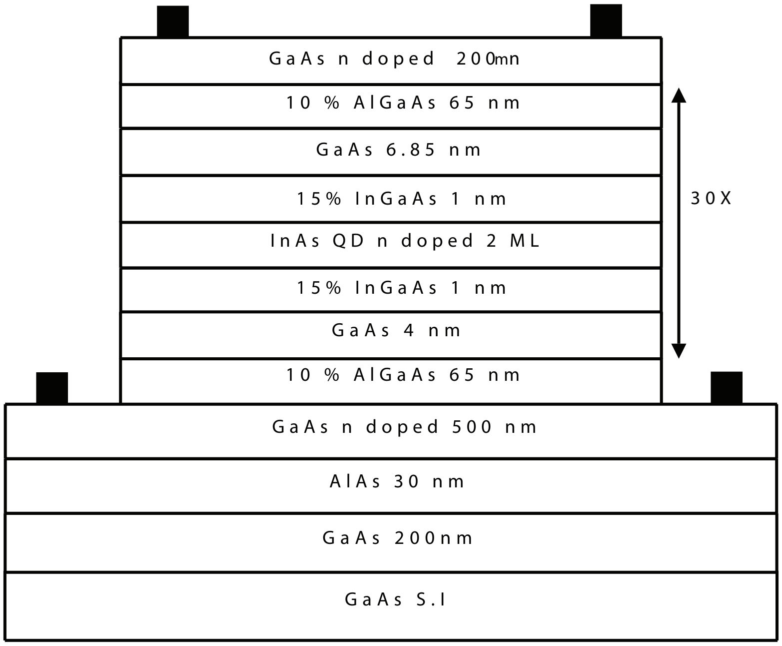

Figure 2.8: InAs/In$_{0.15}$Ga$_{0.85}$As/GaAs DDWELL structure comprising of 30 stacks of active region.

and provides a better spectral resolution, when compared to other spectral measurement techniques using a monochromator and a lock-in amplifier. The devices are cooled using either a liquid He based closed cycle cryostat or by using liquid nitrogen. Using these two cooling systems, measurements can be performed from 12 K to room temperature (RT).

Spectral measurements from devices fabricated with a DDWELL active region at a temperature of 30 K are shown in Figure 2.10, as a function of the applied bias. The spectral response shows two peaks at 9.4 μm and 6.8 μm for positive bias voltages and a much stronger peak at 8.7 μm for negative bias voltages. The LWIR peak is dominant at higher bias voltages, while the MWIR peak has a higher intensity at lower bias voltages. This could be due to the dot-to-well nature of the LWIR transition and the dot-to-continuum nature of the MWIR transition. Tunneling barriers for electrons excited by MWIR photons are lower. Thus, MWIR transitions dominate

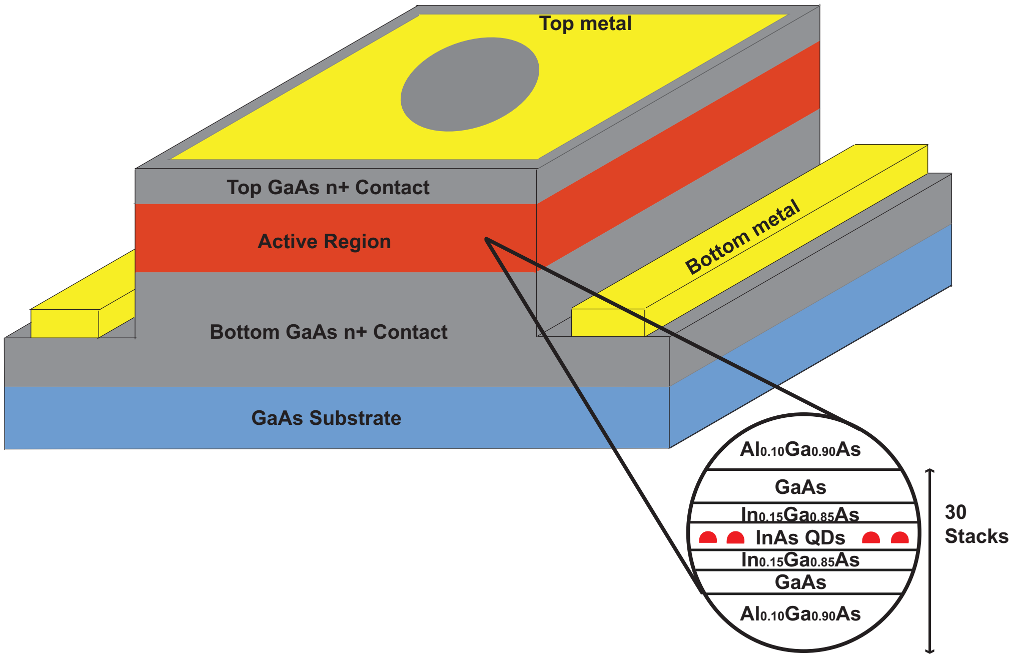

Figure 2.9: Schematic of the fabricated detector structure with the top and bottom contacts and the aperture.

the spectrum at a lower bias. As the bias voltage increases, excited electrons from the well level have higher tunneling probabilities, leading to a higher LWIR spectral intensity. It is to be noted that the strength of LWIR and MWIR transitions are comparable in positive bias while the LWIR transition is dominant in negative bias. DDWELL structures exhibit a bias dependent spectral response similar to DWELL devices, due to asymmetric width of quantum wells in the active region. The transition from a single well based design [36] to a DDWELL based design does not compromise the spectral diversity of the DWELL system in any manner.

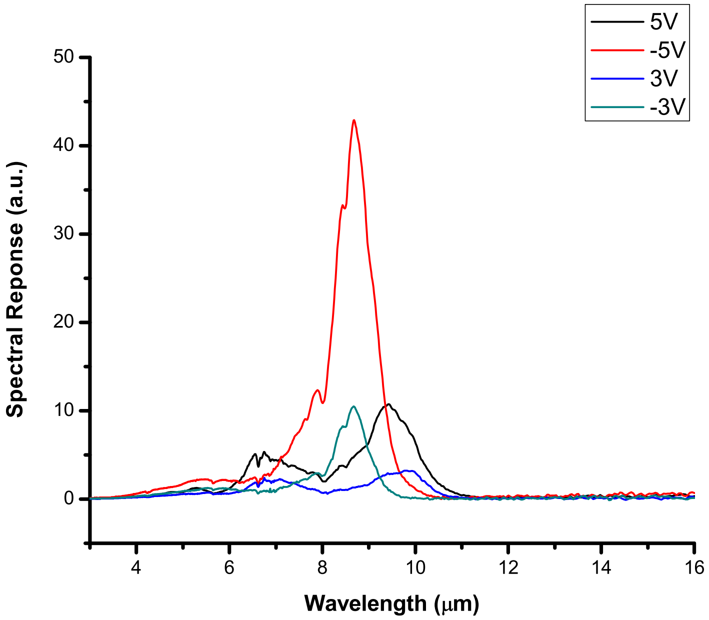

Figure 2.10: Spectral response of a fabricated DDWELL detector at 30 K.

Spectral response of these devices were measured at higher temperatures, as shown in Figure 2.11. At 77K [Figure 2.11 A)] MWIR and LWIR transitions are clearly visible, with limited noise peaks in the spectrum. The LWIR peak in negative bias region has a higher intensity when compared to other transitions. At 120 K, [Figure 2.11 B)]the increased dark currents start affecting the quality of the spectrum. The intensity of negative bias LWIR peak drops and is comparable to spectral intensities in positive bias. The spectral response was visible till a temperature of 140 K. Here, LWIR peak was present only in the negative bias, with the noise limiting presence of LWIR peak in positive bias. The range of bias voltages that can be applied to the detector is also limited at this temperature. The maximum voltage is limited to ±3 V, and dark currents start overloading the device beyond this range. The operating temperature range of DDWELL devices is higher than that

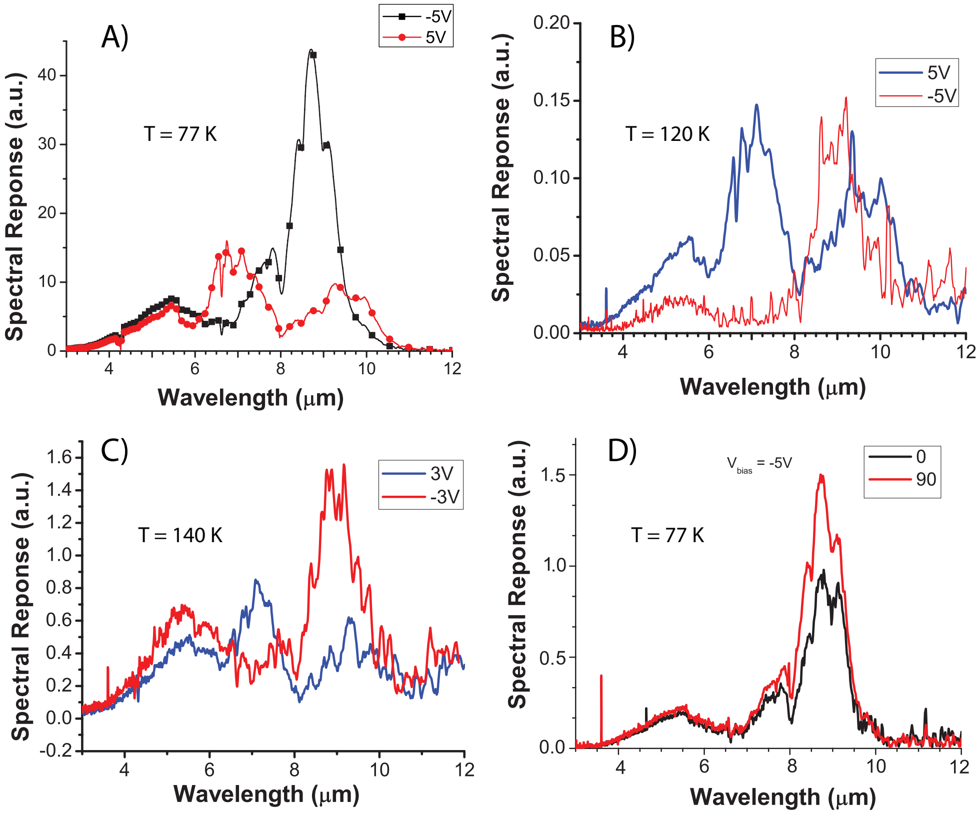

Figure 2.11: Spectral response of the DDWELL device at various temperatures with the applied bias. A): Spectral response of the DDWELL device with 65 nm barrier at 77 K. The MWIR and LWIR peaks can be observed at a positive bias while the LWIR peak is much stronger than the MWIR peak in negative bias. B), C): Spectral response at 120 K and 140 K. The range of bias voltages that can be applied is reduced as the temperature increases. A five point smoothing filter has been applied to reduce the effect of noise peaks. D) Variation of spectral response intensity with the angle of polarization of incident radiation. The devices are measured at a temperature of 77 K and a bias of -5 V.

of single well based DWELL designs, and this leads to reduced cooling requirements for detectors based on DDWELL design.

The polarization dependence of the spectral response was measured using a wire-grid polarizer. The spectral response in the positive bias regime did not show any dependence of intensity with the polarization angle. The negative bias response, however, shows a strong dependence with the angle of polarization. A plot of the spectral response at a bias voltage of -5 V is shown in Figure 2.11 D). The response at a polarization angle of 90 is approximately 70 % higher than the response at an angle of 0°. This may be due to the asymmetry of the quantum dot sizes along the two orthogonal directions. With this difference in intensity, these devices can be used for polarization sensing, which can be used in the field of target detection [64].

2.4.2 I-V Characteristics

Current-voltage characteristics of fabricated devices were measured using a HP 4145 B semiconductor parameter analyzer. The devices were mounted in cryostats, having a metallic shroud cooled to same temperature as the detector. This shroud acts as a cold shield, providing low background photon fluxes. The shroud has an opening that irradiates the detector with a f/2 field of view (FOV). Thus it is possible to measure both dark current, and total current (the sum of dark current and photocurrent) with a f/2 FOV, using the same setup (but not in the same measurement).

The dark current characteristics of DDWELL devices with 30, 50 and 65 nm barriers are plotted in Figure 2.12. The design with a 30 nm barrier shows a significantly higher dark current when compared to designs with 50 and 65 nm barriers. The 50 nm and 65 nm barrier devices have similar dark current characteristics at lower bias voltages. At higher biases, where tunneling currents start to dominate[65], the 65 nm device shows a lower dark current.

The dark currents of DDWELL devices with a 65 nm barrier were measured as a function of temperature. This is plotted in Figure 2.13 with the photocurrent density at 30 K. The dark current density of DWELL devices increase as a function of the temperature. At ≈77 K the dark current density and the photocurrent density of the devices are equal. At this temperature, the device operates as a background limited

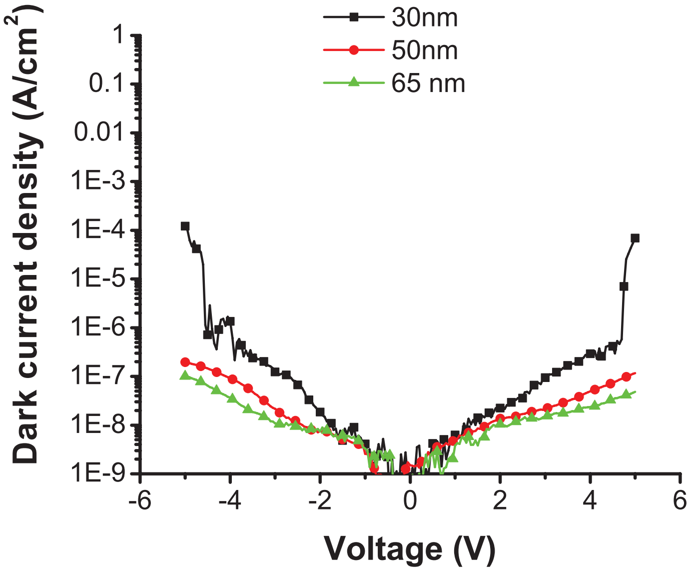

Figure 2.12: Current density of of DDWELL devices with 30, 50, and 65 nm barriers.

infrared photodetector (BLIP). In the BLIP regime, the device noise is dominated by the noise of irradiating photon stream. Further improvement in noise performance cannot be achieved in the BLIP regime by cooling devices, as noise is related to the detection mechanism. At higher temperatures, the dominant noise is from dark current, and by lowering the operating temperature device performance can be improved.

Finally, dark current densities from DWELL and DDWELL detectors are compared in Figure 2.14. Devices with DDWELL active region have significantly lower dark currents. This is reflected in high operating temperatures of DDWELL based devices. At a bias voltage of -4 V, DDWELL systems offer a dark current reduction of 10^4 over standard DWELL designs. The reduced dark current density is the primary reason for higher temperature operation of DDWELL devices, as shown in subsection 2.4.1.

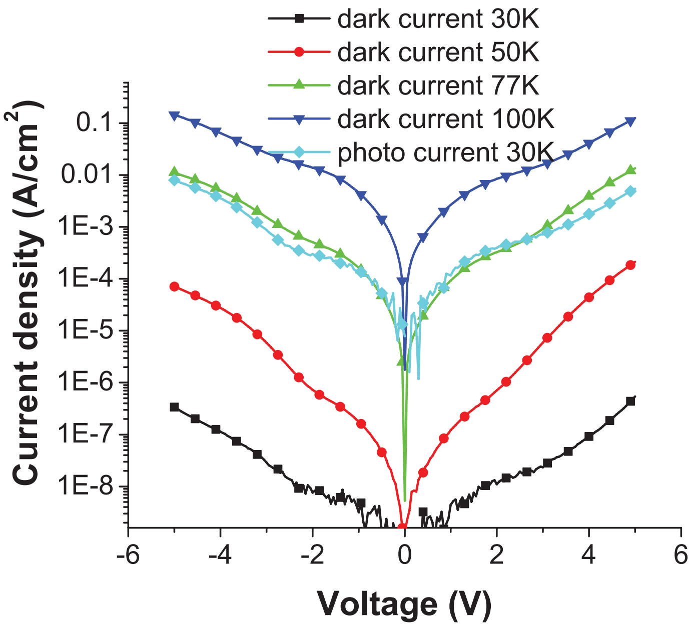

Figure 2.13: Current density DDWELL devices with 65 nm barriers at different temperatures, along with the photocurrent density at 30 K. The BLIP temperature of this device is ≈ 77 K.

2.4.3 Signal and Noise Measurements

The radiometric measurements of IR detector performance involve measurement of the amount of electrical signal and noise. Normalized metrics of responsivity (R) and detectivity (D*) are used to compare the performance of infrared detectors. Responsivity is normalized with respect to the area of the device used, while the detectivity is normalized with respect to device area and integration time of the system. Thus, detectors systems with different apertures and response times can be compared for performance using these two metrics. The signal and noise from the device, upon irradiation by a calibrated IR source, are the primary quantities measured. A detailed description of the experimental setup used to measure R and D* is available in Appendix A. Specific methods used to calibrate the setup, and account for unwanted effects like optical scattering and system noise are discussed

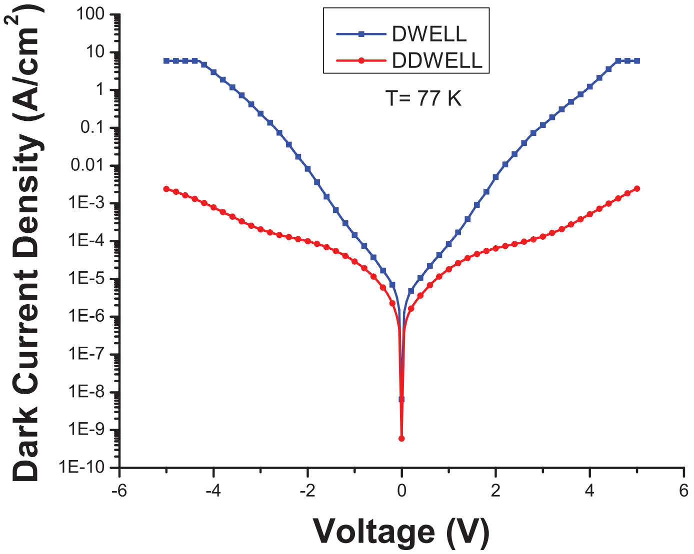

Figure 2.14: Dark current densities of DWELL vs DDWELL devices. At -4 V bias, DDWELL devices have a dark current 4 orders of magnitude lower than DWELL devices.

there.

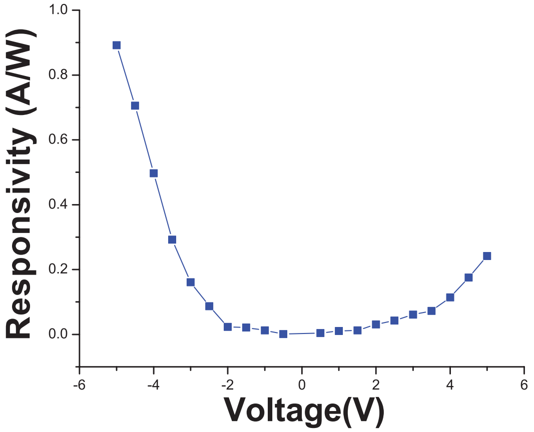

Figure 2.15: Responsivity of the device for various bias voltages at 77K.

A plot of the measured responsivity and detectivity for a DDWELL device with 65 nm barrier, as a function of the applied bias, is shown in Figure 2.15 and Figure 2.17. These devices show a peak responsivity of 0.24 A/W at a bias of 5 V for a wavelength of 9.4 μm, and 0.89 A/W at -5 V for a wavelength of 8.7 μm. This responsivity is lower than that of a device with a single $In_{0.15}Ga_{0.85}As$ well. The use of two wells leading to an increased QWIP like nature , may be the reason for a lower responsivity. The critical parameter for an infrared detector, however, would be the specific detectivity which is a normalized version of SNR. The noise power spectral density from the detector measured at 77 K is plotted in Figure 2.16. Extremely low values of noise currents, lower than 1pA/$\sqrt{Hz}$ are observed in this sample. Care was taken to make sure that the noise observed is from the detector and not due to any external source. Details of the measurement are provided in Appendix A

The peak LWIR detectivities are 1.8 $\times 10^{10}$ $cm.\sqrt{Hz}/W$ at 4 V for 9.4 μm and 6.7$\times 10^{10}$ $cm.\sqrt{Hz}/W$ at -4 V for 8.7 μm. These detectivity values are almost an order of magnitude higher than the values observed for similar DWELL designs [36, 49]. These results compare favorably to QWIPs of similar wavelength, operating at the same temperature. A peak detectivity of around 5 $\times$ 10^{10} $cm\sqrt{Hz}/W$ has been observed for a QWIP with a 8.4 μm peak wavelength at 80 K [66]. For a QWIP with 9.4 μm peak wavelength a peak detectivity of 1.8 $\times$ 10^{10} $cm\sqrt{Hz}/W$ has been observed at 70 K [67]. Table 2.1 summarizes the perforamance of DDWELL with other detector technologies with similar detection wavelengths. The DDWELL design provides an extended range of operation when compared to standard DWELLs [31]. However better ROICs are required to exploit this property in FPA, as current ROICs provide only a limited range of bias.

Higher temperature measurements of responsivity and detectivity are shown in 2.18. The devices show a peak responsivity of 0.77 A/W at a bias of -4 V for a wavelength of 8.7 μm at 140 K. A peak detectivity of 1.09 $\times$ 10^{8} $cm\sqrt{Hz}/W$ is observed at a bias voltage of -4 V for 8.7 μm at 140 K. The peak detectivity for the 9.4 μm wavelength is 7.32 $\times$ 10^{7} $cm\sqrt{Hz}/W$ for a bias of 4 V at 140 K.

FPAs of size 320 $\times$ 256 were fabricated using the DDWELL design. These FPA

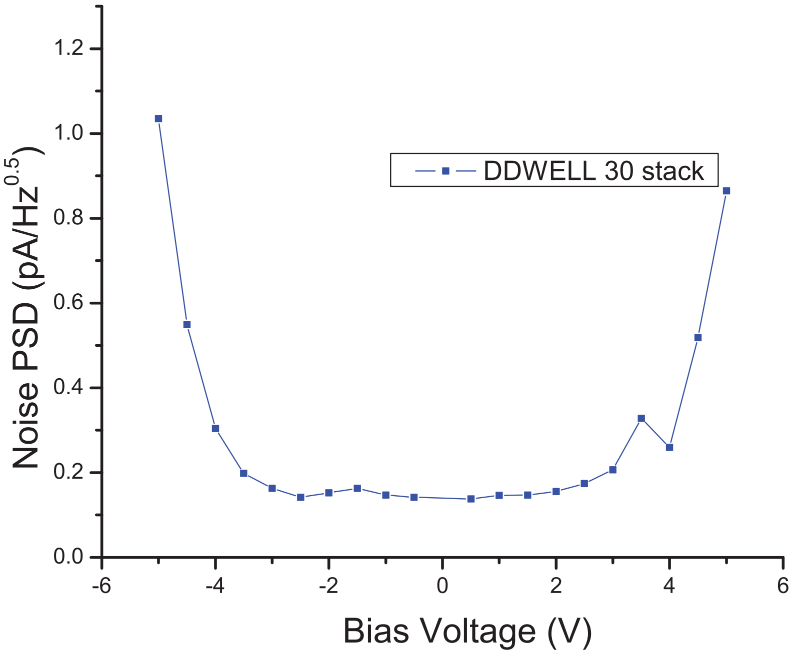

Figure 2.16: Noise PSD from a DDWELL detector at 77 K. A peak PSD of 1.04 $/pA/\sqrt{Hz}$ is observed at 5 V.

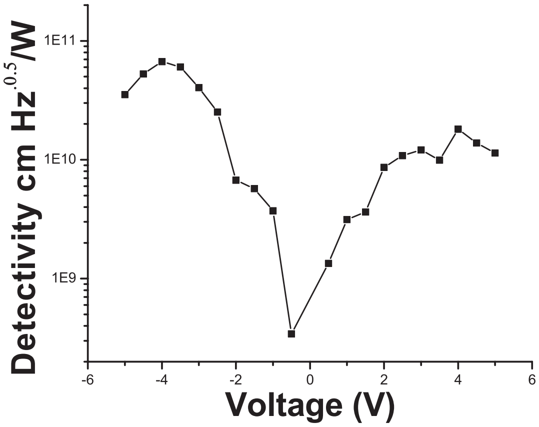

Figure 2.17: Detectivity of the device for different bias voltages at 77K. A peak detectivity of 6.7×10^{10} $cm.\sqrt{Hz}/W$ is observed at -4 V.

were fabricated in house and then sent to QmagiQ LLC for bonding to an Indigo 9705 ROIC and substrate removal. The substrate was removed through polishing

Technology (μm)	Wavelength (μm)	T(K)	D*(Jones)
QWIP[68]	8	77	7.4×10^{10}
MCT[69]	10	78	2×10^{12}
SLS[69]	10	80	4×10^{11}
DWELL[31]	8	77	2×10^{10}
DDWELL	8.7	77	6.7×10^{10}

Table 2.1: Comparison of DDWELL with other IR technologies. Note that the detectivity values of SLS are estimated values from current measurements. The D* values of DDWELL device take into account optical scattering from the substrate, while the DWELL device does not.

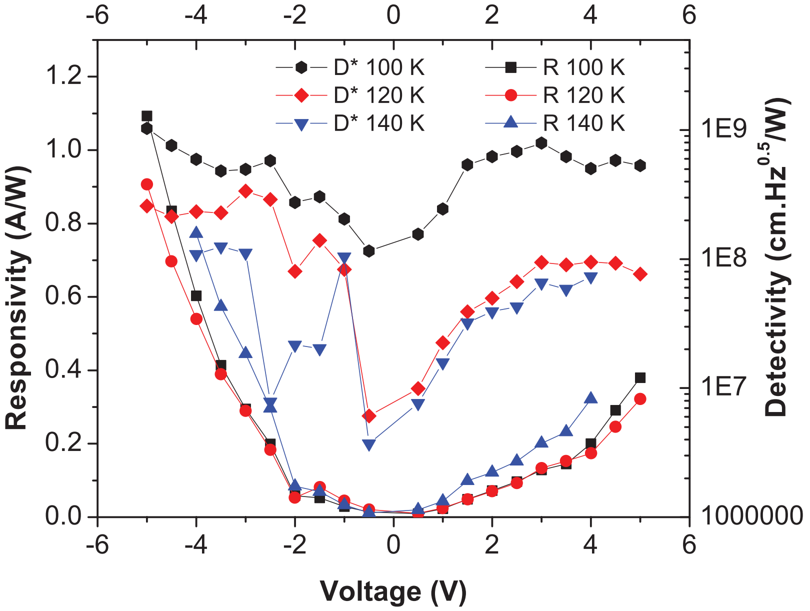

Figure 2.18: Measured responsivity and detectivity of DDWELL device with 65 nm barrier at various temperatures with the applied voltage bias.

and dry etching based on BCl_3-SF_6 mixture. Images were obtained at 80 K. This is a 20 K increase in the operating temperature from FPAs using single well DWELL designs. With improvements in processing, a higher pixel operability and improved SNR can be obtained. The Indigo 9705 ROIC limits the bias range and polarity that can be applied. MWIR and LWIR response can still be observed from DDWELL

FPAs. To selectively image different IR bands, a MWIR/LWIR lens was used for focusing. Images are obtained in both MWIR and LWIR regions of IR spectrum, and in the 3-12 μm range, as shown in Figure 2.19

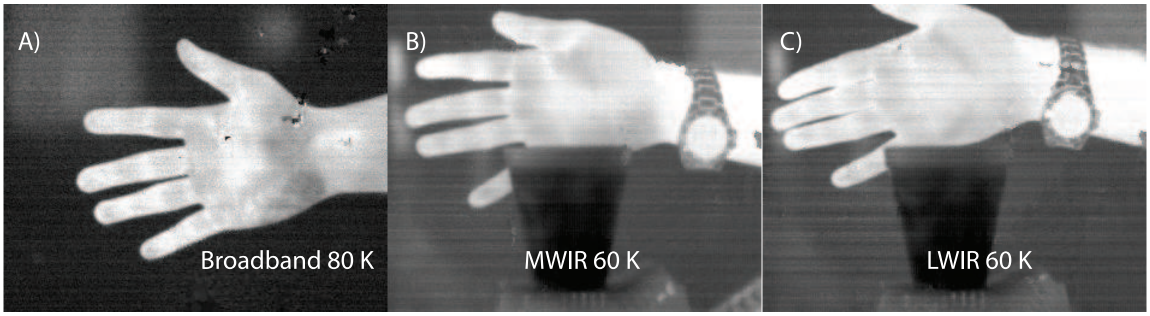

Figure 2.19: Images obtained from DDWELL FPA. A) Broadband (3-12 μm) image at 80 K. B) MWIR image at 60 K. C) LWIR image at 80 K. Image A) courtesy W. Jang

2.5 Conclusions

In this chapter, efforts to grow thicker active regions are discussed and implemented. Reduction of strain per active region stack was achieved by minimizing thickness of the strained QW region. A new design where InAs quantum dots are embedded in $In_{0.15}Ga_{0.85}As$/GaAs wells is presented. A series of optimizations were performed, using AFM and PL, to maximize QD yield. The final detector structure with InAs QDs in a double well and an $Al_{0.10}Ga_{0.90}As$ barrier was grown. Detector structures processed show a dual color spectral response and bias polarity dependent spectra. A high temperature (140 K) LWIR operation is possible for single pixel detectors. Calibrated signal and noise measurements performed indicate a high detectivity of 6.7×10^{10} $cm.\sqrt{Hz}/W$ in the LWIR regime for this device. A dark current reduction factor of 10^4 is observed when compared to standard single well DWELL designs. This value is comparable to several QWIPs which are currently employed in commercial IR systems. Focal plane arrays of size 320×256, which work at a temperature of 80 K, have been processed using these designs.

Chapter 3

Multispectral and Polarization Sensitive DWELL Infrared Detectors

3.1 Introduction

Multi-spectral detection is the ability to sense different wavebands, with a minimal amount of crosstalk. The ability to sense multiple colors provide infrared systems with an additional dimension of contrast. Features with specific spectral signatures can be imaged using different wavelengths of detection. Multi-spectral infrared detection has major applications in the field of gas detection, identification of chemical and biological compounds, remote sensing and thermography [70]. This capability is considered an integral part of third generation IR systems, along with large format arrays and higher temperature of operation [70]. Another potential use is in the detection of targets, especially in low contrast and high clutter. Current multi-spectral systems make use of an external filter with a broadband focal plane array (FPA), or disperse the light on to several arrays [71]. This approach, however increases the cost of the arrays several fold. The use of external components such as filters or beam splitters increase the size of these systems and require complex optical alignment, as array sizes increase.

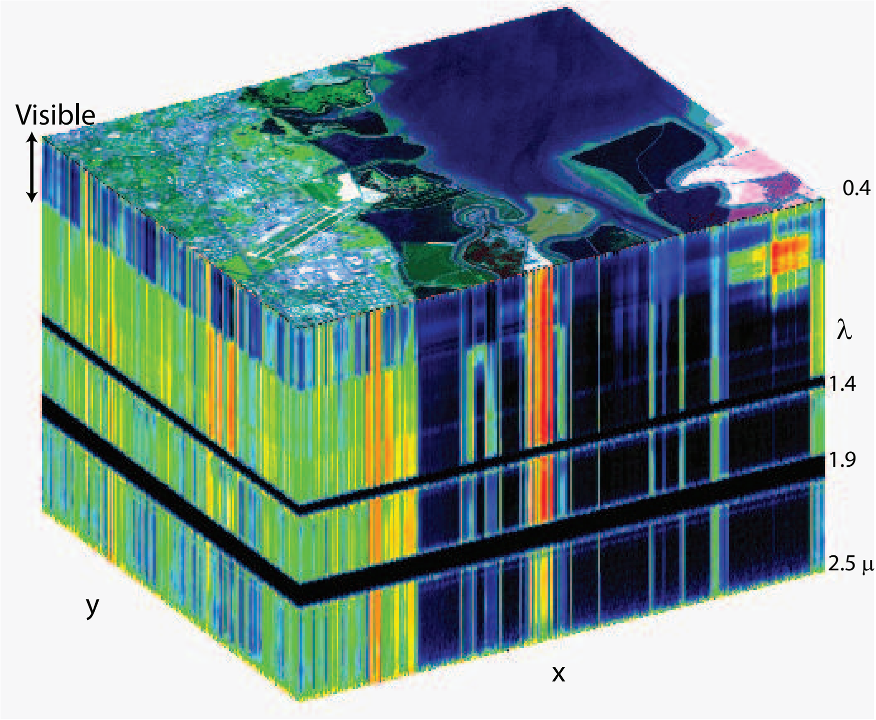

Figure 3.1: Data cube of a multi-spectral image. Different wavelengths are false colored. Image from NASA.

The state of the art infrared systems in place currently use bulk or bulk-like semiconductors as detector materials. Use of bulk InSb in the MWIR region and bulk HgCdTe in the LWIR region is most widespread. In photon rich applications, QWIPs are currently used. All bulk semiconductors exhibit a broad spectral response till the detector cut-off is reached. These devices sense the difference in intensity of a scene, rather than sensing specific wavelengths. The most common approach to have multi-spectral detection in bulk like semiconductors is the use of two back to back biased diodes, with different regions of absorption. By biasing the diodes appropriately, and by taking a difference signal, specific wavebands can be imaged [47, 48]. An example of imaging CO_2 is shown in Figure 3.2. Two SLS diodes, sensing different wavelengths are used in the same epitaxial growth. By biasing each diode, the image in the corresponding waveband is captured. A difference image generated in Figure 3.2 C), shows the presence of CO_2 very clearly. One of the two wavebands sensed includes the CO_2 absorption peak at 4.2 μm, while the second band excludes it. A difference signal between these two bands of absorption enhances the contrast for the 4.2 μm CO_2 peak. This method, however, is limited to detection of two bands. An additional contact is required for each additional band included, increasing the complexity of device processing. In addition, all diodes in this method share a common contact, creating crosstalk between different bands of sensing.

Detection of polarization information can also be very useful in IR systems. Applications of polarization imagery include remote sensing, microscopy and industrial monitoring. Of particular interest are applications in target tracking. In Figure 3.3 three images of the same scene in visible, LWIR, and polarized LWIR are shown. Two trucks, which are otherwise hidden in the visible or in LWIR unpolarized imagery, are clearly visible in polarized LWIR imagery. This strong contrast in imaging is due to polarization sensitivity of human made objects. Enhanced target detection can be achieved by imaging polarimetry, leading to extensive military applications.

Use of resonant cavities to change absorption peaks and to enhance them has been attempted in MWIR and LWIR regions. Fabry-Perot cavities, which are epitaxially grown, and microelectronic mechanical actuators (MEMS) [43, 72] are some of the techniques used to modify the detector response. Another approach is to use gratings etched on to the surface of the detector. This has resulted in improving performance of QWIPs in LWIR region. Gratings etched into the active region couple incident light to higher order modes enabling higher absorption [73, 74]. The use of dielectric

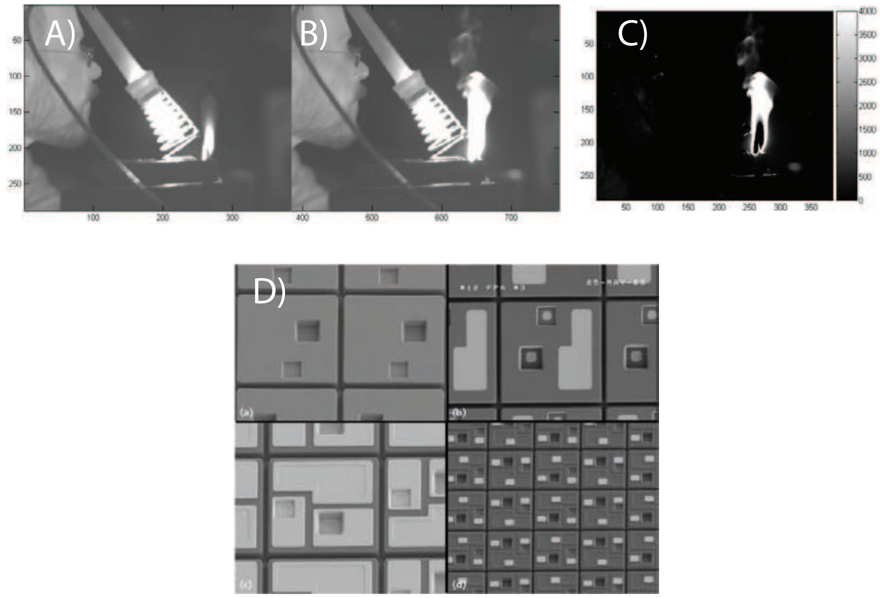

Figure 3.2: CO_2 sensing using two back to back biased diodes. The blue channel images have a cutoff of 4 μm and the red channel images a cutoff of 5 μm. The difference image shows CO_2 absorption at 4.2 μm clearly[48]. An image of the fabricated FPA with three contact pads per pixel is also shown in D).

and metallic deep etched photonic crystals have been attempted in LWIR region [44, 55]. The high aspect ratio needed in etching makes processing difficult and increases dark current in these devices.

In this chapter, a novel method to encode spectral and polarization information inside a pixel is demonstrated. The response of DWELL detectors is tuned by coupling absorption of DWELL active region to resonant modes of a subwavelength nanostructure, integrated with the top surface of the conventional detector. The coupling of a resonant system with detector makes the absorption a function of spectral

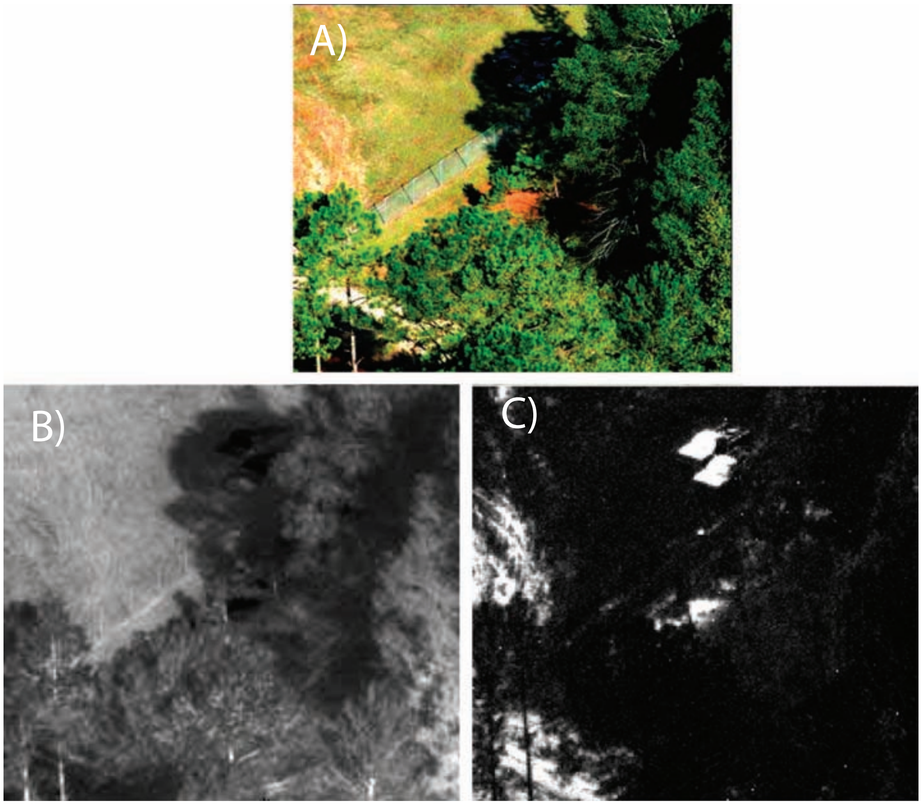

Figure 3.3: A) Visible image of a scene. B)LWIR image of the same scene. C) Polarization image of the scene showing presence of two trucks, which are not visible in the visible and LWIR images [64]

and polarization sensitivity of the pattern integrated. Peak absorption can be tuned by changing the pitch of the pattern. This allows for multi-spectral sensing without the need to have external optics, and makes multi-spectral detectors cheaper and practical. As a result of coupling enhanced the near-field intensity with intersubband transitions of DWELLs, the detector absorption is increased manyfold. This technique requires simplified processing, does not increase dark currents, is detector agnostic and can easily be transferred to a focal plane array.

3.2 Surface Plasmons

Surface plasmons (SP) are bound electromagnetic (EM) excitations propagating at an interface between a metal and a semiconductor. The origin of these surface waves is a coupling of EM fields to electron plasma of the conductor [75, 76]. These waves propagate along the metal-semiconductor interface and are evanescently confined in perpendicular directions. Renewed interest in this field was initiated through the phenomenon of extraordinary transmission through structured subwavelength apertures [77]. An enhanced transmission efficiency, which cannot be described by classical treatment of apertures [78] and strong resonant peaks in transmission were observed in subwavelength periodic holes on metals. The appearance of these resonances is attributed to excitation of surface plasmons at the metal-semiconductor interface.

The dispersion relation of a surface plasmon bound at the metal semiconductor interface is given by

$$k_{sp} = \frac{\omega}{c}\sqrt{\frac{\epsilon_m \epsilon_d}{\epsilon_m + \epsilon_d}} \tag{3.1}$$

where ω is the frequency of the incident wave, c the velocity of light and ϵ the complex dielectric function. Subscripts m and d describe metal and dielectric respectively. A plot of the dispersion is shown for the GaAs-Ag interface interface in Figure 3.4. Equation 3.1 is valid for both real and complex parts of the plasmon wavevector. The real part corresponds to propagation constant, and the imaginary part corresponds to propagation length of the plasmon before it is damped. The dispersion curve of surface plasmons lies to the right of light line separating free space and evanescent photons. The momentum of a surface plasmon is greater than momentum of a free space photon. Thus, it is not possible to directly couple into plasmons propagating at a metal semiconductor interface. Special prism coupling schemes (like the Otto or Kretschmann configurations [75]) or gratings are required to provide additional momentum required for coupling a free space photon to SP modes.

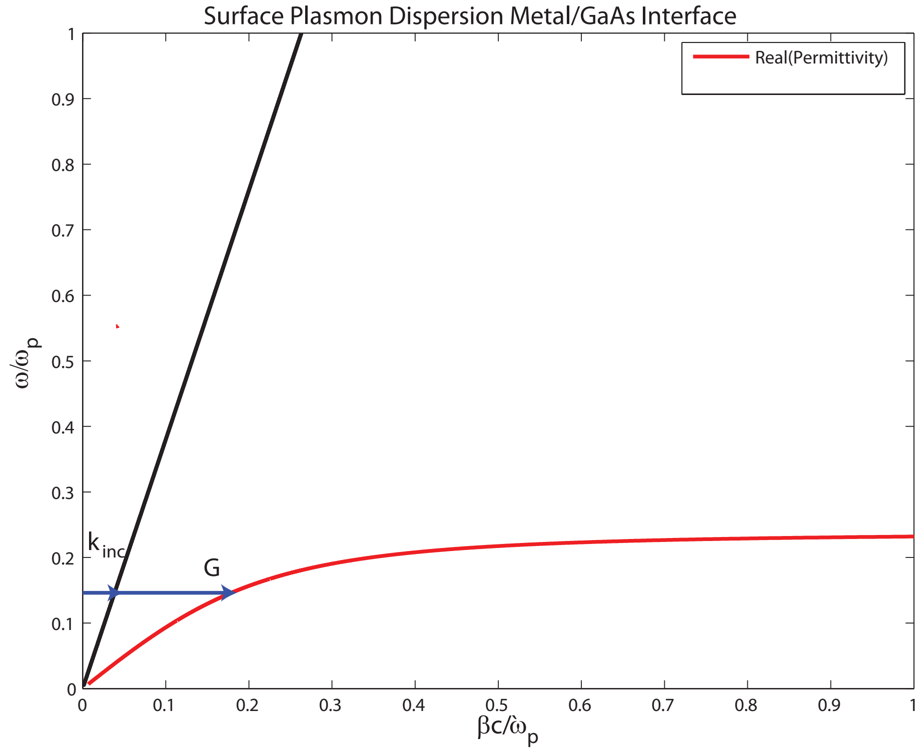

Figure 3.4: Surface plasmon dispersion relation at the GaAs-silver interface. The plasmon wavevector lies on evanescent side of the dispersion diagram.

For a wave incident at an angle θ, the relationship between the SP wavevector k_{sp}, incident wave vector k_0 and the grating vector G is given by

$$k_{sp} = k_0 \sin\theta + G \tag{3.2}$$

For a normally incident wave $\theta = 0$ and all of the momentum has to be provided by the grating. For a square lattice periodic grating used in this work, the dispersion relation can be transformed to a relation between the resonant wavelengths λ_{ij} and the grating pitch a as

$$\lambda_{ij} = \frac{a}{\sqrt{i^2 + j^2}} \sqrt{\frac{\epsilon_m \epsilon_d}{\epsilon_m + \epsilon_d}} \tag{3.3}$$

where i and j are order of plasmon excitations. The symmetric nature of the square lattice allows for two degenerate modes for each excitation order. Plots of the simulated and measured transmission spectra for a square lattice of pitch 2.9 μm are shown in Figure 3.5. Two resonant peaks, corresponding to the first and second order plasmon excitation can be observed.

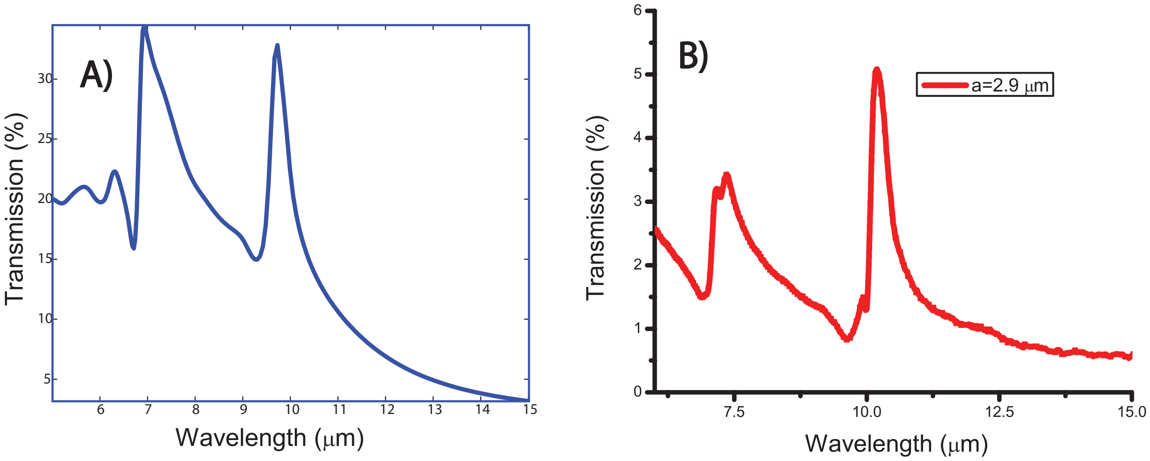

Figure 3.5: Simulated and measured transmission for a square lattice of square holes with a period of 2.9μm: A) Simulated transmission B) Measured transmission. Large area samples for transmission measurements were fabricated using interferometric lithography.

The phenomena of enhanced transmission, high near field intensity, and the ability to concentrate light beyond the diffraction limit has been used in demonstrating emitters, waveguides, antennae, lasers, and switches [79, 80]. Several researchers have discussed the potential of integrating surface plasmon nanostructures with photovoltaic and sensing applications to improve device efficiency [79, 81]. Traditionally, these devices use optically thick layers of active material, comparable to the diffusion length of carriers to maximize efficiency. The application of surface plasmons towards these systems is two fold: the first is to take advantage of the increased transmission due to plasmons and their near field focusing properties, to improve sensitivity of devices [77]. Surface plasmons are strongly confined to the metal-semiconductor interface, with an exponentially decaying field. This resonant field is coupled to an absorber placed in the near field region, leading to an enhancement. The second effect is to take advantage of resonant properties of plasmons to create photon sorters or filters. The strong affinity of resonant peaks with pitch of the fabricated pattern has been used to fabricate spectral and polarization filters [82]. A monolithic integration of the filtering aspects along with the enhanced sensitivity can be used to improve both the sensitivity and spectral selectivity of devices [83].

3.3 Design

The subwavelength nanostructure used in this work to excite surface plasmons consists of square holes in a square lattice, forming an inductive grid [84]. The use of a metallic layer has several advantages. One is the potential use as an integrated top contact, if the metal and semiconductor combination can provide an ohmic contact. The square pattern provides a fully connected region, which can be easily modified to create polarization sensitive and insensitive devices. The DWELL design offers an excellent platform to couple surface plasmons for enhancement and tuning. The single pass absorption efficiency of DWELLs is a few % [29], offering scope for a lot of improvement. The losses introduced by the absorber region are minimal and do not affect the resonant behavior of the system.

Finite difference time domain (FDTD) simulations were performed on detector structures, to understand and predict the effect of integrating a subwavelength pattern with a DWELL absorber region, using commercially available Lumerical® software. Two epitaxial designs were considered for simulations: One has a single well DWELL design consisting of 15 stacks of absorbers and the other has 30 stacks

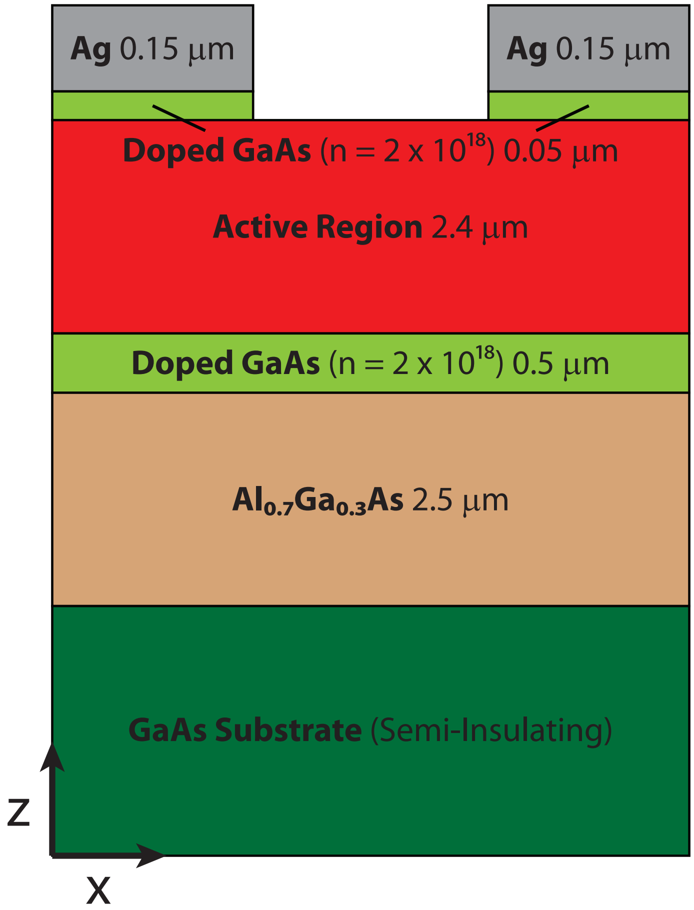

Figure 3.6: Schematic of the structure used for FDTD simulation. The absorber region has 30 stacks of DDWELL absorber, with a thickness of 2.4 μm.

of DDWELL design. A 1% normal incidence single pass absorption for 15 stack DWELL and 2% for 30 stack DDWELL designs is assumed [29]. These fmeasurements agree well with the previously reported values of absorption measured on 30 stack DWELLs with similar structures. Silver was used as the plasmonic metal, and its permittivity was calculated using the Drude model. The thickness of active regions were 0.965 μm and 2.45 μm for DWELL and DDWELL samples respectively. In order to provide a vertical confinement for the field, a thick $\mathrm{Al}_{0.70}\mathrm{Ga}_{0.30}\mathrm{As}$ layer was considered as a cladding below the bottom contact region. The metal layer at the top along with the $Al_{0.70}Ga_{0.30}As$ forms a metal-semiconductor-semiconductor (MSS) waveguide, providing vertical confinement.

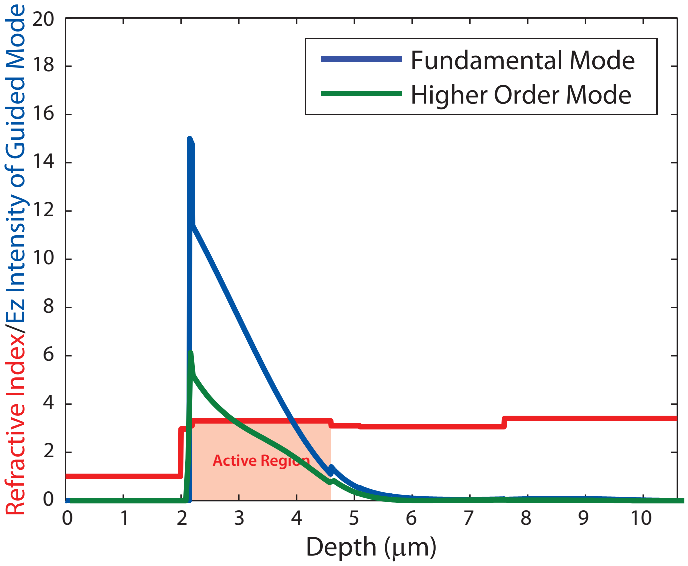

Figure 3.7: Ez field profile for the fundamental mode and a higher order mode of absorption. The confinement of fundamental mode is 91% and that of higher order mode 94%.

A schematic of one of the structures analyzed is shown in Figure 3.6. It consists of a patterned top metal layer, doped top and bottom contacts with the active region in between, and a cladding layer (optional) below the bottom contact layer The simulated structure has a lattice constant of a=2.939 μm, a hole width w to lattice constant ration $w/a = 0.567$ and a top metal thickness of 150 nm. An infinite periodic approximation was used along x and y directions, essentially simulating a large number of periods of the pattern. A perfectly matching layer (PML) was assumed along z direction. The system was illuminated with a polarized plane wave source, incident normal to the surface. The power propagating through the structure is monitored and the absorption of the detector calculated as $A_d = T(z_1) - T(z_2)$, where T is transmission, z_1 is top of the active region and z_2 is bottom of the active region.

The use of $Al_{0.70}Ga_{0.30}As$ cladding improves confinement within the active region. As shown in Figure 3.7, for a structure with a cladding layer, the E_z profile of the fundamental mode has a 91% confinement, in contrast to purely dielectric waveguides with much lower confinements. For a structure with no cladding the confinement is 56%. The ability to grow thicker absorber layers using a DDWELL design, thereby confining a greater portion of the energy within the active region, has been a great advantage here. The corresponding confinement for a single well based DWELL design is 42%, which indicates that a large portion of the energy is leaks into the cladding/substrate and does not contribute to absorption. The absorption is directly proportional to the strength of electric field and the confinement within the active region. A larger confinement within the active region can lead to a higher enhancement of absorption for these devices.

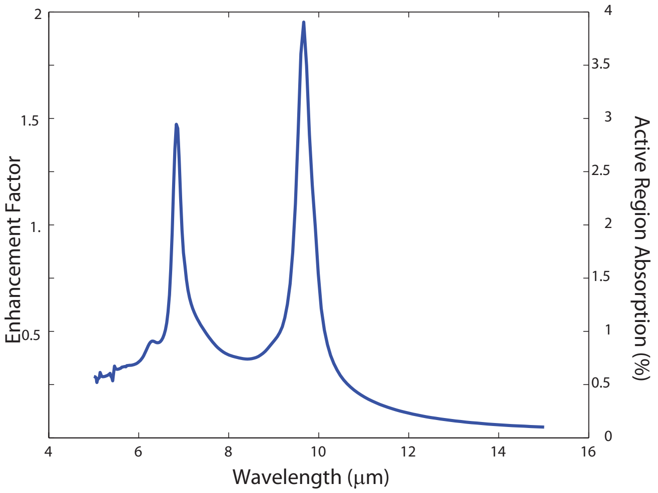

Figure 3.8: Absorption of the DDWELL detector with no cladding. The absorption is enhanced by a factor of 2. The low enhancement is as a result of a low confinement factor for mode energy within the active region.

The plots of simulated absorption are shown in Figure 3.8 and Figure 3.9 for devices without and with an $Al_{0.70}Ga_{0.30}As$ cladding layer. For a device with a cladding the peak absorption is A_d=11.5%, assuming A_{DW}=2% single pass DWELL

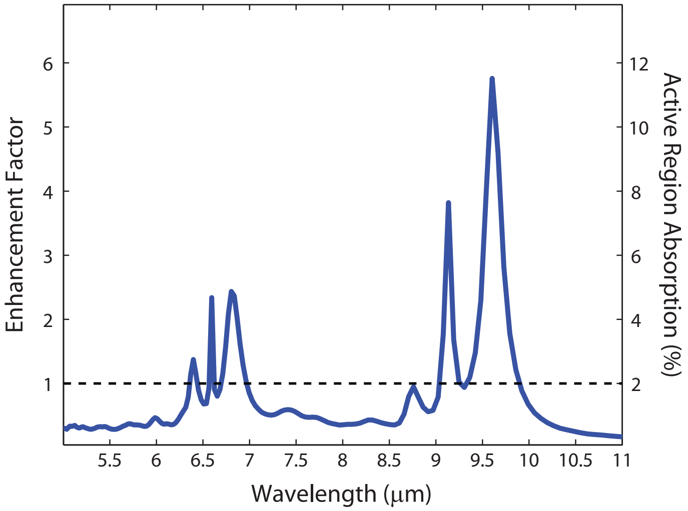

Figure 3.9: Simulated absorption of DDWELL detector an $\mathrm{Al}_{0.70}\mathrm{Ga}_{0.30}\mathrm{As}$ cladding layer below the bottom contact. A peak enhancement factor of 5.7 is predicted for the fundamental mode. A baseline is shown, indicating the single pass absorption of the DWELL region.

absorption. This corresponds to a peak enhancement factor $E = A_d/A_{DW}$ of 5.75, when compared to a device no integrated pattern. The calculation of this enhancement does not remove area covered with metal in the computation, as is done for computing enhancement in extraordinary transmission through patterned thin metallic layers [77]. For a standard DWELL epitaxial design, the enhancement factor is $\approx$2, as there is no cladding to prevent the mode energy leaking into the substrate. The absorption shows several resonant modes, which can be used to sense multiple wavelengths at the same time. The origin and nature of these modes is discussed in chapter 4. The confinement factor for higher order modes of absorption is also plotted in Figure 3.7. The higher order mode has a confinement factor of 94%, which is higher than the fundamental mode. The peak amplitude of the field, however, is lower. The absorption being a function of net energy present in the active region is therefore lower for the higher order mode.

Electric field profiles of the fundamental mode mode along different planes of

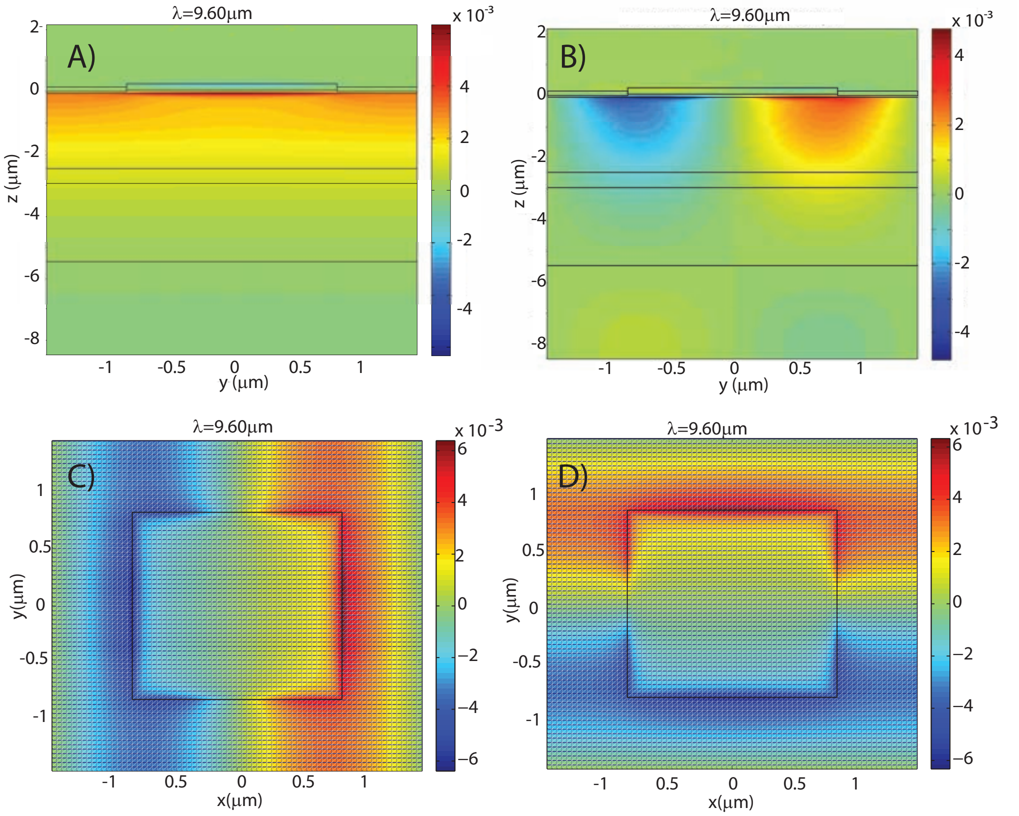

Figure 3.10: A), B)y-z field profile of the fundamental absorption feature at λ=9.6 μm.C), D) x-y field profile for the fundamental mode for two orthogonal polarizations. The modes are identical except for the 90° rotated field profile

the structure are shown Figure 3.10. Due to the symmetry of the square lattice, two degenerate modes are present for each absorption feature. The field profile of one mode is rotated 90° with respect to the other mode. The y-z field profiles of the two orthogonal modes for the highest wavelength absorption feature (λ=9.6 μm) are shown in Figure 3.10 A) and B). The x-y field field profiles at the metal semiconductor interface for the two modes are shown in Figure 3.10 C) and D). The field is concentrated near hole edges in x-y direction and has a evanescent decay in z direction.

The presence of two degenerate modes with identical absorption characteristics,

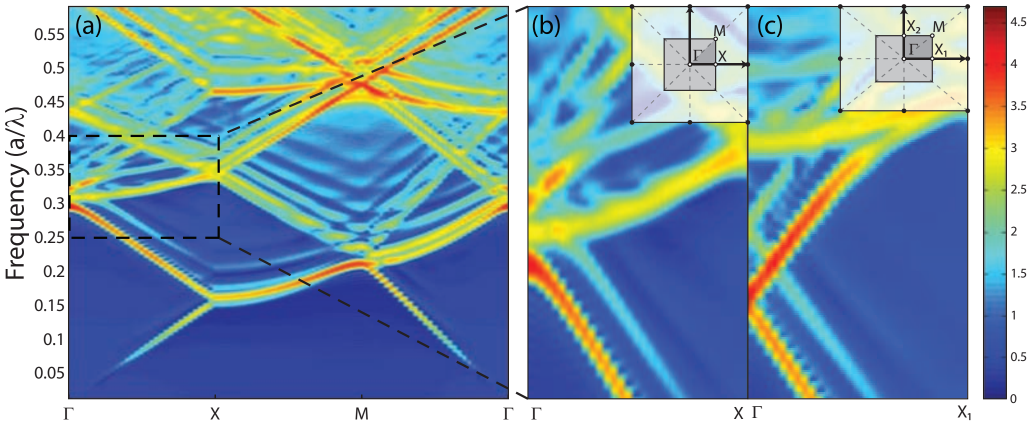

Figure 3.11: (A)Bandstructure of the square lattice: (B) Band profile near the Γ point. Degenerate flatband modes can be observed. (C) Bandstructure of stretched and compressed lattice at the Γ point. The modes of (B) are split in frequency as a result of the broken symmetry [58]

.

but different polarization features can be exploited to design polarization sensitive detectors. If the symmetry of the square structure is broken, the modes are no longer degenerate and are separated in wavelength. Simulated TM bandstructures of the square lattice are shown in Figure 3.11 [58]. There is no bandgap in this structure. Instead, two orthogonal flatband modes are present at the Γ point, to which free space waves easily couple. Low group velocity of these modes confines it in the active region, enabling higher absorption. The symmetry of the square lattice allows presence of two orthogonal modes, one polarized in the x direction and other in the y direction. In a perfect square lattice, these modes are degenerate. The bandstructure for a system, where the lattice is stretched by 10% in one direction and compressed by 10% in the orthogonal direction is shown in Figure 3.11 C). The two orthogonal modes split in frequency as a result of lattice asymmetry. These modes would be strongly polarization dependent, and detection of these modes can provide a scheme for encoding polarization in pixels.

3.4 Fabrication

Detector structures were processed using standard techniques of mesa etching, passivation and contact metal deposition as described in Appendix B. Fabricated pixels consisted of top-illuminated 410 μm x 410 μm square mesas, with aperture diameters ranging between 25 and 300μm. A thin layer of SiN_x was deposited as a passivation layer, followed by a contact metal and a thin plasmonic metal (Ti/Ag) evaporation by e-beam deposition. Ti acts as an adhesion layer and Ag is the plasmonic layer. The plasmon metal covers entire aperture of the detector, eliminating detector response to IR light. Care was taken to cover all excess area on the device by metal, to reduce substrate scattering. Reduction of optical scattering is of paramount importance in these devices, as each detector has a different spectral response from its neighbor. Any scattering or crosstalk between pixels or collection through exposed areas in the mesa, can lead to light being coupled to the absorber without involving the surface pattern. This will manifest as incompletely suppressed absorption features from control sample in the output spectrum.

Following this, three sets of samples were fabricated using e-beam lithography and Ar based dry etching: Sample A with 15 stacks of DWELL active region, sample B and sample C with 30 stacks of DDWELL absorber. Sample A and B have periodic square holes in a square lattice pattern, while sample C had lattice constants stretched in one direction and compressed in the orthogonal direction. Two control samples without plasmon metal were also prepared, control1 for sample A and control2 for samples B and C, as they have the same active region, to compare the effect of integrating subwavelength patterns with the detector. The patterned samples and the control sample were part of the same growth and were processed together till the plasmon metal step, to eliminate variations in growth and processing. A top view of the fabricated detector is shown in Figure 3.12 A) and an SEM image of the fabricated lattice is shown in Figure 3.12 B). A cross sectional SEM of a fabricated

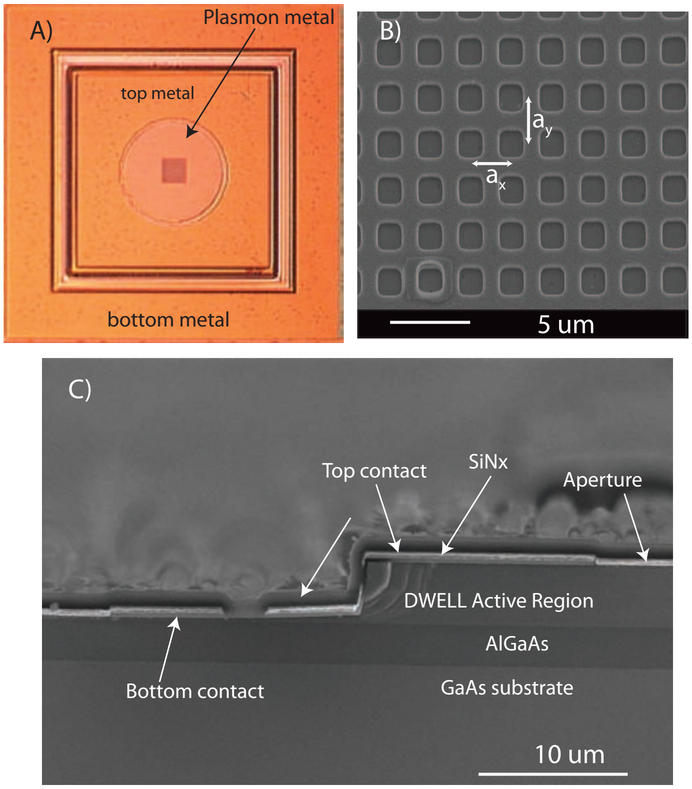

Figure 3.12: Images of fabricated plasmonic DWELL/DDWELL detector. A) Optical image of the fabricated detector. Mesa, top metal, bottom metal and plasmonic metal can be observed. The square region at the center shows the fabricated pattern. B) Scanning electron microscopy (SEM) image of etched pattern inside the detector aperture. The pattern is a rectangular lattice with square holes, formed from a square lattice by stretching lattice constants in one direction and compressing it in the orthogonal direction. C) Cross-sectional SEM images of a fabricated detector. The top metal flows around the edges of the mesa, preventing light leakage through the edges. SiNx is used as a passivant.

device is shown in Figure 3.12 C).

3.5 Characterization

To characterize detectors, spectral response, signal, noise and dark current of the devices were measured. Spectral measurements were done at various bias voltages using a Nicolet 6700 FTIR. Spectral response of sample A for a bias of -4.2 V is shown in Figure 3.13 and of sample B at a bias of 5 V in Figure 3.15, along with control samples at the same bias. The spectral response of patterned devices show the presence of resonant phenomena, showing a peak absorption for the detector at the peak of the resonant cavity. The spectra of sample A show a marked difference from the spectrum of the control sample. The spectra show two modes with peak wavelengths of the fundamental mode varying from 8.5 to 9 μm and 6.1 to 6.6 μm for the higher order mode, while the control sample shows a response with a peak at 10.3 μm. Full width half maxima (FWHM) of the spectrum is 900 nm, indicating a Q factor of 10. The additional peak observed in Figure 3.13 c) may be due to peel-off of plasmon metal layer, coupling light to active region through the exposed areas. In positive bias, the control sample shows a broad response from 7-11 μm. Spectral response from the patterned devices plotted in Figure 3.14, have a single peak in LWIR region. The response is narrower and the peak wavelength scales linearly as pitch of the pattern. The excitation of higher order modes is lower in positive bias, when compared to negative bias.

For sample B, by varying the lattice constant from 1.82 μm to 2.45 μm, peak of the detector response has been tuned from 5.5 to 7.2 μm. The LWIR peak of 9.1 μm present in the control sample is suppressed and the lower wavelength peaks corresponding to resonance have been enhanced. A higher order mode is also visible at lower wavelengths, as predicted by the simulations. The observed spectral features show good agreement in wavelength with predicted features from Figure 3.9. For different bias voltages, the plasmon integrated devices show a behavior similar to unpatterned devices. The peak intensity in MWIR and LWIR regions increase with

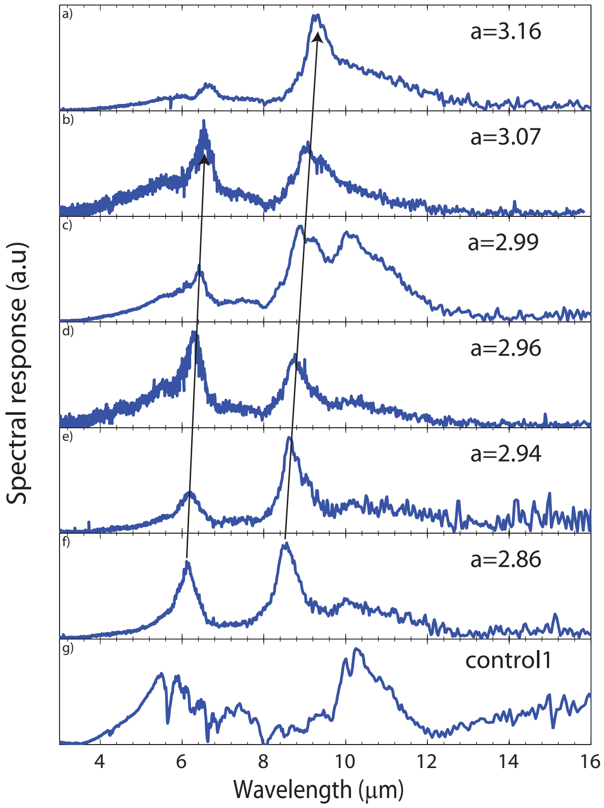

Figure 3.13: Spectral response from sample A (DWELL material, square lattice) obtained at 30 K, -4.2 V bias. Two modes of the resonant cavity, whose peak wavelengths increase with the lattice constant can be seen.

the applied bias voltage, while the wavelength of the resonant peak is invariant, as shown in Figure 3.16.

Spectral response from devices in sample C, which has a rectangular lattice (due to stretching and compression of the square lattice), is shown in Figure 3.17 A) and B). Device A) has a lattice constant of 2.1 μm in the x direction and 2.6 μm in the y direction while device B) has lattice constants of 1.8 μm and 2.1 μm in x and y directions respectively. The detector response for unpolarized light and light

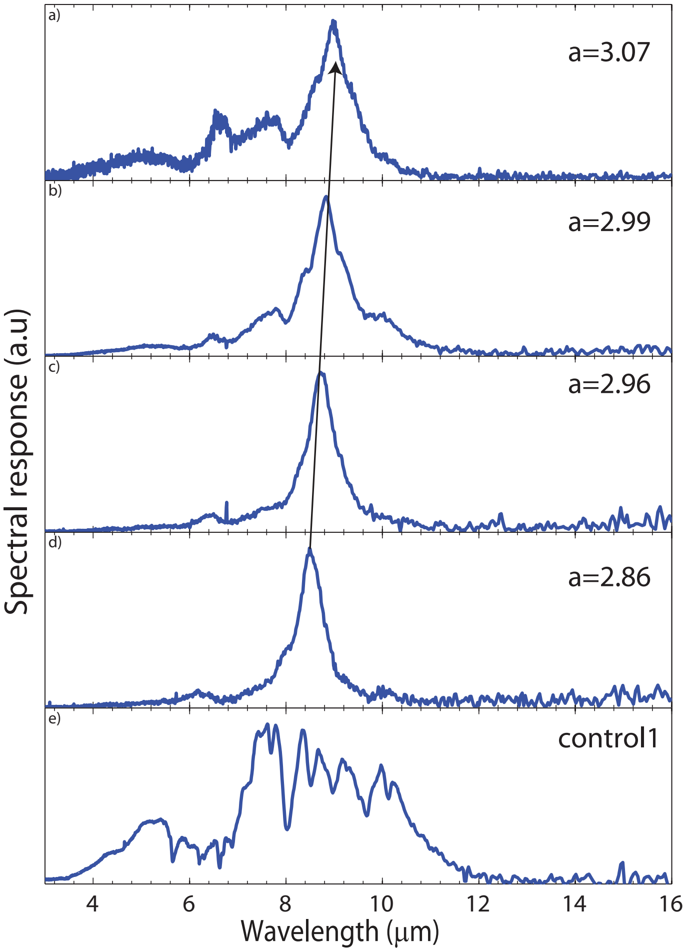

Figure 3.14: Spectral response from sample A at 4 V bias. A single mode is observed in absorption.

polarized in orthogonal directions was measured using a wiregrid polarizer. Splitting of degenerate modes and their stronger response to light polarized in one direction can be observed. The mode in Figure 3.17 A) at 8 μm is 90° polarized while the mode at 6.6 μm is strongly polarized with light at 0° and has an intensity 2.26 times that of 90° polarized light. In 3.17 B) the mode at 6.6 μm is 90° polarized while the one at 5.5 μm is 0° polarized.

The resonant spectra of these devices can be measured at higher temperatures

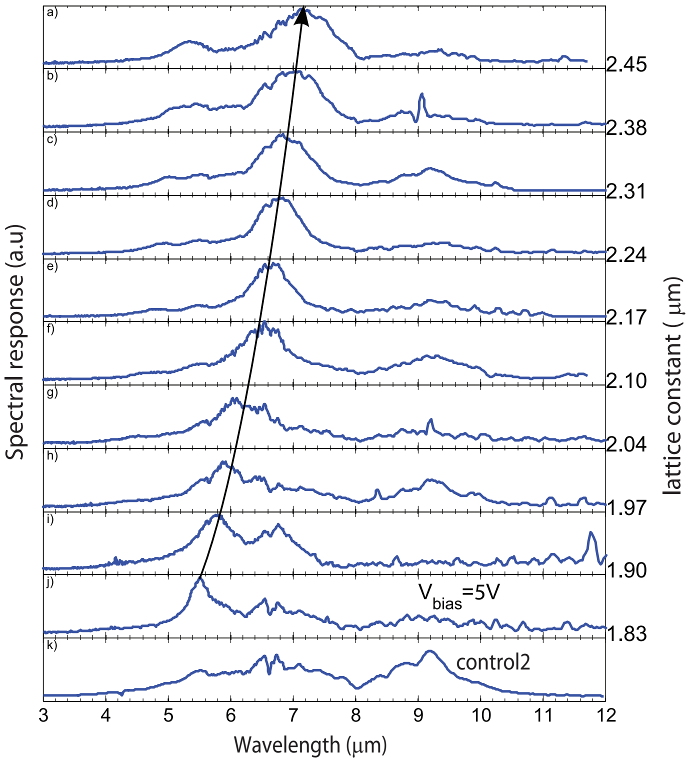

Figure 3.15: Normalized spectral response from sample B, measured at at 30 K indicating tuning of peak wavelength with the lattice constant. The devices were biased at a voltage of 5 V, except for plot i) which was biased at 3 V. Peak wavelength variation from 5.5 μm to 7.2 μm is achieved by changing the lattice constant from 1.82 μm to 2.45 μm. A two point smoothing filter has been applied on the spectra.

without observing a significant degradation in SNR. A representative device from sample B, with a pitch of 2.17 μm is shown in Figure 3.18. The spectrum has a peak at 6.7 μm. The LWIR peaks from the control sample are suppressed, as they are off resonance.

The signal and noise of devices at 77 K was measured by irradiating with a blackbody at 800 K. From these measurements, the peak responsivity and detectivity are extracted, as explained in Appendix A. These are plotted as a function of the applied bias in Figure 3.19 A), for a representative device. The peak detectivity

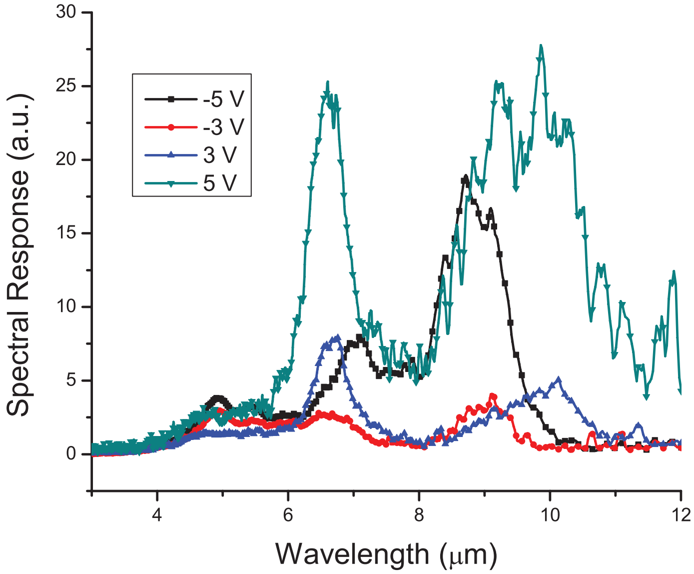

Figure 3.16: Bias dependent spectra from sample B at 30 K. The peak intensity of MWIR and LWIR tranisitions increase with the bias voltage.

observed for this sample is 3.1 × 10^9 cm·$\sqrt{Hz}$/W at 4 V bias, for a wavelength of 6.7 μm. The peak wavelengths of the patterned and control samples are different and hence for a fair comparison, their responsivity needs to be compared at the same wavelength. The enhancement factor is defined as

$$E = \frac{R(\lambda_i)}{R_{control}(\lambda_i)} \tag{3.4}$$

where $R(\lambda_i)$ is responsivity of patterned detector at the resonant wavelength and $R_{control}(\lambda_i)$ is responsivity of control sample at the same wavelength. The plasmonic detectors show an enhancement in detectivity and responsivity, when compared to the control sample. The observed enhancement factors for various wavelengths from samples B and sample C are shown in Figure 3.19 B). The observed enhancement factors vary between 1.5 to 5.5, with peak enhancement observed at 7.2 μm. This plot represents a conservative estimate of the enhancement factor, as substrate scattering is not eliminated completely in control samples. Enhancements in responsivity and detectivity of samples are not identical, due to variations in noise between patterned

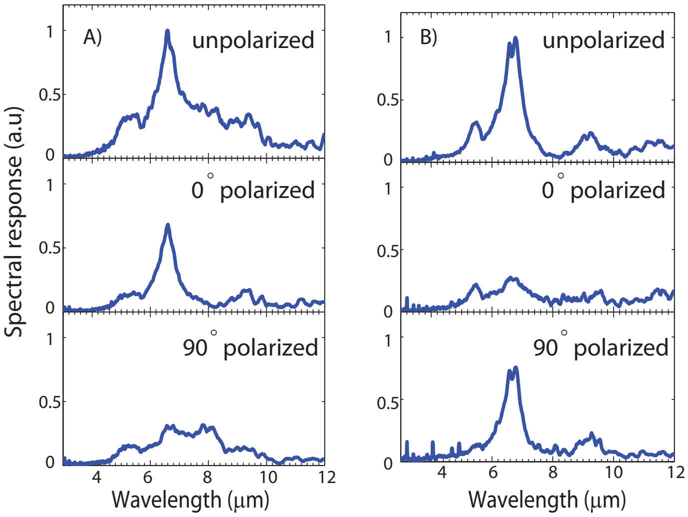

Figure 3.17: Polarization dependent spectral response from devices in sample C (DDWELL material, stretched lattice), at 5 V, 30 K. Response to unpolarized light, light polarized at 0° and 90°. Polarization sensitive modes at different wavelengths, due to different lattice constants in orthogonal directions can be observed. Sample A is stretched in the x direction, while sample B is stretched in the y direction. The resonant mode is dominated by 0° polarized light in A) and by 90° polarized light in B).

sample and control sample. The difference in factors across various wavelengths may be attributed to variations in DWELL absorption and processing of the cavity. This enhancement is seen at wavelengths where the DWELL absorption peak is not prominent. The device performance can be further improved by aligning resonant wavelengths of surface patterns with peak absorption of DWELL layers.

I-V measurements of control sample and patterned devices were performed, to examine the effect of patterning on dark currents. The average dark current density of control samples and dark current densities from patterned devices are plotted in Figure 3.20. The dark current of control sample falls within the statistical distribution of dark currents in patterned samples, which indicates that the patterning process has minimal a contribution to dark current of the detector. The variations in dark current density may be due to pixel to pixel variations in processing and

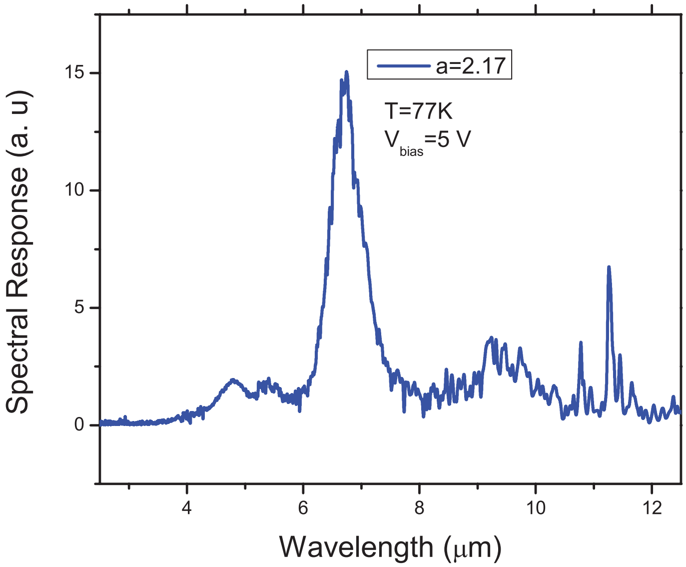

Figure 3.18: Spectral response measured at higher temperatures. Resonant spectra from a device with a=2.17 μm at 77 K and 5 V bias.

may not be due to the patterning process itself. This method of integrating cavities minimizes damage to devices, as the patterning is confined to the surface and does not etch the active region.

3.6 Conclusion

Integration of subwavelength metal nanostructures with DWELL detectors is discussed here. FDTD simulations predict absorption of the integrated structure to be a function of both DWELL detector absorption and the resonant modes of integrated patterns. An absorption enhancement is predicted for the detector. The peak wavelengths are dependent on pitch of the pattern integrated. A fully connected square pattern allows seamless switching between polarization dependent and independent sensing. By stretching and compressing lattice constant along orthogonal directions, devices can be made polarization sensitive. Fabricated detectors show several reso-

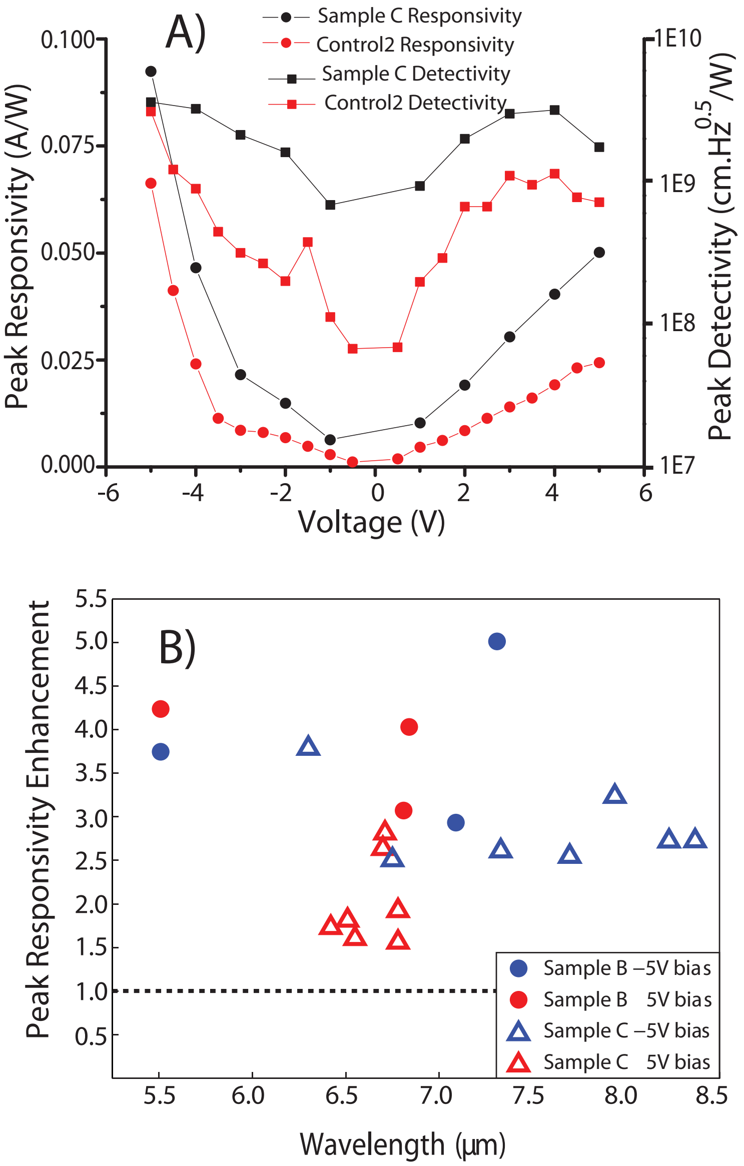

Figure 3.19: Measured responsivity and detectivity of plasmonic detectors. (A) Responsivity and detectivity of a device from sample C at 77 K, with that of control sample. The peak wavelength of control sample at positive and negative bias voltages is 9.4 μm and 8.7 μm respectively. The device from sample C has a peak wavelength of 6.7 μm. (B) Measured enhancement factors of detectors across various samples, for a bias voltage of -5 and 5 V at 77 K. A peak enhancement is observed at 7.2 μm.

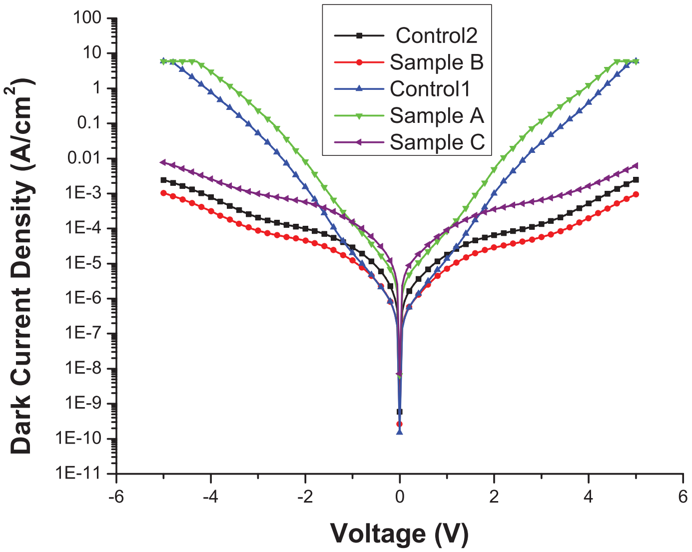

Figure 3.20: Dark current measurements at 77 K for patterned and control samples. The average dark current density for control1, control2 and representative detectors from samples A, B and C are shown.

nant features, whose peaks scale with pitch of the subwavelength structure. Spectral tuning is observed in MWIR and LWIR regions. A peak enhancement factor of 4.9 is observed at 7.2 μm. Devices integrated with rectangular lattices show a 3× polarization sensitivity. Dark current measurements indicate no statistically significant increase in dark current from patterned samples.

Chapter 4

Origin of Resonant Peaks in Plasmonic DWELL Detectors

4.1 Introduction

The use of corrugated metal surfaces or structured metallic films to enhance and improve the efficiency of devices has been a matter of intense study in the recent past[78, 79, 85–87].. Several of these structures use a surface pattern for a 2D confinement (in x and y directions) and a vertical waveguide for z confinement. The use of a metal - semiconductor - metal (MSM) , or metal - semiconductor - air (MSA) or metal-semiconductor-semiconductor (MSS) structures, which confine the electric field to the active region have been explored [56, 58, 88]. The presence of low index cladding layer(s) in these structures result in the presence of propagating waveguide modes in these structures, along with plasmon modes [88–90]. Both of these modes have been predicted to aid enhancement of response from absorbers. A clear understanding of the excitation of these modes and their interactions is necessary to understand the origin of the enhancement and to optimize performance. In this chapter, the origin of resonant peaks observed in DWELL detectors with integrated subwavelength patterns is discussed. By tailoring the coupling geometry and by manipulating the absorber thickness, selective excitation of plasmon modes, waveguide modes and a combination of the two is demonstrated. Attempts are made to understand the origin of these modes, through identifying their spectral and spatial characteristics.

4.2 Analysis of Resonant Features

In order to understand various resonant features, the absorption plot of a plasmon assisted DDWELL detector with an $Al_{0.70}Ga_{0.30}As$ cladding (sample B in chapter 3) is reproduced in Figure 4.1 A). Six modes of absorption can be observed in this sample, while a similar system with no $Al_{0.70}Ga_{0.30}As$ cladding has two modes of absorption. The presence of an $Al_{0.70}Ga_{0.30}As$ cladding, leading to the formation of a MSS waveguide, can excite propagating waveguide modes within the structure. Waveguide modes in thin film structures have been predicted to enhance the performance of solar cells integrated with corrugated metal patterns [88]. In order to understand and analyze the contribution of each type of mode towards the enhancements described in chapter 3, it is necessary to separate out these modes in wavelength. A common approach would be to scale the pitch of the pattern used to couple from free space to the modes of the system. Detector structures were simulated at a pitch of 2.38 μm to determine the effect of changing the pattern on the resonant peaks of observed modes. The peaks of all features in absorption, however, scale almost identically, making it difficult to separate out various modes, within the limits of experimental resolution. Thus, selective excitation one type of mode over the other is necessary for identifying enhancement mechanisms in plasmon assisted DWELL devices.

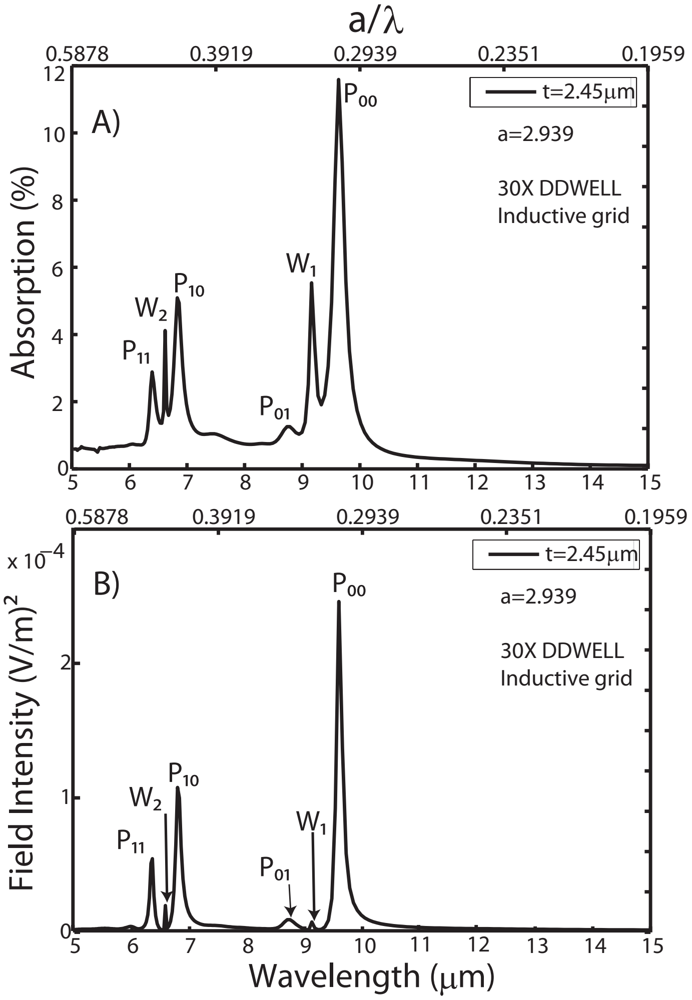

Figure 4.1: A) Absorption from a DDWELL sample integrated with an inductive grid. Six modes of absorption are observed. B) Surface electric field intensity of the same structure as a function of wavelength. Plasmonic modes show a high surface field intensity, while waveguide modes have a weaker intensity at the interface.

The excitation of surface plasmons in a structure is strongly geometry dependent. Minhas et al. have studied the transmission characteristics of inductive (a set of periodic holes in metal) and capacitive (periodic metallic posts) grids in detail [84]. The excitation intensity of surface plasmon waves is dramatically different in these two pattern types. A connected surface, like a set of holes in a lattice, has strong plasmon excitation features. Indeed, the fundamental mode and several higher order modes are visible in the transmission spectra of a set of holes in metal. This is one of the most common patterns used for coupling of plasmons with emitters or absorbers [60, 77, 82, 91]. In contrast, the capacitive grid consists of individual conduction points and does not have a connected conducting channel. This results in fairly weak excitation of plasmons at the metal-semiconductor interface. In a transmission geometry, these structures exhibit a minimum at the first order plasmon mode with a broad transmission region in the higher order modes, see Figure 4.2 [84]. This is quite different from the transmission spectrum of inductive grids exhibiting strong transmission peaks. The wide transmission region of a capacitive grid is also indicative of the increased damping losses of surface plasmons in this structure.

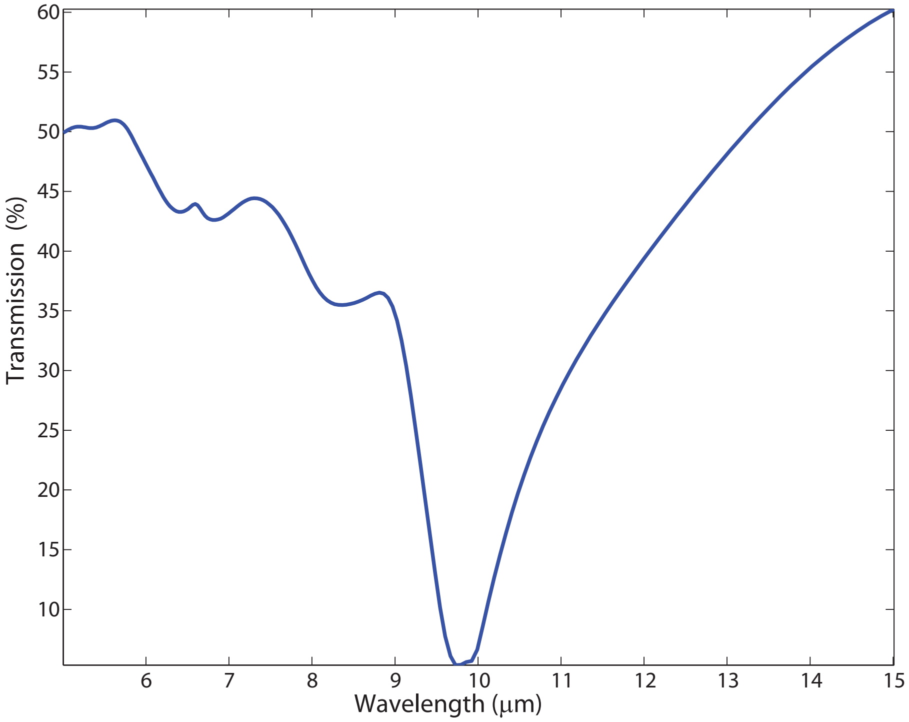

Figure 4.2: Transmission spectrum of an inductive grid. A broad region of high transmission is observed.

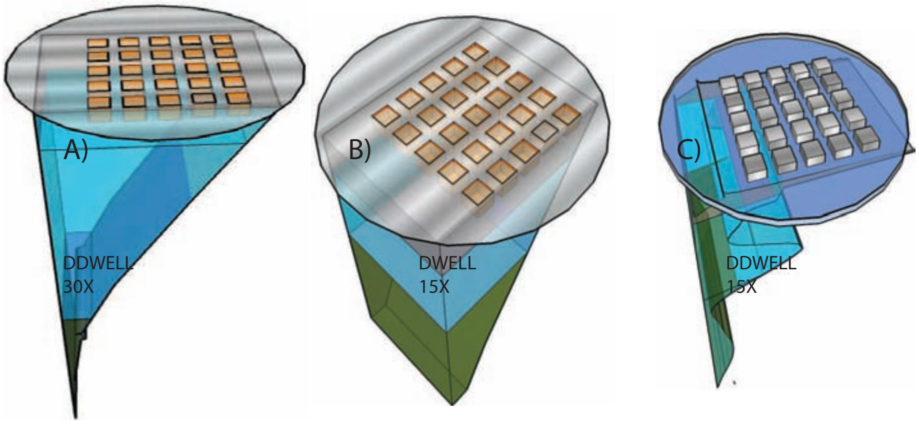

Figure 4.3: A) Inductive grid sample with 30 stack DDWELL B) Inductive grid sample with 15 stack DWELL. C) Capacitive grid sample with 30 stack DDWELL. The useful field contributing to intersubband absorption is shown in blue and the field leaking to contacts/cladding is shown in green.

The strong contrast exhibited by inductive and capacitive grids in coupling plasmons can be exploited for selective excitement of plasmon and waveguide modes. Use of an inductive grid as a surface pattern leads to strong excitation of plasmon modes. In MSS structures, the waveguide modes are also excited, if they are supported. Surface plasmons, being excited at the metal-semiconductor interface, exhibit a very high field intensity there. The waveguide modes, however, are confined to the waveguide formed by the metal-absorber-cladding region and to the substrate. These modes are expected to exhibit a higher intensity inside the waveguide than at the metal-semiconductor interface. This localization of energy from different types of modes in the system can be used to distinguish between them. In planar systems, waveguide modes have a sinusoidal distribution, and have a high field intensity farther away from the waveguide boundary. A thin DWELL absorber placed in the evanescent field region would primarily couple with plasmon modes having an exponential field distribution with the semiconductor region. Capacitive grids, on the other hand, would have a very weak excitation of plasmon modes. The excitation of waveguide modes has a weaker dependence on the nature of the coupling pattern. A capacitive grid, therefore, would primarily excite waveguide modes in a MSS system.

Three detector structures are analyzed to determine the enhancement mechanisms, by combining two coupling patterns and two absorber regions. The thicker absorber used consisted of 30 stacks of DDWELL absorber and the thinner design had 15 stacks of DWELL material. These were combined with inductive and capacitive grids to form three device structures. The first sample had an inductive grid as the coupling pattern and a thick absorber (sample A); the second sample with an inductive grid and a thin absorber (sample B); and finally a capacitive grid and a thick absorber (sample A). An illustration of the three patterns fabricated is given in Figure 4.3 A)-C) along with electric field distribution within the semiconductor.

The absorption features in the sample with thick absorber and inductive grid are shown in Figure 4.1 A). In order to classify absorption features into plasmon and waveguide ones, the surface electric field intensity at metal-semiconductor interface is plotted in Figure 4.1 B). All the absorption peaks corresponding to plasmon modes show a large field intensity at the metal-semiconductor interface. In order to understand the contribution of waveguide modes to absorption, consider the relative intensities between the modes in Figure 4.1 A) and surface field intensities in the same sample in Figure 4.1 B). Figure 4.1 A) shows that the absorption enhancements of the fundamental plasmon mode, the fundamental waveguide mode and the higher order waveguide mode are 5.5×, 2.78× and 2.07× respectively. The surface field intensity of the waveguide modes present in Figure 4.1 B), however, is lower than the intensity of the fundamental plasmon mode by a factor of 33× for the fundamental waveguide mode, and by 13.6× for the higher order waveguide mode. Strong absorption features are observed, however, from these modes in Figure 4.1 A), despite their low field intensity at the metal-semiconductor interface. This points us to the conclusion that surface phenomena have a relatively low contribution towards the origin of these features. The plasmon modes are marked P_{mn} in Figure 4.1, where

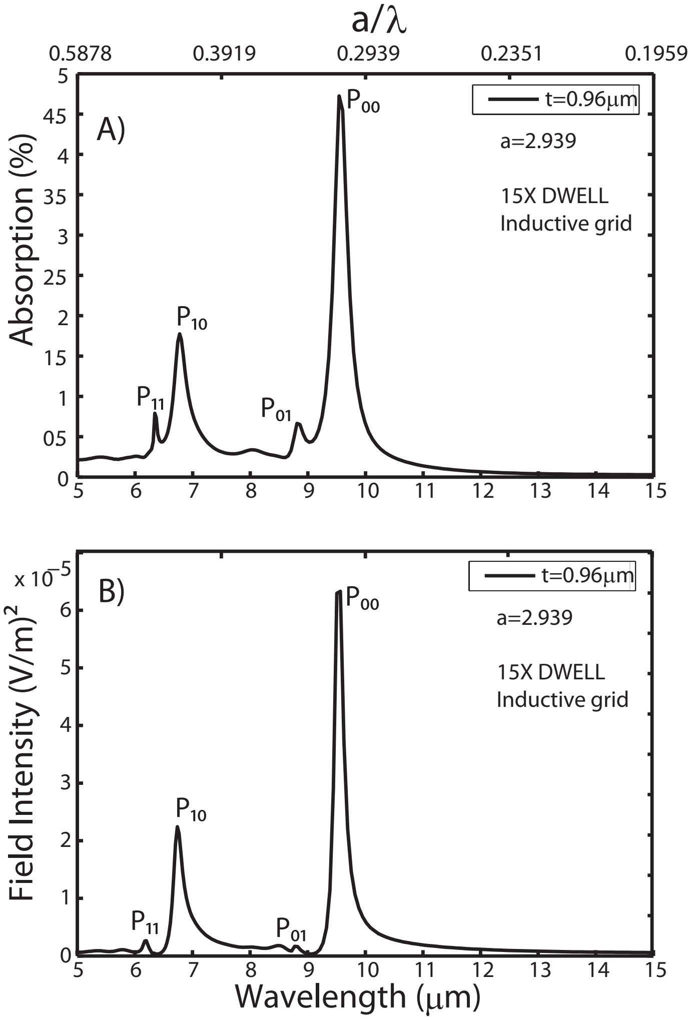

Figure 4.4: A) Simulated absorption plots B) Electric field intensity at the metal-semiconductor interface as a function of wavelength.

m is the order of plasmon excitation and n is the order in z direction (defined as the growth direction). The waveguide modes are indicated as W$_q$, where q is the order of the mode. Thus P$_{00}$ is the fundamental plasmon mode, while P$_{10}$ is the first order plasmon excitation and a zeroth order in the z direction. W$_1$ and W$_2$ are the first and second order TM waveguide modes of the structure. The fundamental plasmon mode can be observed at 9.6 μm and the fundamental waveguide mode at 9.1 μm, with higher order modes at lower wavelengths.

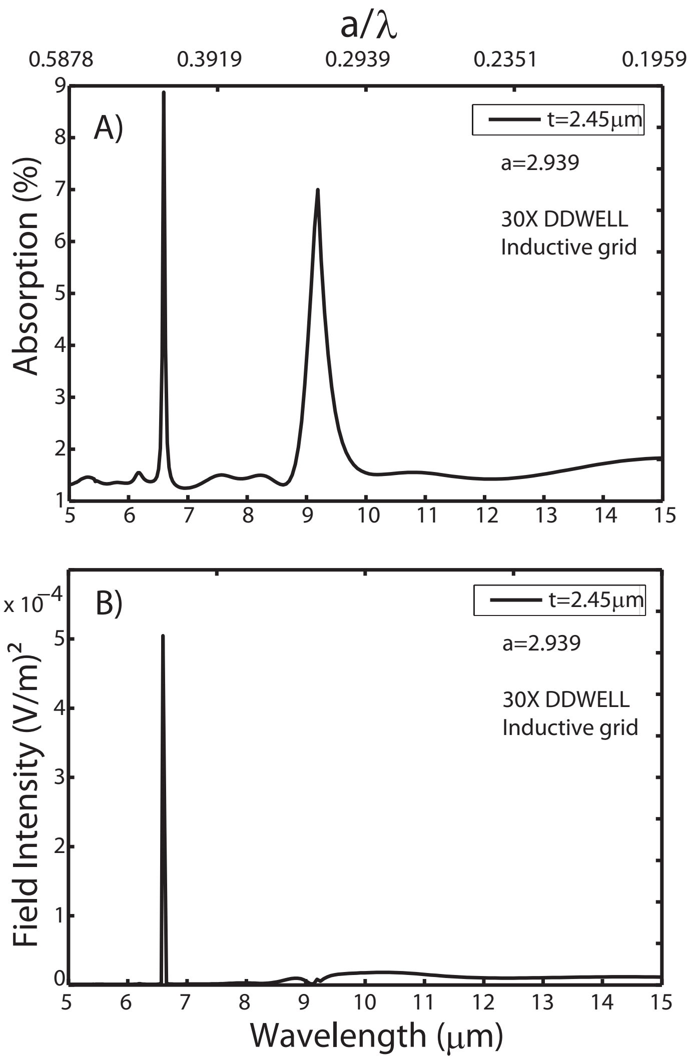

Figure 4.5: A) Excitation of WG modes in absorption. Two modes are observed B) Electric field intensity at the metal-semiconductor interface as a function of wavelength.

For a device structure with a thinner absorber and an inductive grid as the coupling pattern, four modes of absorption are observed in Figure 4.4. The surface electric field intensity as a function of wavelength in Figure 4.4 shows features matched in wavelength and intensity to features of absorption. A strong correlation is observed between surface field intensity and the peaks in absorption, indicating that field excited at the metal-semiconductor interface is responsible for absorption. Thus all the four modes of absorption correspond to plasmon modes. The thinner absorber has a higher degree of spatial overlap with evanescent fields from plasmon modes, than with field distribution from waveguide modes. This is illustrated in Figure 4.3. The high intensity regions of waveguide modes are not within the DWELL absorber and the lower spatial overlap reduces their intensity in absorption. A strategic placement of an absorber within a MSS structure can be used to couple energy from a plasmon mode or a waveguide mode, depending on the application.

For the sample with a thicker absorber and an inductive grid, use of a capacitive grid as the surface pattern limits the excitation of surface plasmons at the metal-semiconductor interface. As a result of the weak coupling, a significantly lower absorption is expected in this sample from plasmonic effects. The dependence of waveguide modes on the connected nature of the surface pattern is lower, except for the purpose of coupling from free space to the waveguide. The absorption plot of this structure in Figure 4.5 shows two features of absorption, matched in wavelength to the features in Figure 4.1 A) from waveguide modes. The absorption from plasmon modes is absent in this design. In Figure 4.1 B), the field intensity at the metal-semiconductor interface for sample C is plotted. It is noted that at the interface, W_1 has a relatively low intensity, while W_2 shows a high intensity. The surface field intensity is a necessary, but not sufficient criteria for mode classification. It is necessary to observe the spatial extent of the field intensity to ascertain the nature of the mode. As illustrated in 4.3 C), the coupling from free space to the metal-semiconductor structure can lead to a high intensity at the interface for even waveguide modes. This intensity, however, does not extend into the absorber region and subsequently does not contribute to absorption.

To examine spatial distribution of electric field, a plot of the E_Z field profile

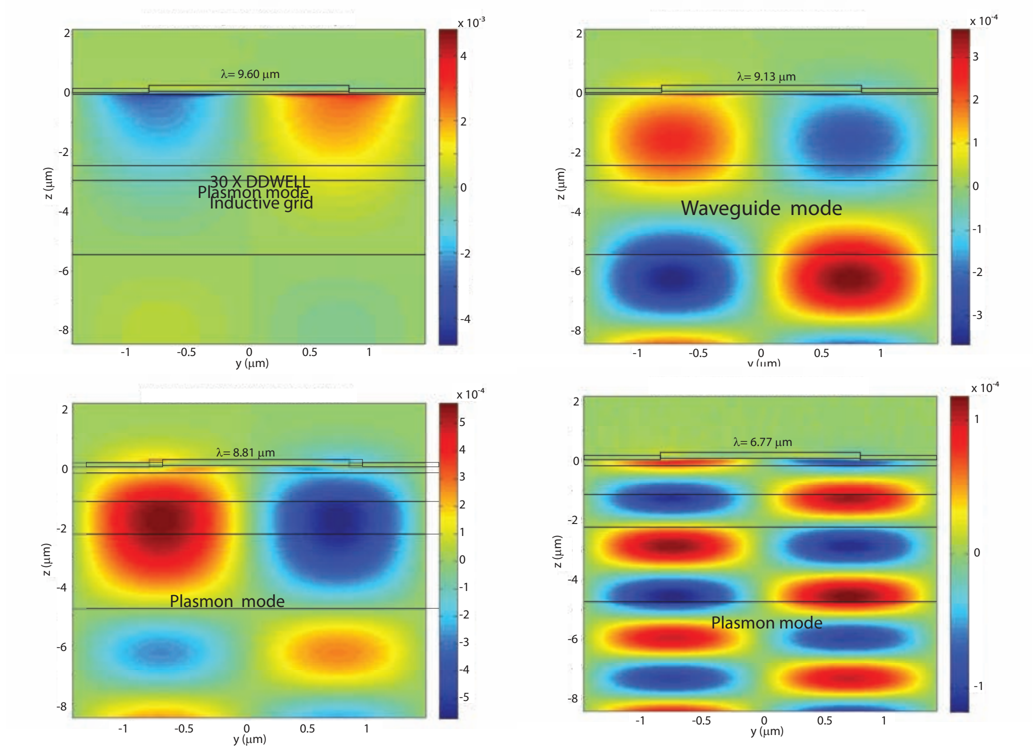

Figure 4.6: A) Mode profile of the fundamental plasmon mode P_{00} at 9.6 μm. B) Fundamental waveguide mode W_1 field profile. C), D) Field profile of P_{10} and P_{01} modes. Lines are drawn to indicate contact regions, waveguide and active regions. The detector structure used is similar to Figure 3.6

of modes in samples A, B, and C in the y-z plane is shown in Figure 4.6. The cross-section is taken at the x-edge of the hole or post as the case may be. The fundamental plasmon mode of sample A at 9.6 μm is depicted in Figure 4.6 A). This mode shows a high intensity at the metal-semiconductor interface, followed by an exponential decay into the active region. As a result of the exponential decay and a thick absorber, a very high confinement factor of 91% is obtained for this mode. The fundamental waveguide mode at 9.1 μm, shown in Figure 4.6 B), has its energy concentrated in the waveguide. There is a significant spatial overlap between the energy of the mode and the contact/substrate regions. This does not contribute to absorption. The P_{00} mode of sample B has a similar profile as the fundamental mode of sample A. This mode, however, has a lower confinement with the active region, as a result of the thinner absorber. The evanescent field tails into the bottom contact. The confinement factor for this mode is 42%, and hence a lower absorption of 4.9% is obtained for this mode. The effect of spatial distribution of the higher order plasmon mode at 6.77 μm (from sample B) is similar to that of waveguide modes. The mode profile is characterized by several regions of enhanced intensity as shown in Figure 4.6 D). Thus, the energy of this mode is not heavily concentrated in the active region, and a lower absorption is seen at this wavelength. For the capacitive grid in sample C, the maximum intensity occurs at the metal-semiconductor interface. This peak intensity, however, does not extend into the active region and the spatial mode decay rate is significantly higher than that of plasmon modes in 4.6 A) and D). The coupling from free space to the waveguide may be responsible for this high intensity. The absorption mostly occurs due to a lower field intensity distributed in the absorbing region.

4.3 Fabrication and Experimental Characterization

Square mesa structures were fabricated by dry etching, passivation and contact metalization. Once the individual detectors were fabricated, a control die was isolated for each sample for comparative characterization. For fabricating an inductive grid, the device aperture was covered with plasmon metal. E-beam lithography and dry etching are then used to transfer the pattern from resist to the metal. The dry etch process, involving physical removal of material from the aperture, introduces rough edges that acting as scattering centers. For a capacitive grid, the pattern was etched in e-beam resist, followed by a metalization (through e-beam evaporation) and lift-off, to transfer patterns. An inverse process is necessitated for the inductive grid, as exposing a positive resist is easier in an electron beam lithography process. SEM images of the fabricated structures are shown in Figure 4.7.

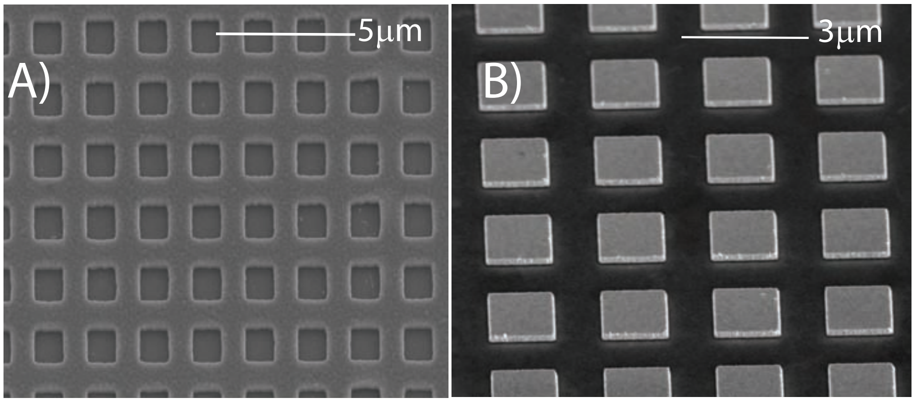

Figure 4.7: A) SEM image of an inductive grid consisting of periodic holes in metal. B) Fabricated capacitive grid of metallic posts.

In 4.6 A) and B), the plasmon mode and waveguide modes have a strong spatial overlap between them. The full width at half maximum (FWHM) of these modes is essentially determined by the losses encountered at the metal, absorber and the cladding. Additional losses are encountered by the finite in-plane extent of the pattern, metal roughness and optical scattering in a fabricated device. Further broadening of features is produced by the illumination optics. A non-zero angular dependence of illumination leads to splitting of modes for plasmons, as the resonance condition for excitation is dependent on the angle of incidence [92]. These losses lead to further broadening of the spectral features. A broad spectrum for either the waveguide or plasmon mode can lead to a coupling between these two modes, in which a surface plasmon mode resident primarily at the metal-semiconductor interface, couples light into the waveguide modes [88]. Currently, our model does not account for this coupling that may be present between these modes.

Spectral response measurements from samples A, B and C were measured using a

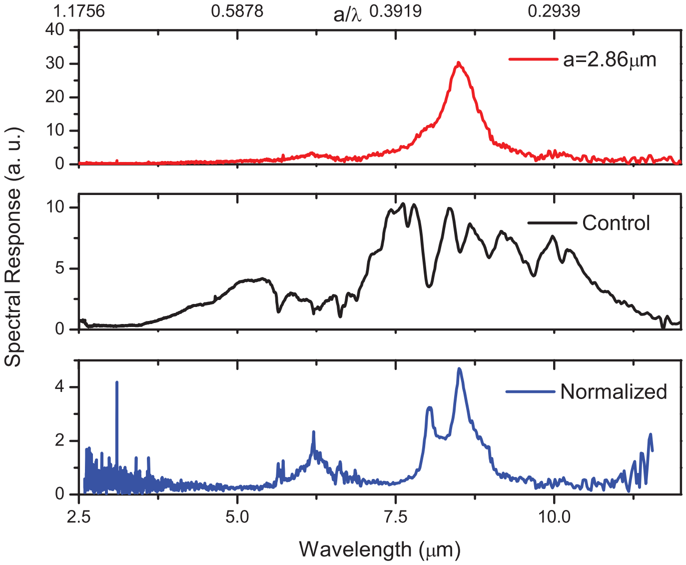

Figure 4.8: A)Measured spectrum from a detector integrated with inductive grid B) Spectral response from a control sample with no grid. C) Normalized plot of absorption showing excited modes.

FTIR at 30 K. The devices were biased to provide maximum spectral diversity in the response. The measured spectra were normalized with the control sample spectrum of that particular die, to observe the modes of absorption present. A representative device from sample B is shown in Figure 4.8, along with the control sample spectrum. Two modes of absorption are clearly visible in the detector response, while a third mode is observed as a small kink in the spectral response. Upon normalization all the three modes excited in the system can be clearly distinguished.

Table 4.1 summarizes the theoretically modeled and experimentally obtained values of a/λ for each of the samples A, B and C. The measured values of a/λ are within 10% of the theoretically modeled values. For sample A, the measured spectrum shows two peaks, one at λ = 5.5 μm and a lower wavelength peak at λ = 3.9 μm, see Figure 4.9. The spectral features observed in sample A have a quality factor Q $\approx$ 10. With this value of Q, the finer features of absorption cannot be

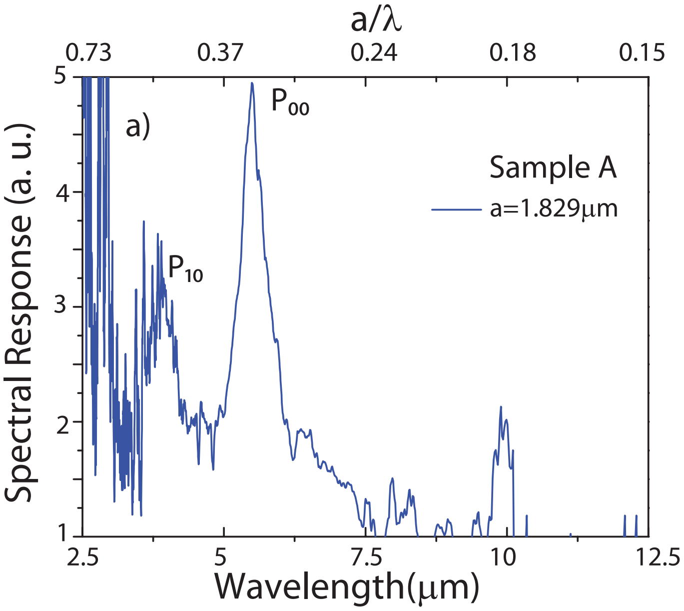

Figure 4.9: Excited modes in a DDWELL detector integrated with inductive grid (sample A). P_{00} and P_{10} modes are observed. Measurements performed at 30 K.

separated. The absorption is dominated by the fundamental plasmon mode P_{00} and the higher order mode P_{10}, forming the two strongest absorption features in 4.9 . The response is noisy at shorter wavelength edges partly due to the lower absorption of the DWELL active region. A response enhancement of 4.9 × has been measured for these samples.

For sample B, the response at 30 K shows three spectral features with the modes P_{00}, P_{10} and P_{01} in Figure 4.10. A thinner absorber, leading to a lower spatial overlap between the plasmon and waveguide mode, may be the reason for improved resolution in the spectrum from sample B. This is especially important in the design of filters and multi-spectral detectors using plasmon based devices, where a reduced crosstalk between bands is critical for the functionality. The effect of plasmon and waveguide modes on the spectral shape and width would be a topic of future research. The spectra obtained from sample C is shown in Figure 4.11. The fundamental

Table 4.1: Theoretically modeled and experimentally obtained values of a/λ for different modes in samples A, B and C. In sample A both plasmon and waveguide modes can be excited, while sample B can excite only the plasmon modes and sample C the waveguide modes. External loss factors and coupling limit the resolution of features in the measured spectra.

Mode	Theory	Sample A	Sample B	Sample C
P_{00}	0.306	0.333	0.337	–
P_{01}	0.336	–	0.366	–
P_{10}	0.428	0.471	0.462	–
P_{11}	0.462	–	–	–
W_1	0.322	–	–	0.327
W_2	0.446	–	–	–

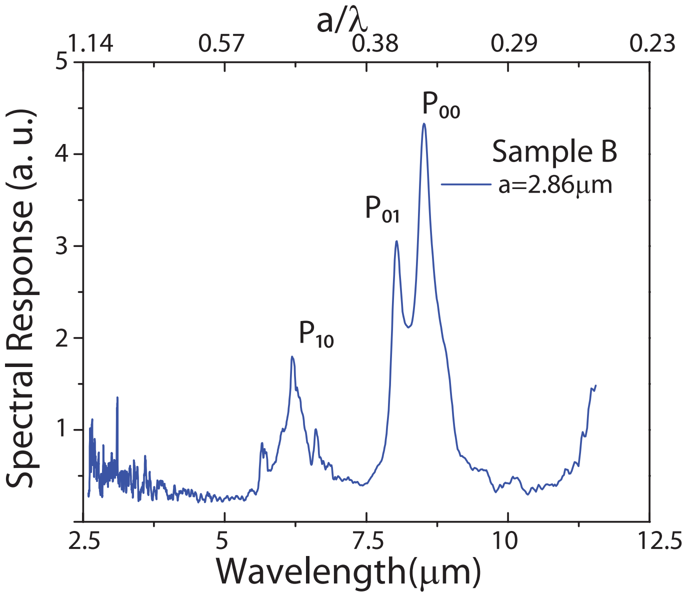

Figure 4.10: Excited modes in a DWELL detector integrated with inductive grid. Three modes of absorption are observed.

waveguide mode W_1 is visible here at a wavelength of 5.81μm. As the capacitive grid limits excitation of plasmon modes, the spectral features originate entirely from to the excitation of waveguide modes within the sample.

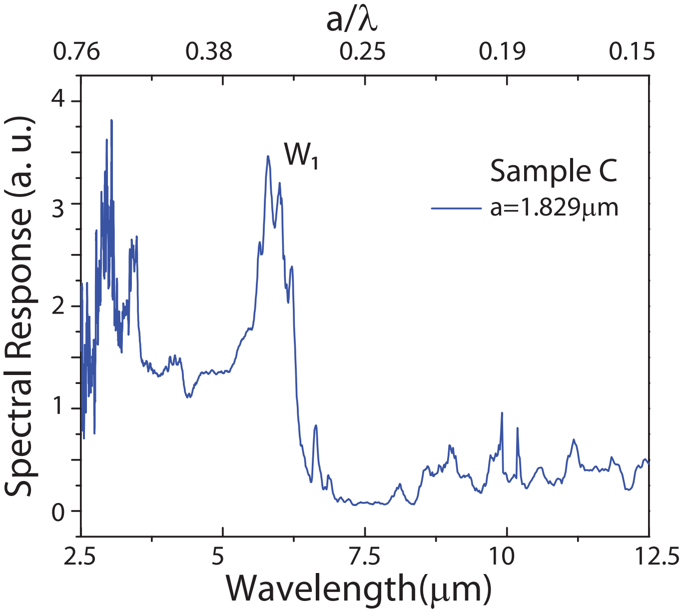

Figure 4.11: Normalized spectrum from detector with a thick absorber and an inductive grid (sample C). The fundamental waveguide mode is visible in the spectrum.

The measured responsivity and detectivity from devices patterned with an inductive grid at 77 K is shown in Figure 4.12. These devices show a responsivity of 0.27 A/W and a high detectivity of 6.5 $\times 10^{10}$ cm.$\sqrt{Hz}$/W at 77 K. The detectivity measurements were done with a background irradiation of 2π FOV, instead of f/2 FOV used in chapter 3. An enhancement of 2.2× has been observed for the response when compared to the sample without a surface pattern. Note that the observed enhancement for waveguide modes are lower than that for plasmon modes. In systems where enhancement over a broad spectral range is desired, both plasmon and waveguide modes can be excited to provide gain over a set of discrete wavelengths or a wide waveband.

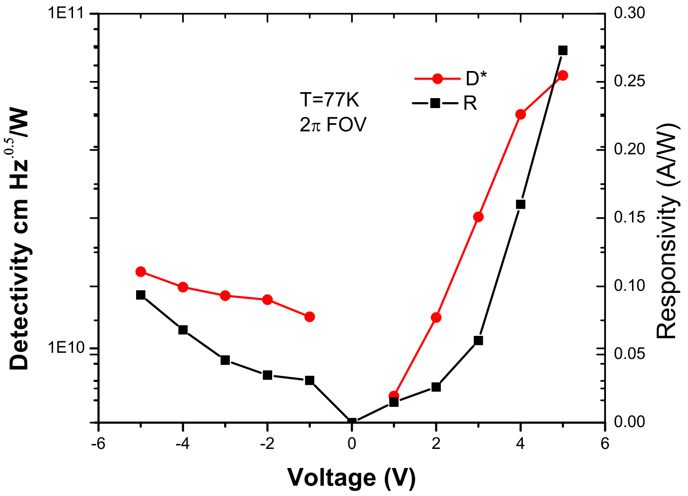

Figure 4.12: Measured responsivity and detecitivity from sample patterned with an inductive grid, measured at 77 K

4.4 Conclusion

The origin of resonant peaks in plasmonic DWELL detector is analyzed in this chapter. The simulated absorption features are compared to the surface field intensity and spatial distribution of fields to identify their characteristics. Three detectors samples, comprising of two active regions of different thicknesses and a different surface pattern, are analyzed. Two enhancement mechanisms are observed in these devices. Using inductive and capacitive grids as surface patterns, waveguide and plasmon modes can be selectively excited within these detectors. Measured spectra show the presence of several modes of absorption, which are classified. Use of a thin absorber with an inductive grid shows excitation of plasmonic modes, while a thicker absorber with an inductive grid excites waveguide modes. An enhancement of 2.2 was observed for the response from waveguide modes and 4.9 for plasmon modes.

Chapter 5

Conclusion and Future Work

5.1 Conclusion

In this work, improvements in DWELL infrared detectors that make them suitable for third generation infrared systems are examined and implemented. DWELL detectors offer several inherent advantages when compared to existing technologies. A low noise, resonant nature of detection, the ability to tune absorption wavelength ,and use of III-V technology make them attractive for enhanced functionality focal plane arrays. This work focuses on two key characteristics of future infrared systems: High temperature operation and multispectral/polarization detection.

Improved operating temperatures were demonstrated for LWIR detectors, by using new DDWELL based designs with thicker active regions. and lower dark currents. The strain introduced in the system was minimized by changing quantum well material to unstrained GaAs from $In_{0.15}Ga_{0.85}As$. In the new design, amount of $In_{0.15}Ga_{0.85}As$ is kept to a minimum, by using it only as a strain bed and a capping material. Several cycles of optimization were performed. PL, AFM and XRD were the tools used for optimizing the structure. The final dot-in-a-double-well design consisted of InAs dots embedded in $In_{0.15}Ga_{0.85}As$ /GaAs quantum wells, with $Al_{0.10}Ga_{0.90}As$ as the barrier material. This system shows a lower PL wavelength when compared to QDs from the standard DWELL structure, indicating better confinement. A 3× improvement is observed in the dot density.

Detectors fabricated using DDWELL design exhibit a dual color spectral response and the ability to tune spectral response with bias voltage. Devices with peaks in MWIR and LWIR regions were measured. The peak wavelength of absorption is different for positive and negative bias polarities. Spectral response was observed till 140 K for the LWIR peak, making these one of the highest reported operating temperatures for QD based LWIR detectors. Calibrated radiometric measurements were performed on devices to measure signal and noise. Optical scattering from open areas between pixels and from the substrate creates additional photon collection. Measurements where scattering is not accounted for leads to overestimation of responsivity in these devices. Efforts were made to measure detectors with different apertures to minimize the amount of scattering. Use of thin metal layers to block open areas of the mask were also performed. The detectors show a responsivity of 0.24 A/W at a bias of 5 V for a wavelength of 9.4 μm and 0.89 A/W at -5 V for a wavelength of 8.7 μm. High detectivities of 1.8 $\times 10^{10}$ $cm.\sqrt{Hz}/W$ at 4 V for 9.4 μm and 6.7×10^{10} $cm.\sqrt{Hz}/W$ at -4 V for 8.7 μm were observed for a f/2 FOV. DDWELL devices show a factor of 10^4 reduction in dark current density over standard DWELL designs.

In the second part of this work, multispectral and polarization sensitive absorption is demonstrated providing additional functionalities to DWELL based detectors. A subwavelength metal nanostructure is integrated with infrared detectors, resulting in the excitation of resonant surface plasmons at the metal semiconductor interface. A coupling of DWELL intersubband absorption with plasmons results in peak absorption of the detector, dependent on pitch and shape of the surface pattern. FDTD simulations were performed to estimate and analyze the effect of integrating surface patterns with the detector. The propagation through subwavelength hole arrays was modeled and large area structures were fabricated for testing. Simulations show several resonant absorption features that vary with pitch of the array. An enhancement of absorption is also predicted. Use of a square hole pattern in a square lattice results in the presence of two degenerate modes of absorption, each strongly dependent on incident polarization. By stretching and compressing the lattice, these modes are separated in wavelength, and can be used for polarization sensitive detectors.

Surface patterns with square lattice and rectangular lattice were integrated with DWELL and DDWELL based detectors. The lattice constants were scaled to include MWIR and LWIR regions. Measured spectra show a response whose peak scales linearly with pitch of the pattern. The shape of spectra observed are different from the control sample spectra. Spectral tuning from 5.5 to 7.2 μm and 8.5 to 9 μm is measured. Several modes of absorption are observed in measurements, whose peak wavelengths agree well with simulated values. The responsivity and detectivity of patterned samples is enhanced, when compared to a control device of the same wafer, but without the surface pattern. Enhancements are observed across MWIR and LWIR regions. A peak enhancement of 4.9 is measured. Dark current measurements indicate no significant increase on surface patterned detectors.

Enhancement mechanisms in plasmonic infrared detectors are studied to understand and engineer their aspects. Simulations indicate the presence of plasmon and waveguide modes in these devices. Both of these modes are predicted to enhance absorption. In order to study enhancement properties of each type of mode individually, surface patterns that selectively excite one type of modes over the other were integrated with the active region. The thickness of DWELL region is varied, to modify the spatial overlap of energy with the absorber. Plasmon modes, waveguides modes and a combination of the two are selectively excited. Spectral measurements from these devices indicate the excitation of several modes, and a possible coupling between them. An enhancement factor of 2.2 is observed for waveguide modes and 4.9 for plasmon modes.

Encoding spectral and polarization information in a pixel can be achieved by a one step lithography using the methods described above. This technique is simple, cost effective and is independent of the detector technology used. Possible future directions including demonstration of a multispectral FPA, integration with other IR technologies and improved designs are discussed in the following section.

5.2 Future Directions

5.2.1 Plasmonic Enhancement for Other IR Technologies

The improvement in detector performance with the integration of surface plasmon based cavities is not limited to DWELL detectors. The methods used in chapter 3 can be applied to most IR technologies currently used [93]. The integration of surface patterns with an IR detector is independent of the detector technology used, and can be used with IR technologies already deployed. Recently, integration of plasmonic patterns with a QWIP has resulted in its performance improvement. These devices have been able to absorb normally incident light, and show improvements in detectivity [68]. Here, the integration of surface patterns with a bulk-like detector is discussed, using SLS material system as an example.

SLS detectors use transitions between minibands formed in a InAs/(In)GaSb superlattice for infrared detection [94, 95]. The InAs/GaSb band heterostructure has a type-II broken band alignment, with the conduction band of InAs 0.129 eV lower than the valence band of GaAs. When grown as a superlattice, this creates electron and hole wavefunction localization. Infrared detectors based on these materials use transitions between electron and hole minibands for detection. SLS detectors have several advantages over conventional IR materials. They use processing and growth techniques of III-V materials, have better uniformity and are cheaper when compared to HgCdTe based systems. The bandgap and bandalignment of the superlattice can be changed using the composition of InAs/GaSb layers. Detectors in MWIR, LWIR and VLWIR have been demonstrated using SLS technology [96–98]. The performance of SLS detectors is comparable to that of HgCdTe detectors, the state of the art technology in LWIR systems.

The absorption coefficient of SLS layers is dependent on the electron-hole wavefunction overlap. For MWIR devices, the overlap is high and thin layers of SLS can be used to have high quantum efficiencies. The overlap decreases for LWIR designs. With increasing wavelength, the quantum efficiency is found to be lower for the same active region thickness. Though InAs and GaSb are lattice mismatched, use of strain compensating InSb like interfaces or a layer of InSb grown between InAs and GaSb have shown to relieve the strain [99]. Thus, it is possible to grow thick layers of SLS without degrading the performance. SLS detectors have shown QE of 35 % in MWIR FPAs and 20% in LWIR detectors [97, 100].

The spectral response of SLS detectors exhibit a broad profile, with no features except the cut-off wavelength. The major advantage of integrating plasmonic cavities would be to sense specific wavebands, which can be tuned by changing the surface pattern [82].

Enhancement of SLS Detectors

The analysis used in chapter 3 assumes the use of a low loss semiconductor and a metal with higher losses for coupling to plasmons. As a result,the evanescent field extends has a longer tail into the semiconductor than the metal. DWELL structures provide a low loss absorber, which does not perturb the properties of the surface plasmon at the metal-semiconductor region significantly. As the quantum efficiency increases, the loss associated with the material increases. Simulations were performed to analyze the effect of integrating a high QE material with plasmonic patterns etched into the surface. The structures simulated are identical with the ones shown in Figure 3.6, except for the high loss. Simulations were performed for a material system with 10%QE. The absorption plot obtained is shown in Figure 5.1.

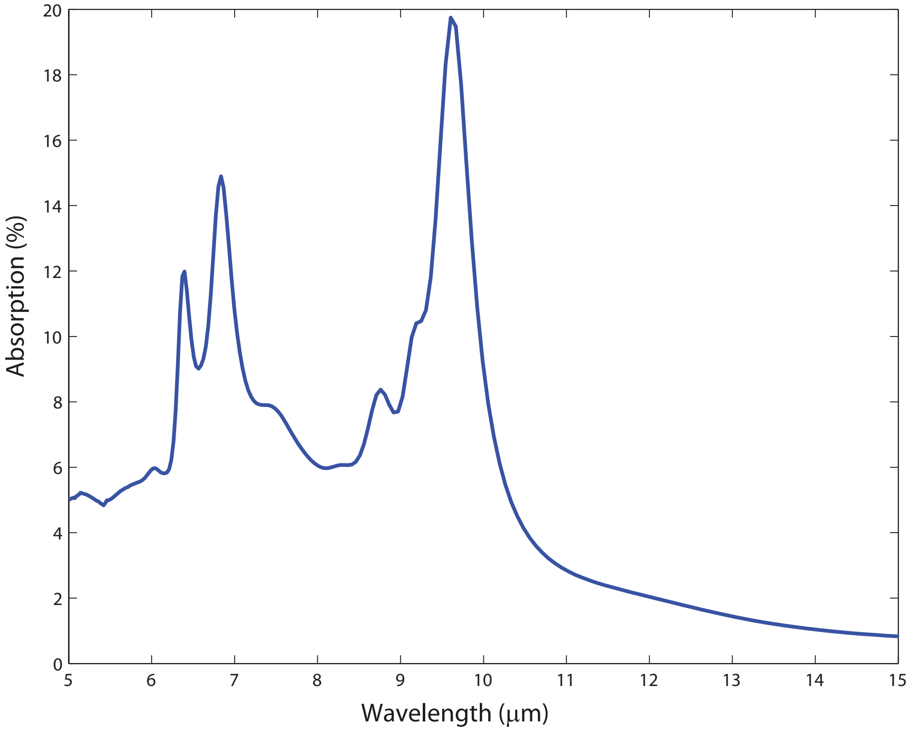

Figure 5.1: Simulated absorption of a device with 10% single pass QE. The spectral peaks are no longer prominent due to high damping loss of the system.

The absorption plots show two clear peaks corresponding to the first and second order plasmon excitations. The resonance, however, is not sharp and the features have a low Q. The high loss of the SLS layer underneath the top contact increases damping loss of plasmons, and as a result a broad spectra is observed. The peak absorption is 17%, showing an enhancement factor of 1.7. This shows that a direct integration of patterns with existing IR structures will not yield optimal results. To obtain selection between spectral features, the losses encountered in the semiconductor region need to be reduced. The QE, and hence the loss associated with absorption can be reduced by having thinner active regions with lower QE. Plasmonic enhancement would also be more viable in the LWIR regime, where lower absorption coefficient of the SLS material can be exploited.

Several SLS diodes use a homojunction bottom contact, where a highly doped SLS layer having the same composition as the absorber is used as a bottom contact [100]. Incident IR radiation is absorbed in the active region as well as the contacts. Use of thick doped regions as bottom contacts, necessary for a good bottom contact during large area etching (critical for FPA fabrication) increases single pass absorption QE of the detector. Integration of plasmonic features would not be effective on these structures. Processing of these designs into detectors, leaving large open areas in the mask, leads to optical scattering. This acts as an additional photon collection area, and corrupting experimental measurements.

The use of cladding layers in DWELL detectors has improved the enhancement factor and confinement of plasmon assisted detectors. Experimental measurements indicate a superlattice refractive index of 3.78, providing little contrast with GaSb (n=3.8) [101]. Hence, conventional SLS structures using a GaSb substrate would provide very low confinement. A natural cladding can be obtained for SLS detectors by growing them on GaAs substrates, instead of GaSb substrates. Several research groups are trying to explore growth on GaAs substrates, as they are cheaper[102, 103]. The use of interfacial misfit (IMF) layer growth mode has been successfully demonstrated at UNM, leading to defect free GaSb on GaAs [104, 105]. Infrared detectors using this technique have been demonstrated in MWIR and LWIR regions. The use of an IMF layer mode to grow a thin MWIR absorber based detector structure on

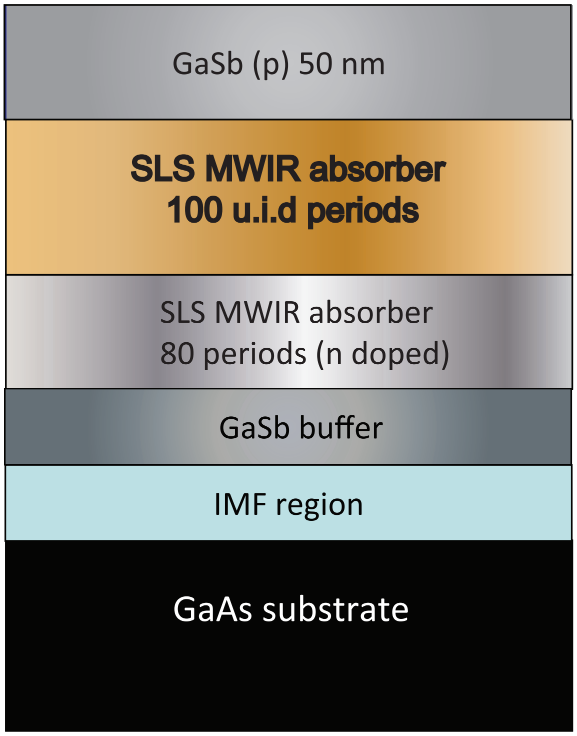

Figure 5.2: SLS device grown on a GaAs substrate. A thin absorber is used to minimize QE for the detector.

a GaAs substrate is proposed for generating plasmonic absorption features in SLS devices, as shown in Figure 5.2. The critical component in this structure would be growth of defect free SLS layers on GaSb, to limit dark current of the detector. Subwavelenth patterns can be directly integrated with this device, without altering the process flow.

5.2.2 Multispectral DWELL FPA

Integration of plasmonic resonators with a DWELL absorber has demonstrated enhancement of responsivity and detectivity of detectors, both in MWIR and LWIR regions. Multi-spectral and polarization sensing is another feature of these detectors.

A demonstration of a multi-spectral FPA with an enhanced absorption would have a tremendous impact on IR sensing. With enhanced QEs, DWELL based FPAs can be considered for third generation IR systems. Monolithically integrated multi-spectral FPAs can be more cost efficient too.

The detectors described in chapter 3 are front side illuminated. Plasmonic patterns are integrated on top contact of the as grown structure. In contrast, most III-V FPAs currently used are back side illuminated. The FPA is processed from the front side and is flip chip bonded to a silicon ROIC using indium bumps. Each FPA is flip chip bonded individually, making it a serial process which is difficult to scale up. The substrate is then removed and the FPA is illuminated from the backside.

For an enhanced absorption, DWELL absorber should be present in the near field region of the evanescent field decaying from the metal-semiconductor interface. Two schemes are proposed for integration of plasmonic structures with a FPA. In one method, the FPA is processed, flip chip bonded and the substrate removed before integrating plasmonic patterns. The pattern can then be integrated in a single lithography step and metal deposition.The lithography for the plasmonic pattern and the metal deposition are done on an already diced and bonded FPA. A schematic of the finished FPA is shown Figure 5.3. The plasmonic pattern interacts with the incident light in a similar way as a single pixel detector described in chapter 3. The confinement of the field would be higher in this scheme, as the pattern is integrated with a thin semiconductor region. The thick substrate that limits the index contrast in a single pixel detector is absent in the case of an FPA and this can lead to a higher confinement. A drawback of this method is the serial processing required for the final lithography step.

For wafer level integration, a process in which the FPA has a finished plasmonic pattern before dicing is required. This can be accomplished by processing the pattern on the flip chip bonded contact (top contact) of each individual pixel. The plasmonic

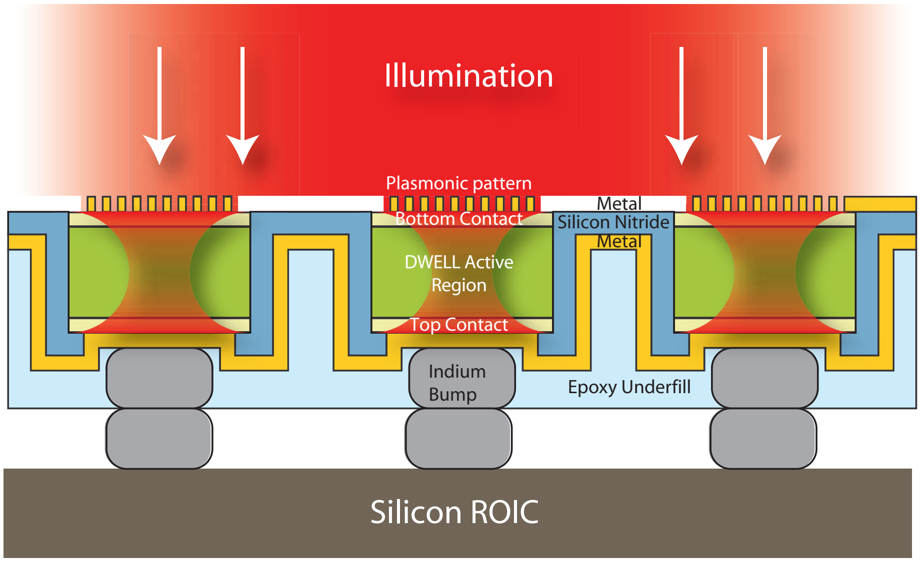

Figure 5.3: Schematic of a plasmonic FPA. The FPA is conventionally processed and the metal nanostructure is integrated on to the backside. An additional lithography step is the only additional step to current processing schemes to fabricate a multispectral FPA.

pattern is processed initially, and the material is etched to define pixels afterwards. Thus the pattern would be on the indium bump side of the FPA, rather than at the illumination side, as was the case before. The use of indium bumps and an underfill epoxy between the ROIC and the FPA reduces the index contrast for the plasmonic pattern. Use of low index dielectrics like silicon nitride can be explored to provide necessary index variation. A single pixel detector, in which enhancement is dependent on the direction of illumination, has been demonstrated recently[106].

Infrared Superpixel

The dependence of absorption peaks on pitch of plasmonic pattern can be used to fabricate FPAs with the ability to simultaneously image scenes in different wavelengths. To this end, an "infrared superpixel" can be used as the unit cell of detection, instead of using an individual pixel. The superpixel consists of several pixels of the FPA, each patterned with a slightly different pattern sensing a different wavelength. A schematic is shown in Figure 5.4 for a 4 band multi-spectral FPA. The superpixel unit cell has 4 individual pixels and is repeated with double the original pitch across length and breadth of the FPA. This method makes the fabrication of multiband FPAs cheaper and more efficient, and does not require external filters. In this example, images in a specific waveband will have half the original resolution along each of the two dimensions.

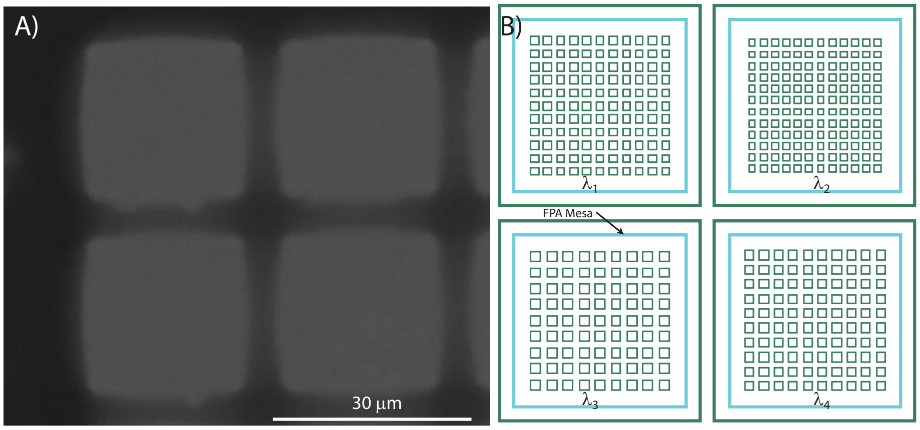

Figure 5.4: A) SEM images of fabricated FPA pixels. A 2×2 array of individual pixels is used as a superpixel. The image is taken from the backside of a bonded and substrate removed FPA. B) Schematic of the superpixel lithography mask. Each pixel has a subwavelength pattern resonant to a different wavelength.

Further research is required to fabricate ROICs with the ability to pick and choose pixels to create images of a specific wavelength. The superpixel concept also needs to be optimized for the optimal number of wavebands and their placement in MWIR and LWIR for maximum spectral resolution. The human eye is able to image the entire visible spectrum with just three different sensors with a large overlap between them. A linear combination of the different wavebands sensed can be used to provide a higher wavelength resolution than individual pixels. An algorithmic spectrometer, using the bias tunability of the DWELL design, uses a similar technique to provide narrow filters in the 3-12 μm region[107]. The geometry of the superpixel is another consideration for active research. The schematic shows a square geometry, which conforms to the current ROIC architecture. Other geometries that minimize the registration error and the FPA bandwidth efficiency can also be considered[108].

All the plasmonic patterns shown in this thesis have been fabricated with e-beam lithography. For a response in the MWIR region, the hole width of the plasmonic pattern becomes sub-micron and reaches the limit of conventional optical lithography. For single pixel prototype fabrication e-beam lithography provides a viable alternative. The area to be patterned in a 320×256 FPA is $\approx$1 cm^2 and use of e-beam lithography would be time consuming and expensive. Alternate lithography techniques like interferometric lithography (IL) need to be explored for large scale FPA fabrication.

5.2.3 Double Metal Waveguide Infrared Detector

The factors limiting the performance of a plasmon coupled FPA are external coupling loss, metal loss and substrate loss. The substrate loss is directly related to the coupling of incident radiation to the active region and increases with the coupling. A critical coupling regime [58, 109] can be achieved by matching the input coupling losses to losses within the detector. A double metal waveguide based design, in which the active region is confined within a thin layer of metal on either side, is proposed to this end. In a DMWG based design, the substrate loss is absent as the substrate is no longer associated with the active region. With the DMWG design, it is possible to match the external coupling losses to the detector losses, and a high absorption can be achieved [58]. A DWMG metamaterial based absorber has recently been demonstrated with a 95% absorption in the IR region[110].

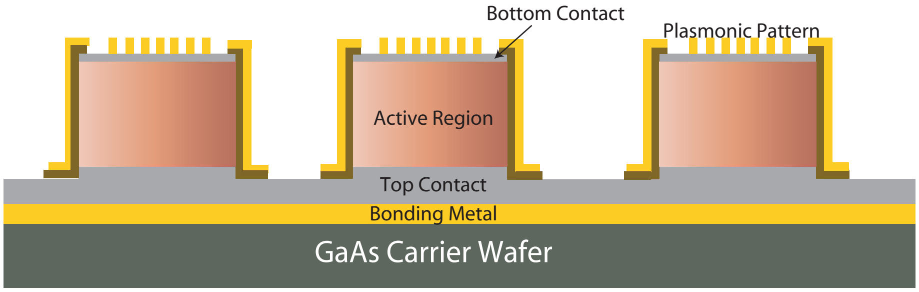

Figure 5.5: Schematic of a double metal waveguide detector. The wafer with the active region is flipped and bonded with the carrier wafer though a metal-metal bonding process. The substrate is removed, and the exposed active region is processed into detector pixels

In order to enclose the active region between metallic waveguides, the substrate should be completely removed and the exposed region metalized. To facilitate processing the wafer with the active region can be bonded to a carrier wafer using pressure bonding or eutectic based bonding, and the substrate removed [111–113]. DMWG based lasers have been demonstrated using this technique. A schematic of the DMWG detector is shown in Figure 5.5. Once the device is bonded and substrate removed, single pixels can be processed using standard techniques. In a DMWG device, the active region is electromagnetically isolated from the handler wafer through a thick metallic layer. Thus, a large index contrast can be obtained between the active region and the surroundings, increasing the confinement. The need to embed the absorber in metallic regions can easily be achieved in conventional FPA processing, as the device is flip chip bonded with no substrate. An additional lithography step would make the conventional FPA a DMWG device. The DMWG architecture can easily be implemented in a flip chip based processing technique without altering the current processing steps.

Appendix A

Characterization

A.1 Sample preparation

For measurements, detectors need to be cooled down to a low temperature, where SNR is high. Typical temperatures range from 12 K to 160 K. A closed cycle He cryostat or a liquid nitrogen cooled cryostat is used, providing a temperature range from 12 K to RT. The cryostats have KBr windows, providing high transmission in MWIR and LWIR regions. Other materials that may be used include CaF_2 or thallium halogenide (KRS) in appropriate spectral windows. Devices are diced into individual dies, wirebonded, and mounted on a 84 pin lead-less chip carrier (LCC). A thermally conductive epoxy or soft metals like indium can be used for mounting. The bonding is done with a commercial wire bonder having both ball and wedge bond options. For samples with a rough or non-uniform metal contact surface, ball bonds are difficult to stick. The excessive force used in bonding can damage the device. Ball bonds, however, provide a better stability during thermal cycling, if adhesion between bond and contact metal is good. The noise introduced from ball bonds is lower when compared to wedge bonds. In this work, use of ball bonds has been preferred whenever measuring devices with low noise.

A.2 Spectral Response

Spectral response is measured using a FTIR. An optical image of the measurement setup used is shown in Figure A.1. IR beam from the FTIR is taken out to an external chamber and focused onto the detector mounted inside a close cycle cryostat, using a parabolic mirror. Normalization of the output spectrum is performed, for the source spectrum and transmission through atmosphere, using a deuterated triglycerine sulphate (DTGS) detector.

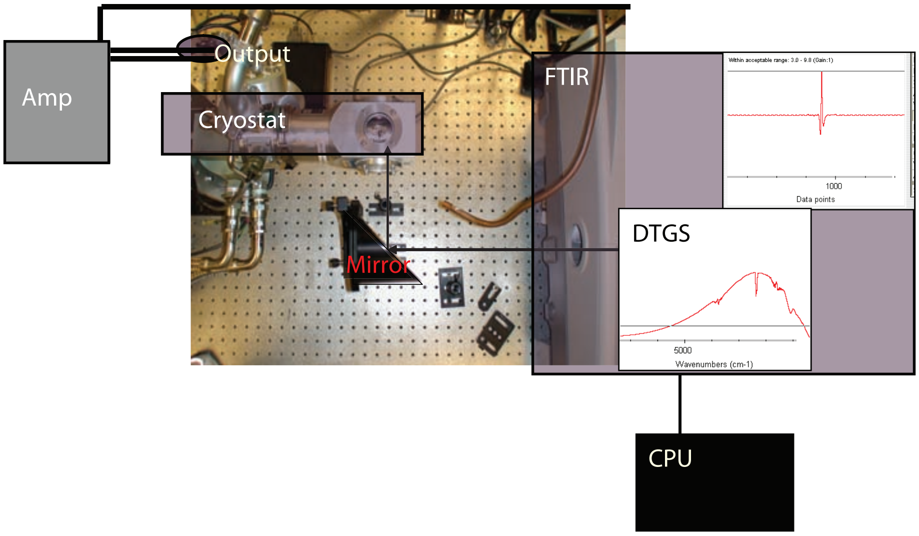

Figure A.1: Schematic of spectral response measurement setup. A closed cycle cryostat based on liquid helium is used with an FTIR for measurement. Images courtesy Greg Bishop.

A.3 Responsivity

Responsivity of a detector characterizes its performance in terms of the photocurrent produced per unit value of incident photon flux. Using responsivity as a metric, detectors of different sizes can be characterized for the amount of signal generated. A schematic of the responsivity measurement setup is provided in Figure A.2. The detector is illuminated with a calibrated Mikron M365 blackbody at 800K modulated with a chopper. The chopper frequency is used as a trigger for the SRS760 fast Fourier transform (FFT) spectrum analyzer. A SRS 570 low noise transimpedance amplifier, that biases the devices and amplifies the measured photocurrent, provides gain to the measurement system. The device is mounted in a liquid nitrogen cooled cryostat equipped with a heater, providing a temperature range from 77 K to RT. In order to account for any errors that may be present in the measurement geometry, a calibrated InSb detector is used as a benchmark during each measurement. The ratio of measured values of InSb responsivity and its acutal calibrated value provides a scaling factor for DWELL responsivity. The peak responsivity of the device is then measured as,

$$R_p = I_0 \bigg/ \int_{\lambda_1}^{\lambda_2} R_N(\lambda) L_e(\lambda, T) A_{BB} A_{opt} \frac{tF_F}{r^2} d\lambda \tag{A.1}$$

where $R_N(\lambda)$, I_0, L_e, A_{BB}, A_{opt} are the normalized spectral response, measured photocurrent, the black body spectral excitance, area of the blackbody source , optical area of the detector and r, t, F_F are the the distance between the source and the detector, the transmission of the window and geometrical scaling factor respectively.

Presence of optical scattering provides a major challenge in measuring exact values of responsivity in DWELL detectors. For a constant photon flux, the amount of signal measured in a device scales linearly as its active optical area. Optical

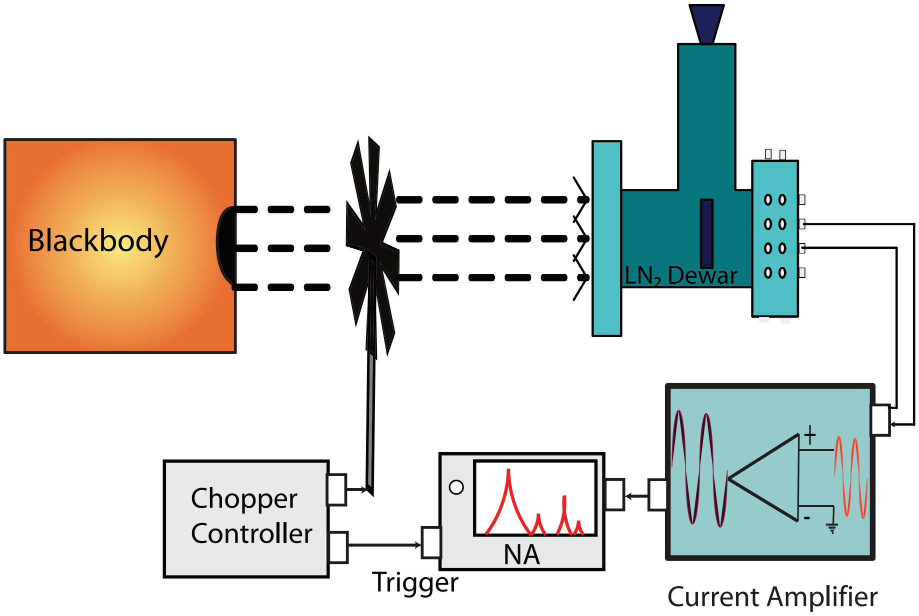

Figure A.2: Schematic of responsivity measurement setup. The same setup without the blackbody and chopper is used for noise measurements.

scattering manifests as an additional photon collection area for the device, outside its active optical area. This may be due to the presence of a thick substrate or open areas in the mask contributing to additional photons reaching the active region. A good estimate of optical scattering can be made by measuring devices with different aperture sizes in each detector die. A plot of the signal obtained from devices with different optical area is shown in Figure A.3. In an ideal case, this graph would pass through the origin. The x intercept of this graph provides the additional collection area, which can be used in Equation A.1 to estimate responsivity accurately. Note that the values of all the other variables Equation A.1 need to be constant during this measurement.

Another option to prevent optical scattering is the use of masks with no open

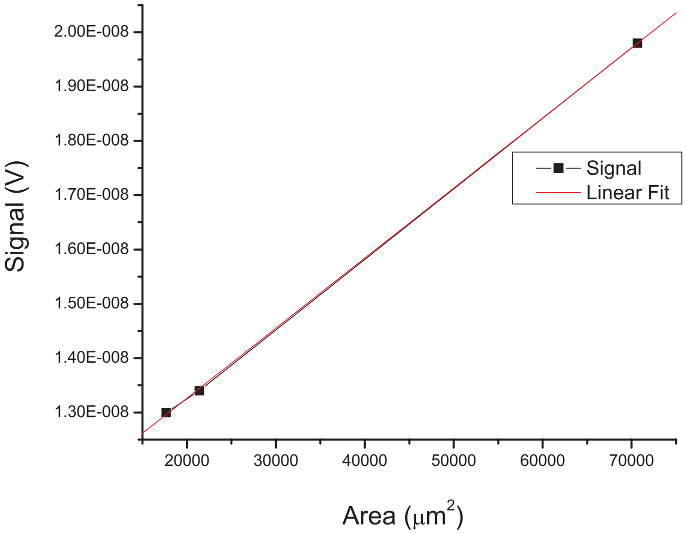

Figure A.3: Signal of the detector measured as a function of the area of the aperture. A non-zero offset is obtained, indicating presence of optical scattering.

regions between bottom contacts. All radiation incident on areas other than the optical area are reflected away, limiting scattering. For measuring nanostructure integrated devices described in chapter 3, this method was preferred. The spectral response is dependent on the absorber as well as the integrated pattern. Thus, response each device is different from that of its neighbor and from the scattering area. To ensure that light is coupled only through the patterned optical area, all other regions were covered with metal while measuring these devices.

The responsivity of a DWELL detector is related to the quantum efficiency as

$$R = \frac{\eta \lambda g q}{hc} \tag{A.2}$$

where g is the photoconductive gain of the system. The responsivity and quantum efficiency as a function of wavelength can be obtained from the peak values calculated above as

$$R(\lambda) = R_p R_N(\lambda) \tag{A.3}$$

A.4 Detectivity

Detectivity of a IR detector is a normalized metric for SNR. The signal is measured to the area of the device (responsivity) and the noise measured is normalized to both area and integration time. The background noise from the detector can be measured using the setup described in section A.3. The detector is illuminated with a background scene (with no blackbody), and the average noise PSD measured directly from the spectrum analyzer. The major noise sources in a DWELL detector are

- 1/f noise
- Shot noise
- Johnson noise

In order to determine the shot noise, noise PSD from the detector is measured at a frequency f>400 Hz. At lower frequencies, the 1/f noise dominates other noise sources. This can be observed as a uniformly decreasing noise psd with frequency in the FFT analyzer. For unpassivated devices, the contribution from 1/f noise increases with time, and non-flat PSD can be observed at higher frequencies, extending to the KHz range. At higher frequencies(f>4KHz, Johnson noise starts dominating the detector performance. In all devices presented here, attempts have been made to measure shot noise.

Ensuring that source of noise measured is the detector is very critical. Other electrical systems operating can introduce noise, which can drown noise from the detector. This will lead to incorrect determination of detector noise and hence detectivity. Several groups estimate detectivity from the dark current [114], but the device will not match the performance of estimated numbers. The performance of an FPA is ultimately determined by the measured SNR. Thus, an exact measurement of noise is necessary to replicate the performance of a single pixel detector in a FPA. Use of closed cycle cooling systems instead of liquid cooled cryostats increase system noise. This can lead to incorrect noise measurements, if measured at low temperatures and for detectors with low noise PSD. For the He based closed cycle cryostat described in section A.1, the cryostat noise overwhelms the detector noise at temperatures lower than 50 K. All noise measurements described have been performed at T$\geq$ 77 K using a liquid nitrogen cryostat.

The detectivity (D*) can be calculated from measured noise PSD and responsivity as

$$D^* = \frac{R\sqrt{A_d}}{PSD} \tag{A.4}$$

where A_d is the total area of the detector. The noise PSD is normalized with the net detector area, as this entire area contributes to noise current. In detector structures described in Appendix B, this is the entire mesa area. This is different from the optical area of Equation A.1, which is the area of the aperture. The noise PSD is related to the noise current as

$$PSD = \frac{i_n}{\sqrt{\Delta f}} \tag{A.5}$$

where i_n is the noise current, and $\Delta f = 1/(2t)$, and t is the integration time used. The noise PSD, however, can directly be measured from the FFT analyzer.

Appendix B

Processing

B.1 Single Pixel Detector Processing

Processing of a single pixel infrared detector involves the following steps.

- Mesa etching
- Passivation
- Contact Metalization
- Rapid Thermal Annealing

The patterns for each step are transferred to a photoresist (PR) using contact optical lithography. The smallest features in this set of masks is 5 μm, which makes contact lithography ideal for large scale device fabrication. The lithography is performed using a MJB3 aligner, with the ability to process 3" wafers. The photoresist used for patterning is dependent upon thickness and depth of the underlying feature. For DWELL devices with active region thickness between 1 and 3 μm, AZ 4330 positive tone resist is used. A adhesion promoter like hexamethyl di silacene (HMDS) may be used to promote bonding of photoresist with the wafer. A schematic of the process flow is shown in Figure B.1.

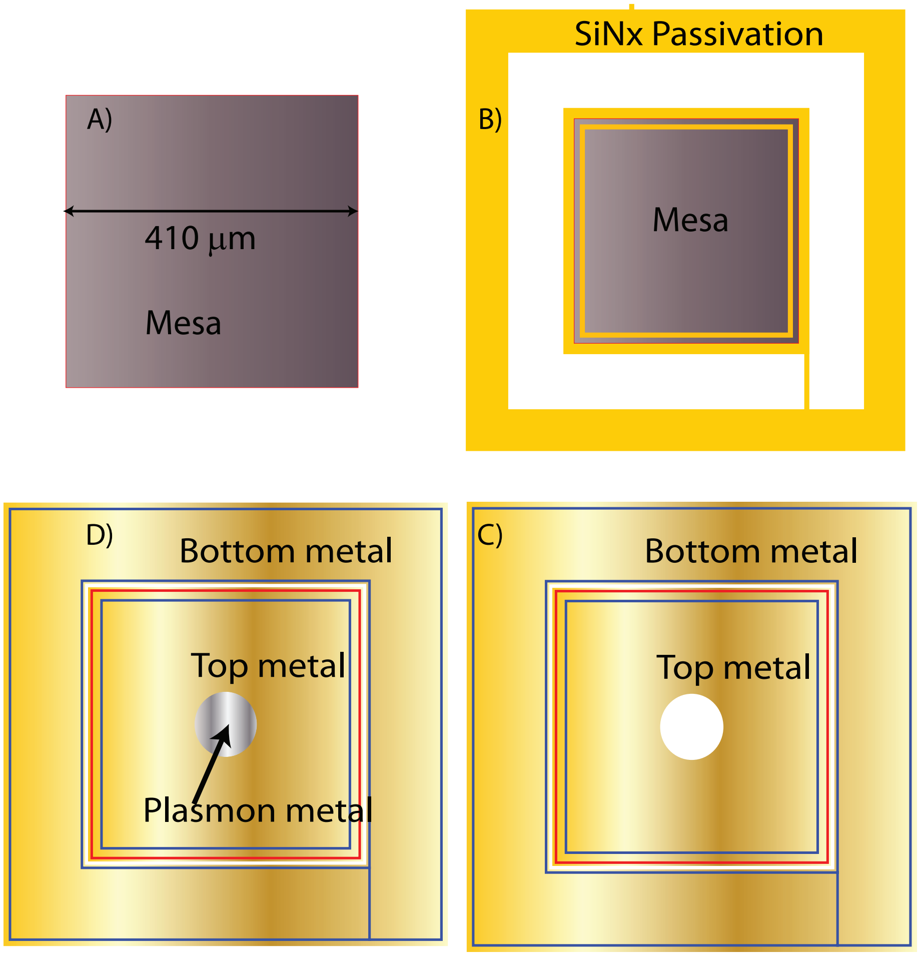

Figure B.1: Schematic of single pixel fabrication. The top view of various features is shown. A) Mesa etching; B) SiNx deposition and etching; C) Contact metal deposition D) Plasmon metal deposition. All features in a subfigure are drawn to scale with each other.

Devices can be isolated electrically by using dry etching, creating spatially separated pixels, or using lateral diffusion of carriers to separate individual pixels[100]. In this thesis, a dry etch process has been used to created mesa structures, to physically isolated devices. The pixel sizes are 410 μm × 410 μm square mesas. BCl_3 is used as the etchant using an inductively coupled plasma (ICP) etcher, with a ICP power of 500 W and RIE power of 90 W. The etch is anisotropic in nature and provides vertical sidewalls. The etch rate ratio of PR to the active material is ≈1:3. ICP is mostly a physical etching process, where the bombardment of ions causes removal of material. This can cause roughness and material damage on the newly etched surface. A wet etch, which is entirely chemistry based, is used to smoothen the etched surface and limit damage. A 50:1 mixture of citric acid and hydrogen peroxide, with an etch rate of ≈50 nm/min, is used. Hydrogen peroxide, being a spontaneously dissociating compound, the concentration varies with time. This affects pH of the etching solution. The pH of the etching solution was monitored and kept constant, for a repeatable etch rate.

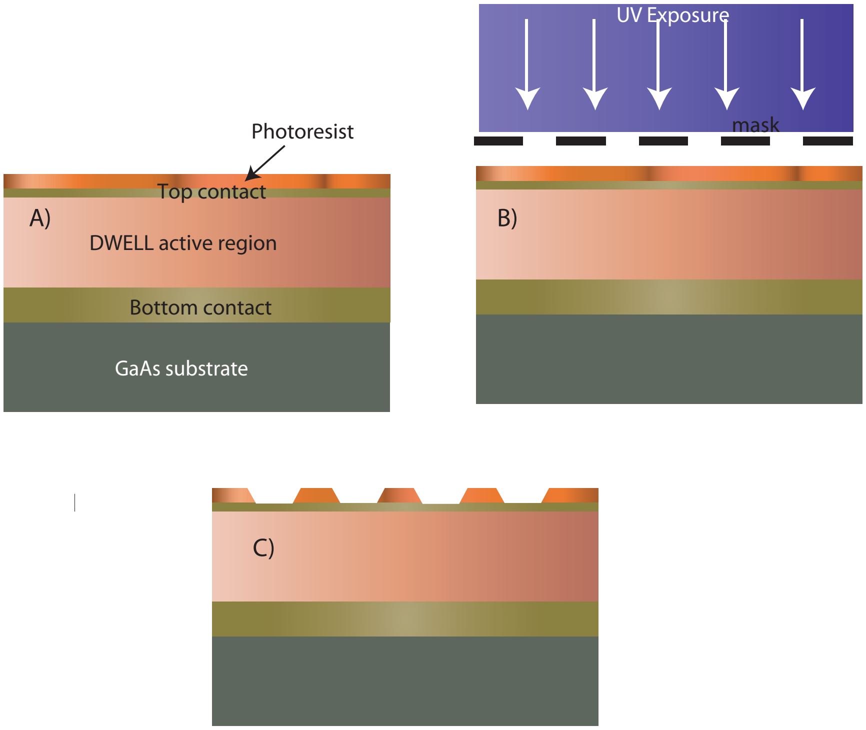

Figure B.2: Illustration of lithography for patterning. A) Wafer coated with photoresist. B) Exposure with mask. C) Features are formed after development. The mask for mesa patterning is used as an example.

A passivant covers the exposed edges of the mesa and the exposed region. SiNx is used as a passivant in all devices presented in this thesis. SiNx is deposited using a PECVD process, using NH_3, SiH_4, and N_2 at 300 °C. A high temperature process provides denser nitride and limits the leakage current through the dielectric. The thickness of the film is between 100-200 nm, to avoid cracking from the high stress nature of thin film SiNx, but sufficiently thick to prevent leakage currents. Following the deposition, photolithography is performed and SiNx is etched away from regions forming top and bottom contacts. Unetched SiNx covers the sidewalls of the mesa, and regions between detector pixels. A dry etch, using a combination of CHF_3 and O_2 or CF_4 is used for etching. Use of buffered oxide (wet) etch (BOE) solution is another option. An illustration is shown in Figure B.1 B).

The contact metal is then deposited through photolithography, e-beam metal evaporation and liftoff. The n-contact metal for GaAs is Ge/Au/Ni/Au. The thicknesses are 26 nm, 54 nm, 15 nm and 300 nm respectively. As deposited, this contact has a Schottky barrier for n-GaAs. A rapid thermal anneal is then performed at 380 °C for 60 s to form an ohmic contact. During this anneal process, Ge and Au layers diffuse into the semiconductor region, forming a thin highly doped region at the surface. Ni acts as a diffusion barrier and the top layer of Au provides a low value of top contact resistance. A clear field mask is used with a negative resist (normally AZ 5214 E-IR) for the lithography. As illustrated in Figure B.3 C), the contact metal covers edges of the mesa, and prevents light leakage into the active region. Optical scattering cannot be completely eliminated , however, due to the presence of open spaces between detectors.

For plasmon integrated devices, the fabrication of the subwavelength pattern is performed using e-beam lithography. Inductive grids are fabricated through an initial metal deposition process, followed by e-beam lithography and Ar based dry etching. Capacitive grids on the other hand, can be fabricated directly using a e-beam lithography, metal deposition and liftoff. This difference in process is necessitated ,as the area to patterned is lower for a positive tone e-beam resist, minimizing lithography time.

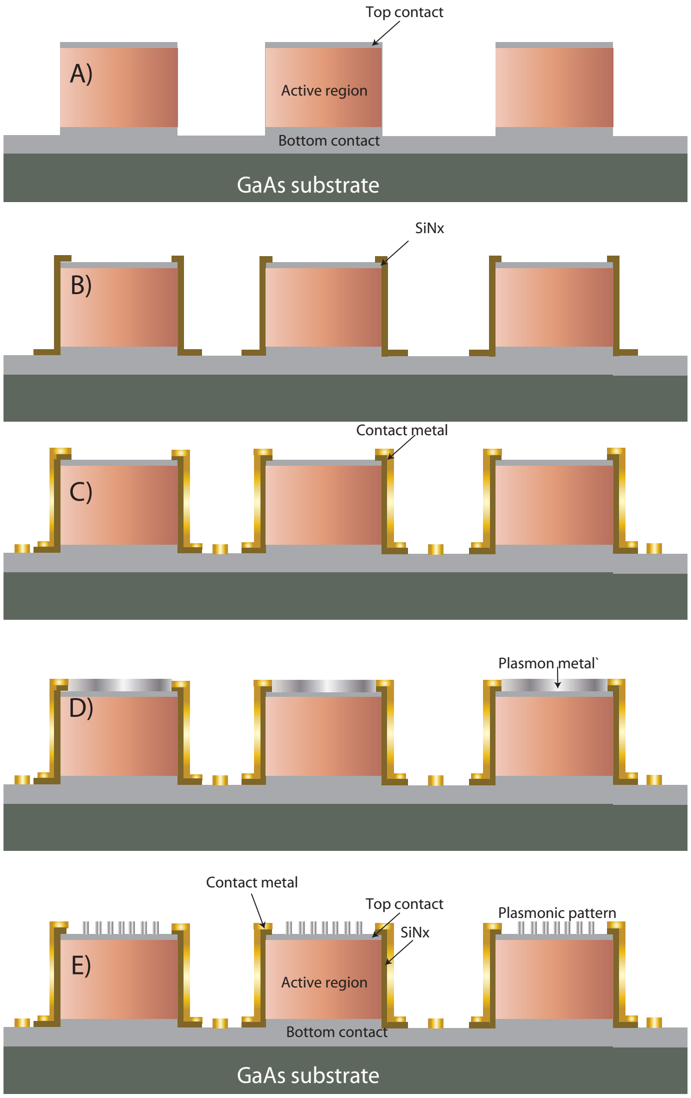

Figure B.3: Fabrication of a single pixel detector. A) Mesa etching. B) Passivation C) Contact metal deposition D) Plasmon metal deposition E) E-beam lithography and etching/liftoff. Steps D) and E) are performed for integration of subwavelength nanostructures with the processed detector.

B.2 Wafer bonding

For fabrication of DMWG devices described in subsection 5.2.3, the active region needs to bonded to a carrier wafer and the substrate removed. Two methods, both of them using a metal-metal bonding have been attempted. In the first method, a thick layer of Au (1 μm) is deposited on the carrier wafer and n-GaAs contact metal is deposited on the grown wafer. These wafers are then bonded together at high temperature (330 °C)and pressure for 30 minutes, to create a strong Au-Au adhesion bond. Another option is to form a Au-In eutectic as a bonding material. Ge/Au/Ni/Au is deposited on the grown wafer and indium is deposited on the carrier wafer. The thickness of the top Au layer and In layer is 1 μm. These wafers are then heated at 250 °C for 15 minutes. The indium melts and diffuses into the Au layer forming an In-Au eutectic, with a melting temperature close to 450 °C. This eutectic acts as the bonding layer between the two wafers. Wafers of sizes 1 cm × 2 cm have been bonded using these techniques.

A substrate removal process was developed for GaAs substrates in-house as part of this thesis work. A wet etch based process providing a high selectivity is used. The etch used is a 1:4 combination of hydrogen peroxide and citric acid. $\mathrm{Al}_x\mathrm{Ga}_{1-x}\mathrm{As}$, $x \geq 0.7$ has been used as an etch stop layer. The etch rate of the solution is $\approx$20 μm/hr, with no agitation. A combination of citric acid and peroxide etches gallium containing compounds, while the etch rate decreases with increasing aluminum content of the material. This differential etch rate is exploited to develop a cheap substrate removal process, effective for large areas. The largest size wafers used have been one inch in diameter.

The critical step in this etch process is preparation of the etching solution. Citric acid is commercially available as an anhydrous powder. To prepare the liquid, it is mixed with water to form a supersaturated solution. Dissolution of citric acid in water is an endothermic process, requiring external heat for the process. Long agitation and wait periods are necessary to produce a complete dissolution. In this thesis, anhydrous acid and water were mixed and agitated for 45 minutes, and left for 12-15 hours to achieve a solution of desired molarity. Hydrogen peroxide (30%) stored at room temperature was found be ineffective in providing a selective etch in 3-4 weeks, due to loss of strength of the solution. This strong dependence of etch selectivity on the dissociation rate has never been reported previously in other uses of peroxide as an oxidiser, including the use in piranha solution used for etching. An optical image of the bonded wafer with the substrate removed is shown in Figure B.4. Nomarski images at various magnifications show a smooth surface.

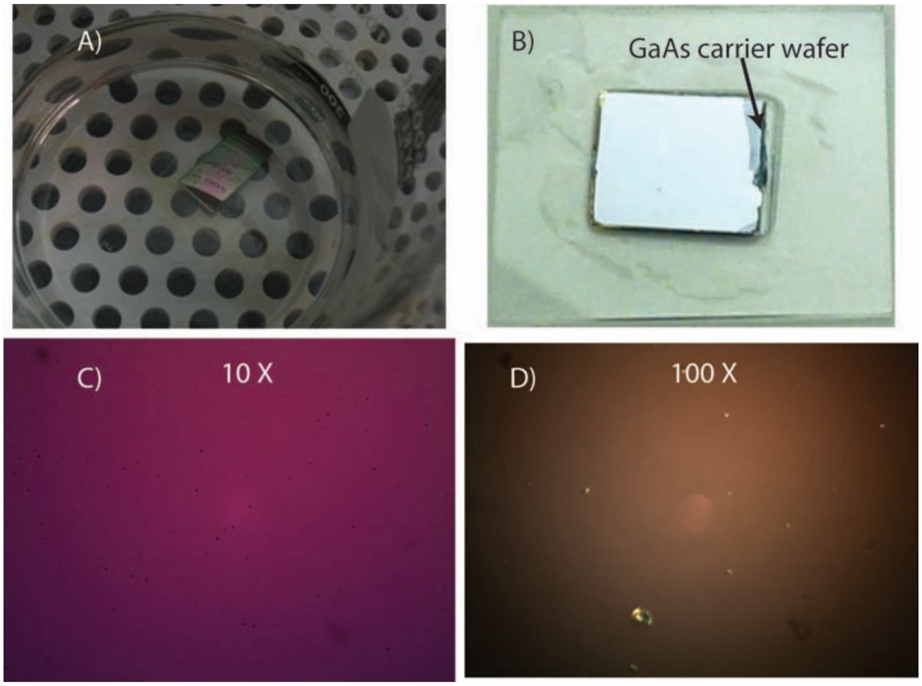

Figure B.4: Images of substrate removal process. A) Wet etching process for substrate removal. The sample is dipped in a mixture of citric acid and hydrogen peroxide, with no agitation. A smooth and shiny surface, comparable to a epitaxially grown layer, indicates complete substrate removal. The samples are mounted on a glass slide. B) A bonded and substrate removed sample. The sample is bonded using a Au-In bonding process. A GaAs substrate is used as the carrier wafer. C), D) Nomarski images obtained at 10× and 100× magnification.

References

[1] http://www.crisp.nus.edu.sg/ research/tutorial/em.htm.

[2] http://www.profc.udec.cl/ gabriel/tutoriales/rsnote/cp1/cp1-7.htm.

[3] http://www.coseti.org/atmosphe.htm.

[4] http://en.wikipedia.org/wiki/infrared.

[5] A. Rogalski. Infrared detectors: an overview. *Infrared Physics and Technology*, 43:187, 2002.

[6] C. H. Wolfe, N. Holonyak, and G. E. Stillman. Physical properties of semiconductors. *Prentice Hall*, 1989.

[7] John Johnson. Analysis of image forming systems. Image Intensifier Symposium, AD 220160 (Warfare Electrical Engineering Department), pages 244–273, 1958.

[8] J. J Sakurai. Modern quantum mechanics. *Addison Wesley*, 1994.

[9] http://people.deas.harvard.edu/ jones/ap216/images/bandgap_engineering.

[10] S. Krishna. Optoelectronic properties of self-assembled InAs/InGaAs quantum dots.

[11] I.N Stranski and L. Krastanow. *Sitzungsberichte d. Akad. D. Wissenschaften in Wien*, IIb:146, 1937.

[12] C. Ratsch and A. Zangwill. Equilibrium theory of the Stranski-Krastanov epitaxial morphology. *Surface Science.*, 293:123, 1993.

[13] T.E. Vandervelde, M.C. Lenz, E. Varley, A. Barve, J. Shao, R. Shenoi, D.A. Ramirez, W. Jang, Y.D. Sharma, and S. Krishna. Multicolor quantum dots-in-a-well focal plane arrays. In *Proc. of SPIE Vol*, volume 6940, pages 694003–1, 2008.

[14] U. Bockelmann and G. Bastard. Phonon scattering and energy relaxation in two-, one-, and zero-dimensional electron gases. *Phys. Rev. B*, 42(14):8947–8951, Nov 1990.

[15] J. Urayama, T. B. Norris, J. Singh, and P. Bhattacharya. Observation of phonon bottleneck in quantum dot electronic relaxation. *Phys. Rev. Lett.*, 86(21):4930–4933, May 2001.

[16] S. Chakrabarti, A. D. Stiff-Roberts, X. H. Su, P. Bhattacharya, G. Ariyawansa, and A. G. U. Perera. High-performance mid-infrared quantum dot infrared photodetectors. *J. Phys. D*, 38:2135, 2005.

[17] S. D. Gunapala and S. V. Bandara. Semiconductors and semimetals. *Academic Press*, 62, 1999.

[18] S. D. Gunapala and S. V. Bandara. Thin films. *Academic Press*, 21, 1995.

[19] S. Tang, C. Chiang, P. Weng, Y. Gau, J. Luo, S. Yang, C. Shih, S. Y. Lin, and S. Lee. High-temperature operation normal incident 256×256 InAs-GaAs quantum-dot infrared photodetector focal plane array. *IEEE Photon. Tech. Lett.*, 18:986, 2006.

[20] L. Fu, H. H. Tan, I. McKerracher, J. Wong-Leung, C. Jagadish, N. Vukmirovic, and P. Harrison. Effects of rapid thermal annealing on device characteristics of InGaAs/GaAs quantum dot infrared photodetectors. *J. Appl. Phys.*, 99:114517, 2006.

[21] A. D. Stiff-Roberts, S. Krishna, P. Bhattacharya, and S. Kennerly. High-detectivity, normal-incidence, mid-infrared ($\lambda \approx 4$ μm) InAs/GaAs quantum-dot detector operating at 150 K. *Appl. Phys. Lett.*, 79:421, 2001.

[22] E. T. Kim, A. Madhukar, Z. Ye, and J. C. Campbell. High detectivity InAs quantum dot infrared photodetectors. *Appl. Phys. Lett.*, 84:3227, 2004.

[23] J. Phillips, P. Bhattacharya, S. W. Kennerly, D. W. Beekmanand, and M. Dutta. Self-assembled InAs-GaAs quantum-dot intersubband detectors. *IEEE J. Quant. Elec.*, 35(6):936, 1999.

[24] P. Bhattacharya, X. H. Su, S. Chakrabarti, G. Ariyawansa, and A. G. U. Perera. Characteristics of a tunneling quantum-dot infrared photodetector operating at room temperature. *Appl. Phys. Lett.*, 86:191106, 2005.

[25] W. Zhang, H. Lim, M. Taguchi, S. Tsao, B. Movaghar, and M. Razeghi. High-detectivity InAs quantum-dot infrared photodetectors grown on InP by metalorganic chemical vapor deposition. *Appl. Phys. Lett.*, 86:191103, 2005.

[26] H. Lim, S. Tsao, W. Zhang, and M. Razeghi. High-performance InAs quantum-dot infrared photodetectors grown on InP substrate operating at room temperature. *Appl. Phys. Lett.*, 90:131112, 2007.

[27] David Z.-Y. Ting, Sumith V. Bandara, Sarath D. Gunapala, Jason M. Mumolo, Sam A. Keo, Cory J. Hill, John K. Liu, Edward R. Blazejewski, Sir B. Rafol, and Yia-Chung Chang. Submonolayer quantum dot infrared photodetector. *Applied Physics Letters*, 94(11):111107, 2009.

[28] S. Tsao, H. Lim, W. Zhang, and M. Razeghi. High operating temperature 320×256 middle-wavelength infrared focal plane array imaging based on an InAs/InGaAs/InAlAs/InP quantum dot infrared photodetector. *Appl. Phys. Lett.*, 90:201109, 2007.

[29] S. D. Gunapala, S. V. Bandara, C. J. Hill, D. Z. Ting, J. K. Liu, Sir B. Rafol, E. R. Blazejewski, J. M. Mumolo, S. A. Keo, S. Krishna, Y. C. Chang, and C. A. Shott. 640× 512 pixels long-wavelength infrared quantum-dot infrared photodetector imaging focal plane array. *IEEE J. Quantum Electron.*, 43(11):230–237, 2007.

[30] S. D. Gunapala. Long-wavelength infrared (LWIR) quantum-dot infrared photodetector (QDIP) focal plane array. *Proc. SPIE*, 6206:62060, 2006.

[31] S.Krishna. Quantum dots-in-a-well infrared photodetector. *J. Phys. D*, 38:2142, 2005.

[32] S. Raghavan, D. Forman, P. Hill, N. R. Weisse-Bernstein, G. von Winckel, P. Rotella, S. Krishna, S. W. Kennerly, and J. W. Little. Normal-incidence InAs/InGaAs quantum dots-in-a-well detector operating in the long wave infrared atmospheric window. *J. Appl. Phys.*, 96:1036, 2004.

[33] M. R. Matthews, R. J. Steed, M. D. Frogley, C. C. Phillips, R. S. Attaluri, and S. Krishna. Transient photoconductivity measurements of carrier lifetimes in an InAs/$In_{0.15}Ga_{0.85}As$ dots-in-a-well detector. *Appl. Phys. Lett.*, 90:103519, 2007.

[34] A Amtout, S Raghavan, P Rotella, G von Winckel, A Stintz, and S Krishna. Theoretical modeling and experimental characterization of InAs/InGaAs quantum dots in a well detector. *J. Appl. Phys.*, 96:3782, 2004.

[35] G. von Winckel, S. Krishna, and E.A. Coutsias. Spectral element modelling of semiconductor heterostructures. *Math. and Comp. Model*, 43:582, 2006.

[36] S. Krishna, S. Raghavan, G. von Winckel, A. Stintz, G. Ariyawansa, S. G. Matsik, and A. G. U. Perera. Three-color ($\lambda_{p1} \approx 3.8\mu$m, $\lambda_{p2} \approx 8.5\mu$m, and $\lambda_{p3} \approx 23.2\mu$m) InAs/InGaAs quantum-dots-in-a-well detector. *Appl. Phys. Lett.*, 83:2746, 2003.

[37] P. Aivaliotis, N. Vukmirovic, E. A. Zibik, J. W. Cockburn, D. Indjin, P. Harrison, C. Groves, J. P. R. David, M. Hopkinson, and L. R. Wilson. Stark shift of the spectral response in quantum dots-in-a-well infrared photodetectors. *J. Phys. D*, 40:5537, 2007.

[38] S. Krishna, D. Forman, S. Annamalai, P. Dowd, P. Varangis, T. Tumolillo, A. Gray, J. Zilko, K. Sun, M. Liu, J. Campbell, and D. Carothers. Demonstration of a 320×256 two-color focal plane array using InAs/InGaAs quantum dots in a well detectors. *Appl. Phys. Lett.*, 86:193501, 2005.

[39] E. S. Varley, S. Krishna, D. A. Ramirez, J. S. Brown, S. J Lee, A. Stintz, M. C. Lenz, A. Riesinger, and M. Sundaram. Demonstration of a two-color 320 × 256 quantum dots-in-a-well focal plane array. *Proc. SPIE*, to be published:22, 2007.

[40] E. Varley, M. Lenz, S. J. Lee, J. S. Brown, D. A. Ramirez, A. Stintz, and S. Krishna. Single bump,two-color quantum dot camera. *Appl. Phys. Lett.*, 91:081120, 2007.

[41] E. L. Dereniak and G. D. Boreman. Infrared detectors and systems. *John Wiley and Sons*, 1996.

[42] R. S. Attaluri, S. Annamalai, K. T. Posani, A. Stintz, and S. Krishna. Influence of Si doping on the performance of quantum dots-in-well photodetectors. *J. Vac. Sci. Tech B.*, 24:1553, 2006.

[43] R. S. Attaluri, J. Shao, K. T. Posani, S. J. Lee, J. S. Brown, A. Stintz, and S. Krishna. Resonant cavity enhanced InAs/$In_{0.15}Ga_{0.85}As$ dots-in-a-well quantum dot infrared photodetector. *J. Vac. Sci. Tech B.*, 25:1186, 2007.

[44] K. T. Posani, V. Tripathi, S. Annamalai, N. R. Weisse-Bernstein, S. Krishna, R. Perahia, O. Crisafulli, and O. J. Painter. Nanoscale quantum dot infrared sensors with photonic crystal cavity. *Appl. Phys. Lett.*, 88:151104, 2006.

[45] S. Krishna, O. Kwon, and M. Hayat. Theoretical investigation of quantum dot avalanche photodiodes for mid-infrared applications. *IEEE. J. Quantum Electron.*, 41:1468, 2005.

[46] AV Barve, SY Shah, J. Shao, TE Vandervelde, RV Shenoi, W.Y. Jang, and S. Krishna. Reduction in dark current using resonant tunneling barriers in quantum dots-in-a-well long wavelength infrared photodetector. *Applied Physics Letters*, 93:131115, 2008.

[47] P. Mitra, F. C. Case, J. H. McCurdy, S. A. Zaidel, and L. T. Claiborne. Multispectral long-wavelength quantum-well infrared photodetectors. *Applied Physics Letters*, 82:3185, 2003.

[48] R. Rehm, M. Walther, J. Schmitz, J. Fleißner, J. Ziegler, W. Cabanski, and R. Breiter. Dual-colour thermal imaging with InAs/GaSb superlattices in mid-wavelength infrared spectral range. *Electronic Letters*, 42:2124–2127, 2006.

[49] R. V. Shenoi, R. S. Attaluri, A. Siroya, J. Shao, Y. D. Sharma, A. Stintz, T. E. Vandervelde, and S. Krishna. Low-strain InAs/InGaAs/GaAs quantum dots-in-a-well infrared photodetector. *J. Vac. Sci. Tech B.*, 26:1136–1139, 2008.

[50] Rajeev Shenoi, Jennifer Hou, Yagya Sharma, Jiayi Shao, Thomas Vandervelde, and Sanjay Krishna. Low strain quantum dots in a double well infrared detec-

tors. In *Proceedings of SPIE Infrared Spaceborne Remote Sensing and Instrumentation XVI*, volume 7082. SPIE, August, 2008.

[51] R. P. Prasankumar, W. W. Chow, J. Urayama, R. S. Attaluri, R. V. Shenoi, S. Krishna, and A. J. Taylor. Density-dependent carrier dynamics in a quantum dots-in-a-well heterostructure. *Applied Physics Letters*, 96(3):031110, 2010.

[52] T.E. Vandervelde, M.C. Lenz, E. Varley, A. Barve, Jiayi Shao, R.V. Shenoi, D.A. Ramirez, Wooyong Jan, Y.D. Sharma, and S. Krishna. Quantum dots-in-a-well focal plane arrays. *Selected Topics in Quantum Electronics, IEEE Journal of*, 14(4):1150–1161, July-Aug. 2008.

[53] RP Prasankumar, WW Chow, J. Urayama, RS Attaluri, RV Shenoi, S. Krishna, and AJ Taylor. Density-dependent carrier dynamics in a quantum dots-in-a-well heterostructure. *Applied Physics Letters*, 96:031110, 2010.

[54] Rajeev V. Shenoi, Aaron Gin, Jessie Rosenber, Oskar J. Painter, and Sanjay Krishna. Selective excitation of resonant plasmon and waveguide modes in a metal-semiconductor nanostructure. *Nano Letters*, Submitted to Nano Letters.

[55] R. V. Shenoi, D. A. Ramirez, Y. Sharma, R. S. Attaluri, J. Rosenberg, O. J. Painter, and S. Krishna. Plasmon assisted photonic crystal quantum dot sensors. In *Society of Photo-Optical Instrumentation Engineers (SPIE) Conference Series*, volume 6713 of *Society of Photo-Optical Instrumentation Engineers (SPIE) Conference*, October 2007.

[56] R. V. Shenoi, J. Rosenberg, T.E. Vandervelde, O.J. Painter, and S. Krishna. Multispectral quantum dots-in-a-well infrared detectors using plasmon assisted cavities. *Quantum Electronics, IEEE Journal of*, 46(7):1051–1057, july 2010.

[57] R. V. Shenoi, J. Rosenberg, T. E. Vandervelde, O. J. Painter, , and S. Krishna. Multispectral infrared detection using plasmon-assisted cavities. In Bjorn F.

Andresen, Gabor F. Fulop, and Paul. R. Norton, editors, *Proceedings of SPIE Infrared Technology and Applications XXXV*, volume 7298. SPIE, April, 2009.

[58] Jessie Rosenberg, Rajeev V. Shenoi, Sanjay Krishna, and Oskar Painter. Design of plasmonic photonic crystal resonant cavities for polarization sensitive infrared photodetectors. *Opt. Express*, 18(4):3672–3686, 2010.

[59] Jessie Rosenberg, Rajeev V. Shenoi, Thomas E. Vandervelde, Sanjay Krishna, and Oskar Painter. A multispectral and polarization-selective surface-plasmon resonant midinfrared detector. *Applied Physics Letters*, 95(16):161101, 2009.

[60] Chun-Chieh Chang, Yagya D. Sharma, Yong-Sung Kim, Jim A. Bur, Rajeev V. Shenoi, Sanjay Krishna, Danhong Huang, and Shawn-Yu Lin. A surface plasmon enhanced infrared photodetector based on InAs quantum dots. *Nano Letters*, 10(3):1704–1709, April 2010.

[61] S. Tsao, H. Lim, W. Zhang, and M. Razeghi. High operating temperature 320 x 256 middle-wavelength infrared focal plane array imaging based on an InAs/InGaAs/InAlAs/InP quantum dot infrared photodetector. *Applied Physics Letters*, 90(20):201109, 2007.

[62] H. Lim, S. Tsao, W. Zhang, and M. Razeghi. High-performance InAs quantum-dot infrared photodetectors grown on InP substrate operating at room temperature. *Applied Physics Letters*, 90(13):131112, 2007.

[63] Ram Saran Attaluri. *Growth and Optimization of Quantum Dots-in-a-well Infrared Photodetectors*. PhD thesis, University of New Mexico, 2007.

[64] J. Scott Tyo, Dennis L. Goldstein, David B. Chenault, and Joseph A. Shaw. Review of passive imaging polarimetry for remote sensing applications. *Appl. Optics*, 45:5453–5469, 2006.

[65] Harald Schneider and H. C. Liu. *Quantum Well Infrared Photodetectors*. Springer Series in Optical Sciences. Springer, 2007.

[66] S.D. Gunapala, S.V. Bandara, J.K. Liu, E.M. Luong, N. Stetson, C.A. Shott, J.J. Bock, S.B. Rafol, J.M. Mumolo, and M.J. McKelvey. Long-wavelength 256×256 GaAs/AlGaAs quantum well infrared photodetector (QWIP) palm-size camera. *IEEE Trans. Electron Devices*, 47(2):326–332, Feb 2000.

[67] M. Z. Tidrow, J. C. Chiang, Sheng S. Li, and K. Bacher. A high strain two-stack two-color quantum well infrared photodetector. *Appl. Phys. Lett.*, 70(7):859–861, 1997.

[68] W. Wu, A. Bonakdar, and H. Mohseni. Plasmonic enhanced quantum well infrared photodetector with high detectivity. *Applied Physics Letters*, 96:161107, 2010.

[69] Jagmohan Bajaj, Jerry Sullivan, Don Lee, Ed Eifer, and Manijeh Razeghi. Comparison of type-ii superlattice and hgcdte infrared detector technologies. volume 6542. SPIE, 2007.

[70] A. Rogalski, J. Antoszewski, and L. Faraone. Third-generation infrared photodetector arrays. *Journal of Applied Physics*, 105(9):091101, 2009.

[71] M. A. Kinch. *Fundamentals of Infrared Detector Materials*. SPIE Press, 2007.

[72] C.A. Musca, J. Antoszewski, K.J. Winchester, A.J. Keating, T. Nguyen, K.K.M.B.D. Silva, J.M. Dell, L. Faraone, P. Mitra, J.D. Beck, M.R. Skokan, and J.E. Robinson. Monolithic integration of an infrared photon detector with a mems-based tunable filter. *Electron Device Letters, IEEE*, 26(12):888–890, Dec. 2005.

[73] T. R. Schimert, S. L. Barnes, A. J. Brouns, F. C. Case, P. Mitra, and L. T. Claiborne. Enhanced quantum well infrared photodetector with novel multiple

quantum well grating structure. *Applied Physics Letters*, 68(20):2846–2848, 1996.

[74] S. Schartner, S. Golka, C. Pflugl, W. Schrenk, A. M. Andrews, T. Roch, , and G. Strasser. Band structure mapping of photonic crystal intersubband detectors. *Appl. Phys. Lett.*, 89:151107, 2006.

[75] H. Raether. *Surface plasmons on smooth and rough surfaces and on grattings.* 1988.

[76] Stefan A. Maier. *Plasmonics: Fundamentals and Applications.* Springer, 2007.

[77] T. W. Ebbesen, H. J. Lezec, H. F. Ghaemi, T. Thio, and P. A. Wolff. Extraordinary optical transmission through sub-wavelength hole arrays. *Nature*, 391:667–669, 1998.

[78] C. Genet and T. W. Ebbesen. Light in tiny holes. *Nature*, 445(7123):39–46, January 2007.

[79] Jon A. Schuller, Edward S. Barnard, Wenshan Cai, Young C. Jun, Justin S. White, and Mark L. Brongersma. Plasmonics for extreme light concentration and manipulation. *Nature Materials*, 9(3):193–204, February 2010.

[80] Hideki T. Miyazaki and Yoichi Kurokawa. Squeezing visible light waves into a 3-nm-thick and 55-nm-long plasmon cavity. *Phys. Rev. Lett.*, 96(9):097401, Mar 2006.

[81] Harry A. Atwater and Albert Polman. Plasmonics for improved photovoltaic devices. *Nature Materials*, 9(3):205–213, February 2010.

[82] E. Laux, C. Genet, T. Skauli, and T.W. Ebbesen. Plasmonic photon sorters for spectral and polarimetric imaging. *Nature Photonics*, 2(3):161–164, 2008.

[83] S. Krishna. The infrared retina. *Journal of Physics D: Applied Physics*, 42:234005, 2009.

[84] B. K. Minhas, W. Fan, K. Agi, S. R. J. Brueck, and K. J. Malloy. Metallic inductive and capacitive grids: theory and experiment. *J. Opt. Soc. Am. A*, 19(7):1352–1359, 2002.

[85] Stefan A. Maier and Harry A. Atwater. Plasmonics: Localization and guiding of electromagnetic energy in metal/dielectric structures. *Journal of Applied Physics*, 98(1):011101, 2005.

[86] Saleem H. Zaidi, M. Yousaf, and S. R. J. Brueck. Grating coupling to surface plasma waves. i. first-order coupling. *J. Opt. Soc. Am. B*, 8(4):770–779, 1991.

[87] Vivian E. Ferry, Marc A. Verschuuren, Hongbo B. T. Li, Ruud E. I. Schropp, Harry A. Atwater, and Albert Polman. Improved red-response in thin film a-Si:H solar cells with soft-imprinted plasmonic back reflectors. *Applied Physics Letters*, 95(18):183503, 2009.

[88] Vivian E. Ferry, Luke A. Sweatlock, Domenico Pacifici, and Harry A. Atwater. Plasmonic nanostructure design for efficient light coupling into solar cells. *Nano Letters*, 8(12):4391–4397, December 2008.

[89] Daisuke Okamoto, Junichi Fujikata, Kenichi Nishi, and Keishi Ohashi. Numerical study of near-infrared photodetectors with surface-plasmon antenna for optical communication. *Japanese Journal of Applied Physics*, 47(4):2921–2923, 2008.

[90] Peter N. Saeta, Vivian E. Ferry, Domenico Pacifici, Jeremy N. Munday, and Harry A. Atwater. How much can guided modes enhance absorption in thin solar cells? *Opt. Express*, 17(23):20975–20990, 2009.

[91] S. C. Lee, S. Krishna, and S. R. J. Brueck. Quantum dot infrared photodetector enhanced by surface plasma wave excitation. *Opt. Express*, 17(25):23160–23168, 2009.

[92] D. Wasserman, E. A. Shaner, and J. G. Cederberg. Midinfrared doping-tunable extraordinary transmission from sub-wavelength gratings. *Applied Physics Letters*, 90(19):191102, 2007.

[93] C. T. Middlebrook, G. Zummo, and G. D. Boreman. Direct-write electron-beam lithography of an ir antenna-coupled microbolometer onto the surface of a hemispherical lens. *Journal of Vacuum Science and Technology B: Microelectronics and Nanometer Structures*, 24(6):2566–2569, 2006.

[94] DL Smith and C. Mailhiot. Proposal for strained type II superlattice infrared detectors. *Journal of Applied Physics*, 62:2545, 1987.

[95] Elena Plis, Jean B. Rodriguez, and Sanjay Krishna. *InAs/(In)GaSb Type II Strain Layer Superlattice Detectors*. Elsevier, to be published.

[96] Y. Wei, A. Hood, H. Yau, A. Gin, M. Razeghi, M.Z. Tidrow, and V. Nathan. Uncooled operation of type-II InAs/GaSb superlattice photodiodes in the mid-wavelength infrared range. *Applied Physics Letters*, 86(23):233106–233106, 2005.

[97] GJ Sullivan, A. Ikhlassi, J. Bergman, RE DeWames, JR Waldrop, C. Grein, M. Flatté, K. Mahalingam, H. Yang, M. Zhong, et al. Molecular beam epitaxy growth of high quantum efficiency InAs/GaSb superlattice detectors. *Journal of Vacuum Science & Technology B: Microelectronics and Nanometer Structures*, 23:1144, 2005.

[98] B.M. Nguyen, S. Bogdanov, S.A. Pour, and M. Razeghi. Minority electron unipolar photodetectors based on type II InAs/GaSb/AlSb superlattices for

very long wavelength infrared detection. *Applied Physics Letters*, 95:183502, 2009.

[99] A. Khoshakhlagh, E. Plis, S. Myers, YD Sharma, LR Dawson, and S. Krishna. Optimization of InAs/GaSb type-II superlattice interfaces for long-wave (8 μm) infrared detection. *Journal of Crystal Growth*, 311(7):1901–1904, 2009.

[100] HS Kim, E. Plis, JB Rodriguez, GD Bishop, YD Sharma, LR Dawson, S. Krishna, J. Bundas, R. Cook, D. Burrows, et al. Mid-IR focal plane array based on type-II InAs/ GaSb strain layer superlattice detector with nBn design. *Applied Physics Letters*, 92:183502, 2008.

[101] B.M. Nguyen, D. Hoffman, P.Y. Delaunay, M. Razeghi, and V. Nathan. Polarity inversion of type II InAs/ GaSb superlattice photodiodes. *Applied Physics Letters*, 91:103503, 2007.

[102] E. Plis, JB Rodriguez, G. Balakrishnan, YD Sharma, HS Kim, T. Rotter, and S. Krishna. Mid-infrared InAs/GaSb strained layer superlattice detectors with nBn design grown on a GaAs substrate. *Semiconductor Science and Technology*, 25:085010, 2010.

[103] S.A. Pour, BM Nguyen, S. Bogdanov, EK Huang, and M. Razeghi. Demonstration of high performance long wavelength infrared type II InAs/GaSb superlattice photodiode grown on GaAs substrate. *Applied Physics Letters*, 95:173505, 2009.

[104] G. Balakrishnan, J. Tatebayashi, A. Khoshakhlagh, SH Huang, A. Jallipalli, LR Dawson, and DL Huffaker. III/V ratio based selectivity between strained Stranski-Krastanov and strain-free GaSb quantum dots on GaAs. *Applied Physics Letters*, 89:161104, 2006.

[105] S. H. Huang, G. Balakrishnan, A. Khoshakhlagh, A. Jallipalli, L. R. Dawson, and D. L. Huffaker. Strain relief by periodic misfit arrays for low defect density gasb on gaas. *Applied Physics Letters*, 88(13):131911, 2006.

[106] SC Lee, S. Krishna, and SRJ Brueck. Light direction-dependent plasmonic enhancement in quantum dot infrared photodetectors. *Applied Physics Letters*, 97:021112, 2010.

[107] W.Y. Jang, M.M. Hayat, J.S. Tyo, R.S. Attaluri, T.E. Vandervelde, Y.D. Sharma, R. Shenoi, A. Stintz, E.R. Cantwell, S.C. Bender, et al. Demonstration of bias-controlled algorithmic tuning of quantum dots in a well (DWELL) midIR detectors. *IEEE J. Quantum Electron*, 45:674–83, 2009.

[108] Rajeev Ramanath, Wesley E. Snyder, and Hairong Qi. Mosaic multispectral focal plane array cameras. volume 5406, pages 701–712. SPIE, 2004.

[109] Ming Cai, Oskar Painter, and Kerry J. Vahala. Observation of critical coupling in a fiber taper to a silica-microsphere whispering-gallery mode system. *Phys. Rev. Lett.*, 85(1):74–77, Jul 2000.

[110] Xianliang Liu, Tatiana Starr, Anthony F. Starr, and Willie J. Padilla. Infrared spatial and frequency selective metamaterial with near-unity absorbance. *Phys. Rev. Lett.*, 104(20):207403, May 2010.

[111] A. Benz, G. Fasching, Ch. Deutsch, A. M. Andrews, K. Unterrainer, P. Klang, W. Schrenk, and G. Strasser. Terahertz photonic crystal resonators in double-metal waveguides. *Opt. Express*, 15(19):12418–12424, 2007.

[112] Benjamin S. Williams, Sushil Kumar, Hans Callebaut, Qing Hua, and John .L Reno. Terahertz quantum-cascade laser at 100 μm using metal waveguide for mode confinement. *Appl. Phys. Lett.*, 83:2124–2127, 2003.

[113] Karl Unterrainer, Raffaele Colombelli, Claire Gmachl, Harold Y. Hwang, Federico Capasso, A. Michael Sergent, Deborah L. Sivco, and Alfred Y. Cho. Quantum cascade lasers with double metal-semiconductor waveguide resonators. *Appl. Phys. Lett.*, 80:3060–3062, 2002.

[114] N. Gautam, H. S. Kim, M. N. Kutty, E. Plis, L. R. Dawson, and S. Krishna. Performance improvement of longwave infrared photodetector based on type-ii InAs/GaSb superlattices using unipolar current blocking layers. *Applied Physics Letters*, 96(23):231107, 2010.